The Nuclear Dependence of Structure Function Ratios from Unpolarized Deep Inelastic Scattering

by

Taeksu Shin

M.S. in Physics, Hampton University
August 1993

Submitted to the Department of Physics
in partial fulfillment of the requirements for the degree of

Doctor of Philosophy

at the

MASSACHUSETTS INSTITUTE OF TECHNOLOGY

Feb 2000

Author ....
Department of Physics
January 23, 2000

Certified by ....
Professor Richard G. Milner
Professor of Physics
Thesis Supervisor

Accepted by ....
Professor Patrick Lee
Graduate Student Coordinator

The Nuclear Dependence of Structure Function Ratios from Unpolarized Deep Inelastic Scattering

by

Taeksu Shin

Submitted to the Department of Physics
on January 23, 2000, in partial fulfillment of the
requirements for the degree of
Doctor of Philosophy

Abstract

Deep-inelastic scattering from unpolarized ^{2}H, ^{3}He and ^{14}N gas targets has been measured by the HERMES experiment at DESY. The ratios of the inclusive nuclear cross sections with respect to the deuterium cross section have been determined in the x range of $0.013 < x < 0.7$ with the average Q^2 varying between 0.5 and 7 GeV^2. The data are compared to existing measurements by NMC and E665 and are found to be substantially different for x values below $x = 0.1$. As the experiments were performed at largely different incident lepton energies, the cross section ratios are measured for different values of the virtual photon polarization parameter ϵ. The observed difference in the cross section ratios is attributed to a large A-dependence of the longitudinal structure function at low x and low Q^2.

Thesis Supervisor: Professor Richard G. Milner
Title: Professor of Physics

Acknowledgments

This work would not be possible without help from many people. I would like to take this opportunity to express my gratitude to those who have provided support and help throughout my career.

I am very grateful to my advisor, Richard Milner, not only for his guidance with full of keen insight into nature but also for his encouragment and support. In spite of my many mistakes, he has always been supportive. At the final stage of this work, his careful reading and comments were indispensible and made this thesis readable. I also would like to thank Robert Redwine. He has been always kind and receptive to my abrupt visits to his office and gave me kind advice on many aspects of my life. I would like to thank Antje Brüll for her help with my analysis. This thesis would not be possible without her contributions and help. I also thank Victoria Kaspi and William Donnelly for carefully reading and commenting my thesis. I credit Bill with giving me an idea for checking basic assumptions in this analysis. It made this thesis results valuable. I owe many thanks to Gerard vd Steenhoven and Jeroen J. van Hunen for their help on finalizing this analysis and writing a beautiful paper. Their help on this work has been a great source of reliability. I wish Jeroen to have a very wonderful physics career with his new position at CERN. I also would like to thank Arthur Mateos for introducing a new perspective in my analysis and help me throughout many hard times. I would like to thank Igor Akushevich for his help and suggestions on radiative correction study. I would like to also thank my former advisor, Keith Baker, for his encouragement and support. He provided me with a great chance to exploit further career in physics at MIT. It has been a great privilege for me to be a part of such a wonderful physics department.

I would like to thank Steve Pate, Laird Kramer and Dirk Schepper for their friendship and helping me starting HERMES project at the early stage. I also thank Bryan Tipton, Jeffery Martin, Mark Sutter and Nik Gregory. Without their friendship, my life at MIT would have been very dry. I would like to thank Kevin Lee, William Schmitt, the late Hojoon Park, Shiao-bin Soong, Kyungeon Joo, Kevin Mcilhany, David Lowntree, Dipangkar Dutta, Bill Franklin, Doug Hassel, Vitaly Ziskin, Joanne Gregory, Haijun Song, and many more from LNS. I would like to thank these people from HERMES for being patient with my bad English, Elke Aschenauer, Balijeet Bains, Eric Belz, Tomas Benisch, Bruce Bray, Walter Brueckner, Geoffrey Court, Brad Filippone, Brendan Fox, M. A. Funk, Philipp Geiger, Ole Hansen, Yorck Holler, Harold Jackson, Edward Kinney, Machiel Kolstein, Hauke Kolster, Wolfgang Korsch, Sabine Krohn, Naomi Makins, Ramona Matthes, Andy Miller, Tom ONeill, Jinsong Ouyang, Brynnen Owen, Mark Pitt, Hans-Juergen Plett, Greg Rakness, Dirk Ryckbosch, Yashushiro Sakemi, Gunar Schnell, Vitaly Shutov, James Stewart, Erhard Steffens, Uta Stoesslein, Hugh Tallini, Mike Vetterli, Manuella Vincter, Erik Volk, Wolfgang Wonder, Tom Wise, and many more.

Many thanks go to my friends and seniors: John Ahn, Jonghak Kim, Churl Oh from GBS; Shinoo Nam, Sebyung, Chinkyoung, Changryong, Minkyu in Hamburg; Daeki Kim, Youngki Lee and Byungjoon Hwang for their friendship.

I also thank my parents, Youngjin Shin, Dongnyeu Jang, Seungryong Han, Soonee Song, and all of my family in Korea for their endless support and care throughout my life. I would like to thank my kids, Michael and Michelle, for their happy smiles in spite of my absence. I regreted that I was always away from Michael's birthday during my frequent travels to Germany. Lastly, I would like to acknowledge my wife Yunjeong, to whom this thesis is dedicated, for her endless love and sincere devotion over entire period of our marriage. Her absolute support and encouragement have been an ultimate source of my resilence.

Contents

Chapter 1

Deep Inelastic Scattering

1.1 Introduction

The very ancient and fundamental question *what is the structure of matter* has been the main driving force to study nature at ever smaller distance scales. After the magnificent work of Rutherford in the early 20th century, the technique of scattering has been the principal tool to probe inside matter and answer this basic question. The many realizations of Rutherford's basic idea have been exploited to access the substructure of matter. One example is deep inelastic scattering (DIS) which gives a window on the quark structure inside the nucleon.

Deep inelastic scattering of charged and neutral leptons has been a very powerful tool for studying the substructure of the nucleon and has revealed most of what we know about the quark structure of the nucleon and of the nucleus citebib:mallot. The very first deep inelastic scattering experiments were conducted in the late 1960's at the Stanford Linear Accelerator Center(SLAC). It was found that the cross section for this process was roughly independent of the wavelength of the virtual photon or the scale at which the nucleon was probed. From the *scaling property* of the cross section, the SLAC DIS experiment led to the discovery of partons [1, 2] which later were identified with hypothetical quarks, postulated earlier to explain the hadron spectrum [3, 4], and to the subsequent development of the Quark Parton Model(QPM) [5, 6]. DIS also played an important role in the discovery of missing constituents, later identified as gluons, and the merging of all pictures into a coherent dynamical theory of quarks and gluons, Quantum Chromodynamics(QCD).

Although a consistent picture emerged and DIS has been developed to be a very precise tool, its history has contained a number of surprises. The first observation of A-dependence in the DIS structure functions, the so called EMC effect, was made by the European Muon Collaboration (EMC) [7]. The cross section ratio of iron to deuterium showed a deviation from unity, which indicated a significant nuclear binding effect on the nucleons inside the nucleus. Later, the violation of the Ellis-Jaffe sum rule [8, 9] in polarized muon DIS by EMC [10, 11] gave rise to many questions concerning our understanding of the spin structure of the nucleon. Further, the observed violation of the Gottfried sum rule [12] by the New Muon Collaboration (NMC) [13] suggested that the light quark sea is not flavor symmetric. This was later confirmed by experiment E866 at FERMILAB [14] and by HERMES [15], independently.

The recent objectives of DIS experiments include the detailed study of the x-dependence of the parton distributions; the study of their Q^2 evolution; and the direct test of perturbative QCD (pQCD). The fundamental theory of the strong interaction, QCD, is very successful in describing DIS data at high Q^2. However, whenever QCD meets with low x and Q^2, there are still many unanswered questions. One of the fundamental questions from a nuclear physics perspective is how do the quark and gluon distributions of the nucleon change in the nuclear environment. What are the mechanisms responsible for such changes? These issues are the main motivations for this thesis work.

The HERMES (HERa MEasurement of Spin) experiment was designed to study the spin structure of the nucleon using polarized deep inelastic scattering. The experiment is located at the Deutsche Elektronen Synchrotron(DESY) laboratory in Hamburg, Germany. DESY's Hadronen Elektronen Ring Anlage (HERA) circulates a 27.5 GeV, naturally polarized positron beam. HERMES uses polarized internal gas targets to carry out the spin dependent DIS measurements. However, by flowing unpolarized gas to the internal target, HERMES also produces very abundant, high quality DIS data to study nuclear effects on unpolarized DIS structure function ratios and vector meson production. HERMES has been taking data since 1995 and this thesis work uses the unpolarized DIS data: 4.3 million events from ^1H, ^2H, and ^3He taken in 1996 and 2.2 million events from ^2H and ^{14}N taken in 1997.

The thesis is divided into six chapters. In chapter 1, the deep inelastic scattering process in the languages of the QPM and QCD is briefly discussed in the context of the current DIS world data. A detailed description of the HERMES experiment is presented in chapter 2. In chapters 3 and 4 the data analysis and extraction of cross section ratios are discussed. Chapter 5 contains a discussion of the implications of the HERMES results in terms of new nuclear effects. Conclusions based on these studies are summarized in chapter 6.

1.2 Deep Inelastic Scattering

The physical process under study in this thesis is the deep inelastic scattering of a charged lepton from an unpolarized, stationary target and the reaction can be written as

$$e + N \rightarrow e' + X \tag{1.1}$$

where e and $e^{'}$ denote the incoming and outgoing positron, respectively, N is the target nucleus and X is the final state of the hadronic system. When the momentum transfer and the mass of the final state hadronic system are large enough compared to typical hadron masses, the process is referred to as deep inelastic scattering. In the kinematic domain of deep inelastic scattering, the target nucleons break up and then produce hadrons through the process of hadronization. If the scattered leptons are detected and the hadrons are ignored through the above process, then the process is called inclusive scattering. Since the resolution of the scattering process is inversely proportional to the four-momentum squared, the substructure of the nucleon becomes visible in deep inelastic scattering.

The lowest order Feynman diagram for the deep inelastic scattering process is shown in figure 1-1. The contribution from two (or more) exchanged virtual photons is suppressed since $\alpha(= e^2/4\pi\epsilon_0\hbar c \sim 1/137)$ is small. The heavy bosons such as W and Z^0 are also not considered because of the relatively low center of mass energies of the measurements described in this thesis.

The basic variables used are the four momenta of the incoming and outgoing leptons $k = (E, \mathbf{k})$ and $k^{'} = (E^{'}, \mathbf{k}^{'})$, respectively; the nucleon four momentum $p = (M, 0)$; the four momentum of the virtual photon $q = k - k^{'}$. The scattering angle of the lepton in the laboratory frame is denoted as θ. The commonly used kinematic variables are given in table 1.1. The variable $x(= x_{Bj})$, known as the Bjorken scaling variable, has a direct physical interpretation in the quark parton model. In the infinite momentum frame where the nucleon has an infinitely large momentum and all masses and transverse momenta can be neglected, x is the fraction of the nucleon's momentum carried by the struck quark. The variable y in the laboratory frame is the fractional energy of the incident lepton transferred to the target nucleon. Together with the fact that both Q^2 and ν are positive, this gives the allowed range of the scaling variables of x and y as:

$$\begin{aligned} 0 \leq x \leq 1 \\ 0 \leq y \leq 1 \end{aligned} \tag{1.2}$$

The minimum value of the invariant mass of the hadronic system, W, occurs when the lepton scatters elastically off the target as a whole:

$$W^2 \equiv (p+q)^2 = M^2 + 2M\nu - Q^2 \geq M^2. \tag{1.3}$$

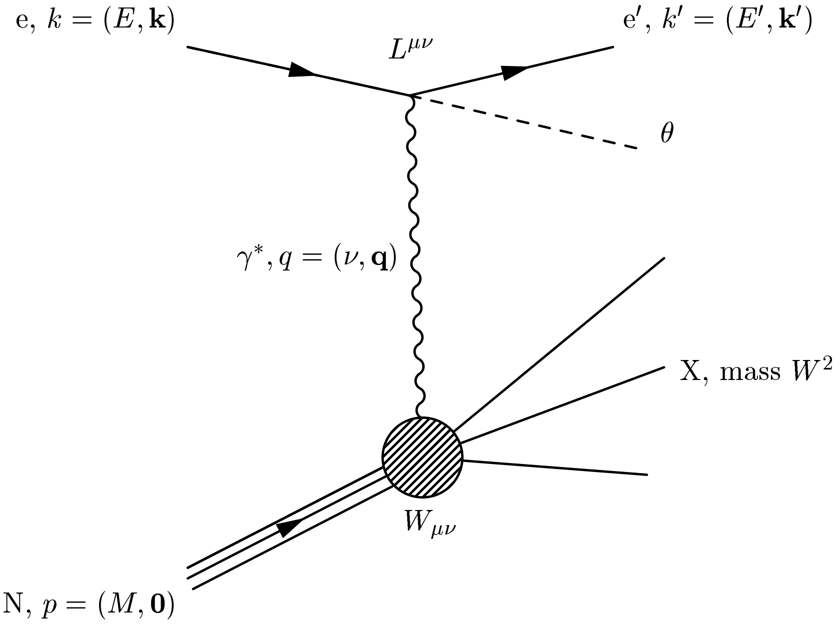

Figure 1-1: The lowest order Feynman diagram for the deep inelastic scattering process is shown. The lepton e scatters from the target nucleon N by exchanging a virtual photon γ^*.

1.2.1 The one photon exchange cross section of DIS

Assuming single photon exchange in the reaction (1.1), the double differential one photon exchange absorption cross section [16, 17] may be written as

$$\frac{d^2\sigma}{dQ^2 d\nu} = \frac{4\pi\alpha^2}{Q^4 E^2} L_{\mu\nu} W^{\mu\nu} \tag{1.4}$$

where α is the fine structure constant, $L_{\mu\nu}$ the leptonic current tensor, and $W^{\mu\nu}$ the hadronic current tensor. The leptonic current tensor $L_{\mu\nu}$ describes the emission of the virtual photon by the lepton and is given as [16]

$$\begin{aligned} L_{\mu\nu} &= \frac{1}{2} \sum_{s'} \bar{u}(k', s') \gamma_\mu u(k, s) \bar{u}(k, s) \gamma_\nu u(k', s') \\ &= \frac{1}{2} Tr(\not{k}' + m) \gamma_\mu (\not{k} + m) \\ &= 2[k'_\mu k_\nu + k_\mu k'_\nu - g_{\mu\nu}(k \cdot k' - m^2)] \end{aligned} \tag{1.5}$$

Variable	Covariant form	Laboratory system
Q^2	$-q^2 = -(k-k^{'})^2$	$2EE'(1-\cos\theta)$
ν	$p \cdot q/\mathrm{M}$	$E - E^{'}$
x	$Q^2/(2p \cdot q)$	$Q^2/(2M\nu)$
y	$p \cdot q/(p \cdot k)$	ν/E
W^2	$(p+q)^2$	$M^2 + 2M\nu - Q^2$

Table 1.1: The kinematic variables commonly used in the deep inelastic scattering process are shown.

where $\bar{u}$ and u are the lepton spinors obeying the Dirac equation, $s(s')$ is the initial(final) spin of the lepton and $g^{\mu\nu}$ is the metric tensor. The hadronic tensor $W^{\mu\nu}$ [16] describes the photon-nucleon vertex and can be written if the initial nucleon is unpolarized:

$$W^{\mu\nu} = W_1 g^{\mu\nu} + \frac{W_2}{M^2} p^\mu p^\nu + \frac{W_4}{M^2} q^\mu q^\nu + \frac{W_5}{M^2}(p^\mu q^\nu + q^\mu p^\nu) \tag{1.6}$$

Here $L_{\mu\nu}$ is symmetric in $\mu\nu$ and hence only the symmetric part of $W^{\mu\nu}$ contributes to the unpolarized cross section. The W_i are in general functions of ν and Q^2 and gauge invariance constrains $q_{\mu\nu} W^{\mu\nu} = 0$ for any ν and Q^2. Applying this to the above $W^{\mu\nu}$ requires

$$\begin{aligned} W_5 &= -W_2(p \cdot q/q^2) \\ W_4 &= W_2(p \cdot q/q^2)^2 - W_1 M^2/q^2 \end{aligned} \tag{1.7}$$

and then the hadronic current tensor $W^{\mu\nu}$ becomes

$$\begin{aligned} W^{\mu\nu} = &- (g_{\mu\nu} - \frac{q_\mu q_\nu}{q^2}) W_1(x, Q^2) \\ &+ (p_\mu - q_\mu \frac{p \cdot q}{q^2})(p_\nu - q_\nu \frac{p \cdot q}{q^2}) \frac{1}{M^2} W_2(x, Q^2). \end{aligned} \tag{1.8}$$

Therefore, the $L_{\mu\nu} W^{\mu\nu}$ term in equation (1.4) becomes

$$L_{\mu\nu} W^{\mu\nu} = 4W_1 k \cdot k' + \frac{W_2}{M^2} 4(p \cdot k)(p \cdot k') - 2k \cdot k' M^2. \tag{1.9}$$

In the laboratory frame, by substituting the equation (1.9) into (1.4), the double differential one photon exchange cross section becomes

$$\frac{d^2\sigma}{dQ^2 d\nu} = \frac{4\pi\alpha^2}{Q^4 E^2}[W_2(\nu, Q^2)\cos^2\frac{\theta}{2} + 2W_1(\nu, Q^2)\sin^2\frac{\theta}{2}] \tag{1.10}$$

By comparing this with the formula for elastic *e-p* scattering, the inelastic structure functions $W_{1,2}$ in equation (1.10) can be expressed as

$$\begin{aligned} W_1^{el}(\nu, Q^2) &= \frac{Q^2}{4M^2} G_M^2(Q^2)\delta(\nu - \frac{Q^2}{2M}) \\ W_2^{el}(\nu, Q^2) &= \frac{G_E^2(Q^2) + (Q^2/4M^2)G_M^2(Q^2)}{1 + Q^2/4M^2}\delta(\nu - \frac{Q^2}{2M}) \end{aligned} \tag{1.11}$$

where $W_{1,2}^{el}$ are the elastic structure functions and $G_{E,M}$ are the electric and magnetic Sachs form factor [16].

For a Dirac particle with *point-like* structure coupling, one finds the dimensionless relations [16]:

$$\begin{aligned} 2MW_1(\nu, Q^2) &= \frac{Q^2}{2M\nu}\delta(\frac{Q^2}{2M\nu} - 1) \\ \nu W_2(\nu, Q^2) &= \delta(\frac{Q^2}{2M\nu} - 1). \end{aligned} \tag{1.12}$$

It is worth while to note that the structure function $W_{1,2}$ depend on only one variable $x = Q^2/2M\nu$ and this is the signature for scattering from point-like objects.

The structure functions $W_{1,2}$ are function of both ν and Q^2 and the squared mass of the unobserved hadronic system W^2 is in the laboratory frame. For fixed W^2 values, the structure function $W_{1,2}$ shows

$$\left.\begin{aligned} MW_1(W, Q^2) \\ \nu W_2(W, Q^2) \end{aligned}\right\} \xrightarrow{Q^2\to\infty} 0 \tag{1.13}$$

due to the resonance form factors decreasing at large Q^2. However, for a fixed $x = Q^2/2M\nu$ and $Q^2 \geq 1$, there is the striking prediction of Bjorken scaling [6] as

$$\begin{aligned} MW_1(x,Q^2) &\xrightarrow{Q^2\to\infty} F_1(x) \\ \nu W_2(x,Q^2) &\xrightarrow{Q^2\to\infty} F_2(x) \end{aligned} \tag{1.14}$$

The above two structure functions $W_{1,2}(\nu, Q^2)$ can be written in terms of the absorption cross section for virtual transverse($\pm$ helicity) and longitudinal helicity(0 helicity) photons, σ_T and σ_L. A photon moving along the z-axis with energy ν and squared mass Q^2 can have polarization vectors as

$$\begin{aligned} \varepsilon(\pm 1) &= \mp\frac{1}{\sqrt{2}}(0; 1, \pm i, 0) \\ \varepsilon(0) &= \frac{1}{\sqrt{Q^2}}(\sqrt{Q^2+\nu^2}, 0, 0, \nu) \end{aligned} \tag{1.15}$$

to satisfy the gauge invariance of $q \cdot \varepsilon$. By defining $\sigma_{\pm 1,0}$ as

$$\sigma_{\pm 1,0} = \frac{4\pi\alpha}{K}\varepsilon^{\mu}_{\pm 1,0} W_{\mu\nu} \varepsilon^{\nu}_{\pm 1,0} \tag{1.16}$$

with the incident photon flux K, the two structure functions $W_{1,2}$ become

$$\begin{aligned} W_1 &= \frac{K}{4\pi^2\alpha}\sigma_T \\ W_2 &= \frac{K}{4\pi^2\alpha}(\sigma_T + \sigma_L)\frac{Q^2}{Q^2+\nu^2} \end{aligned} \tag{1.17}$$

with $\sigma_T \equiv \frac{1}{2}(\sigma_+ + \sigma_-)$. Then the quantity R, the ratio of longitudinal to transverse cross section of the virtual photon, can be obtained:

$$R \equiv \frac{\sigma_L}{\sigma_T} = \frac{W_2}{W_1}(1 + \frac{\nu^2}{Q^2}) - 1. \tag{1.18}$$

The differential cross section can be also written in terms of the absorption cross section for transversely and longitudinally polarized photons, σ_T and σ_L, as

$$\sigma = \Gamma_T(\sigma_T + \epsilon\sigma_L) \tag{1.19}$$

where ϵ is the ratio Γ_L/Γ_T, with $\Gamma_T(\Gamma_L)$ being the probability that a lepton emits a transverse(longitudinal) polarized virtual photon. The structure function F_1 and F_2 are related to σ_L and σ_T via

$$\begin{aligned} \sigma_T &= \frac{4\pi\alpha^2}{M\sqrt{\nu^2+Q^2}} F_1(x,Q^2) \\ \sigma_T + \sigma_L &= \frac{4\pi\alpha^2\sqrt{\nu^2+Q^2}}{\nu Q^2} F_2(x,Q^2). \end{aligned} \tag{1.20}$$

One can also define a longitudinal structure function F_L to accompany the purely transverse F_1 by

$$F_L(x,Q^2) = (1+\frac{Q^2}{\nu^2})F_2(x,Q^2) - 2xF_1(x,Q^2). \tag{1.21}$$

It is customary to express the longitudinal component as the ratio of the two absorption cross section, σ_L and σ_T:

$$R = \frac{\sigma_L}{\sigma_T} = \frac{F_L}{2xF_1}. \tag{1.22}$$

Finally, the double differential cross section can be expressed as a function of F_2 and R

$$\frac{d^2\sigma}{dQ^2dx} = \frac{4\pi\alpha^2}{Q^4x}F_2(x,Q^2)\{1 - y\frac{M^2x^2y^2}{Q^2} + \frac{y^2+4M^2x^2y^2/Q^2}{2(1+R(x,Q^2))}\}. \tag{1.23}$$

1.3 The parton model

Deep inelastic scattering from point-like quarks was discovered in the late 1960s at SLAC using 20 GeV electrons in the kinematic range of $2 < Q^2 < 7.5$ GeV^2 [18, 19]. Surprisingly, the data exhibited the scaling behavior, as predicted by Bjorken [6], already at these rather low Q^2 values. In other words, the measured structure function seemed to scale with the resolution of $\lambda \sim \sqrt{Q^2}$ with which the nucleon was probed. This behavior could be only explained by the presence of point-like particles in the nucleon, named as partons by Feynman [20].

In the Bjorken limit, $Q^2 \to \infty$ and $\nu \to \infty$, keeping $x = Q^2/2M\nu$ fixed, the parton model is applicable under several assumptions [21, 22]. Firstly, it is assumed that the leptonic current J_μ couples to quarks. Then the contributions to forward virtual Compton amplitude can be classified by the flow and interactions of quark lines. The second assumption is that at large values of Q^2 the currents, but not the states, may be treated as in free field theory. Thus, final state interactions (b) in Figure 1-2, and vertex corrections (c) in Figure 1-2 are ignored. This leaves the one and two particle contributions shown

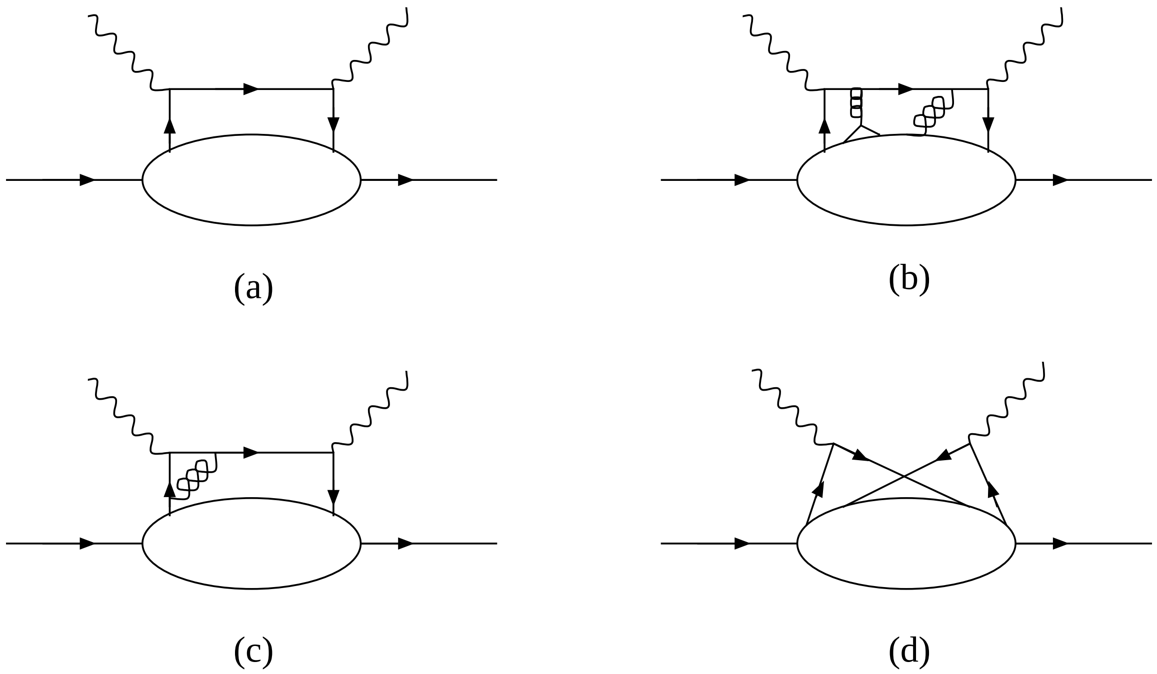

Figure 1-2: Some contributions to forward virtual Compton scattering in QCD: (a) the parton model diagram, (b) final state interactions, (c) vertex correction, (d) interference.

in figures 1-2-(a) and -(d), respectively. However, since the contribution of figure 1-2-(d) vanishes faster by a power of Q^2, the interference diagram (d) can be safely ignored. This leaves now only figure 1-2-(a): the elastic and incoherent scattering of each quark in the target nucleon, i.e. *"quasi-elastic"* scattering.

The variable x has a physical interpretation in an Infinite Momentum Frame (IMF) [23, 24]. With the following choice for the nucleon and vector boson momenta of

$$\begin{aligned} p &= (P + \frac{M^2}{P}, \vec{0}_\perp, P) \\ q &= (\frac{M\nu}{P}, \vec{q}_\perp, 0) \end{aligned} \tag{1.24}$$

and writing the nucleon state $|p>$ as a sum of multiparton states, $|p>= \sum_{i=1}^{n} |k_i>$, the momenta k_i can be express as

$$k_i = (x_i P + \frac{k_{i\perp}^2 + m_i}{2x_i P}, \vec{k}_{i\perp}, x_i P) \tag{1.25}$$

with $\sum_{i=1}^{n} x = 1$. Using the IMF representation, the lifetime of the multiparton state becomes [24, 25]

$$\tau_{partons} \sim \frac{1}{\sum_{i=1}^{n} k_{i0} - p_0} = \frac{2P}{\sum_{i=1}^{n} \frac{k_{i\perp}^2 + m_i}{x_i} - M^2} \tag{1.26}$$

If the interaction time of the vector boson with the partons is given by $\tau_{int} \sim 1/q_0 = P/M\nu$ then the scattering becomes incoherent for $\tau_{parton} \gg \tau_{int}$, i.e.

$$2M\nu + M^2 \gg \sum_{i=1}^{n} \frac{k_{i\perp}^2 + m_i}{x_i}. \tag{1.27}$$

The inequality above only holds if $x_i \neq 0$ or $x_i \neq 1$. The structure function, hadronic $W_{\mu\nu}$, in the parton model is obtained by replacing the intermediate state in 1-2-(a) on-shell. The struck quark and the remnants of the target appear separately as physical intermediate states. These are shown in figure 1-3, which allow us to write the hadronic tensor as

$$W_{\mu\nu}(p,q) = \sum_i \sum_s \int d^4k f_s^i(p,k) \omega_{\mu\nu}^i \delta[(k+q)^2] \tag{1.28}$$

where the sums are taken over the quark flavors i, and quark helicities s. The strong interaction vertex, f_s^i, is a function of the scalar product of p and k. The tensor $\omega_{\mu\nu}^i$ describes the interaction of the virtual photon with the quark of momentum k. This can

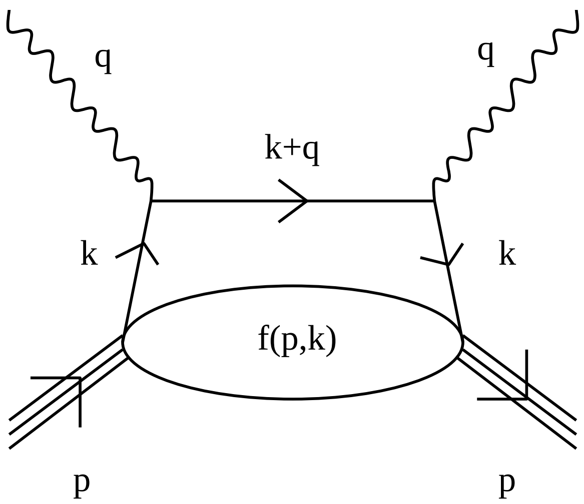

Figure 1-3: The lepton-nucleon scattering in the quark-parton model.

be written in the case of massless on-shell quarks as

$$W_{\mu\nu}(p,q) = \sum_i 2e_i^2 \int \frac{dk^2 dx}{2Mx\mu} q_i(x)\delta(x_i - x) \\ [2k_\mu k_\nu + k_\mu q_\nu + q_\mu k_\nu - g_{\mu\nu} k \cdot q] \tag{1.29}$$

where the function $q_i(x)$ is normally seen as the probability of finding a quark of flavor i with fraction x of the proton momentum. The equation (1.29) can be related to equation (1.6), describing the hadronic tensor. Now the introduced dimensionless structure function $F_1(x)$ can be interpreted as the total sum of the lepton charged quark probability distributions, carrying the momentum fraction x , including the quark-antiquark sea

$$MW_1(p,q) \longrightarrow F_1(x) = \frac{1}{2}\sum_i e_i^2 q_i(x). \tag{1.30}$$

$F_2(x)$ is also defined analogously as the sum of quark-momentum distributions weighted with the lepton charge.

$$\nu W_2(p,q) \longrightarrow F_2(x) = \sum_i e_i^2 x q_i(x). \tag{1.31}$$

We see that the structure functions depend only on one variable x and no longer depend on the scale of the kinematics.

The structure functions F_2 and F_1 are in the QPM directly related via $F_2(x) = 2xF_1(x)$, called the Callan-Gross relation [26], which is only valid if the quarks are spin 1/2 particles. The structure function R goes to zero in the Bjorken limit

$$R = \frac{\sigma_L}{\sigma_T} = \frac{F_2(x) - 2xF_1(x)}{2xF_1(x)} = 0. \tag{1.32}$$

It is important to keep in mind the place of the parton model in QCD. It is valid modulo logarithms: quantities which scale, i.e., become functions of x alone in the parton model, will be modulated by powers of ln Q^2 when QCD interactions are included. Quantities which vanish like a power of Q^2 in the parton model may vanish only like a power of ln Q^2 in QCD.

1.3.1 Quark density distribution

The quark densities in the proton are defined as $u(x) = u_p(x) = u_n(x)$ and $d(x) = d_p(x) = u_n(x)$, where isospin symmetry is assumed between the proton and the neutron. It is convenient to define singlet (S) and non-singlet (NS) quark distributions. The singlet quark distributions are written

$$q^S = \sum_{i=1}^{N_F}(q_i + \bar{q}_i) \tag{1.33}$$

where the sum extends over all flavors, have flavor and baryon quantum numbers equal to zero. The non-singlet quark distributions

$$q^{NS} = q_i - \bar{q}_j \text{ for any i, j, and i } \neq \text{ j} \tag{1.34}$$

have non-zero flavor and baryon quantum numbers. The structure function F_2 for the proton can be written in terms of quark-distribution as

$$F_2^p(x) = \frac{4}{9}[xu(x) + x\bar{u}(x) + xc(x) + x\bar{c}(x)] + \frac{1}{9}[xd(x) + x\bar{d}(x) + xs(x) + x\bar{s}(x)] \tag{1.35}$$

by neglecting quarks heavier than the strange flavor. $F_2^n(x)$ is obtained by interchanging $u \longleftrightarrow d$ and $\bar{u} \longleftrightarrow \bar{d}$. An example of a non-singlet structure function is the difference between the structure functions F_2 for the proton and neutron

$$F_2^p(x) - F_2^n(x) = \frac{1}{3}[xu_v(x) - xd_v(x)]. \tag{1.36}$$

F_2 for the deuteron is an example of a singlet structure function

$$F_2^d(x) = \frac{5}{18}x\sum_i[q_i(x) + \bar{q}_i(x)] - \frac{1}{3}[x\bar{s}(x) - x\bar{c}(x)] \tag{1.37}$$

if the second term is negligible. Here F_2^d is defined per nucleon. The non-singlet quark distribution is governed by the valence quarks. The distribution peaks at $x = 1/3$ and decreases with decrease x. The singlet distribution increases at low x.

The quark-parton model has been widely used in studies of nucleon structure. Although it cannot explain all phenomena, it works impressively well for processes with high momentum transfer. It should be remembered that the scaling violation predicted by QCD is a rather small effect. At $x = 0.5$, the value of F_2 decreases by $\cong 50$ % when going from 1 $\rightarrow$ 25 GeV^2 in Q^2. This change should be compared with that of the elastic proton form factor squared, which falls by a factor of 10^5 over the same Q^2 interval.

1.4 The structure functions in QCD

Although the QPM has been very successful in early DIS experiments, the most precise experimental data show that even in the Bjorken scaling region, the structure functions have a weak Q^2 dependence. To understand this, one must go beyond the QPM to QCD. The lepton quark scattering amplitude involves color radiative corrections, some of which add coherently (e.g. wave function and vertex renomalization) and some of which are incoherent (e.g. bremsstrahlung). Such a radiative process leads to a correction that varies logarithmically with Q^2. The most rigorous approach to the calculation of structure functions and to the description of their Q^2 variation comes from the operator product expansion(OPE) and the renormalization group.

1.4.1 Operator product expansion

It is convenient to write the hadronic tensor in terms of the forward virtual Compton scattering amplitude using the optical theorem, see figure 1-4, as [16, 27, 21]

$$W_{\mu\nu} = \frac{1}{2\pi} Im T_{\mu\nu} \tag{1.38}$$

where $T_{\mu\nu}$ is given by

$$T_{\mu\nu} = i \int d^4 z e^{iqz} < p|T(j_\mu(z) j_\nu(0))|p > . \tag{1.39}$$

Here, T is the time ordering operator, responsible for the hadron propagator introduced through the optical theorem. The Compton amplitude is called *"forward "* since it should be evaluated at zero momentum transfer.

The important feature of the nucleon amplitude is that it is essentially given by a product of two operators j_μ and j_ν which are separated by a distance z_0. In DIS, the distance is nearly lightlike and the OPE in the lightlike limit gives a product of operators, $\tilde{A}$ and $\tilde{B}$, which can be expanded as [27, 21, 28]

$$\tilde{A}(z)\tilde{B}(0) = \sum_i C_i(z^2)\tilde{O}_i(z, 0) \tag{1.40}$$

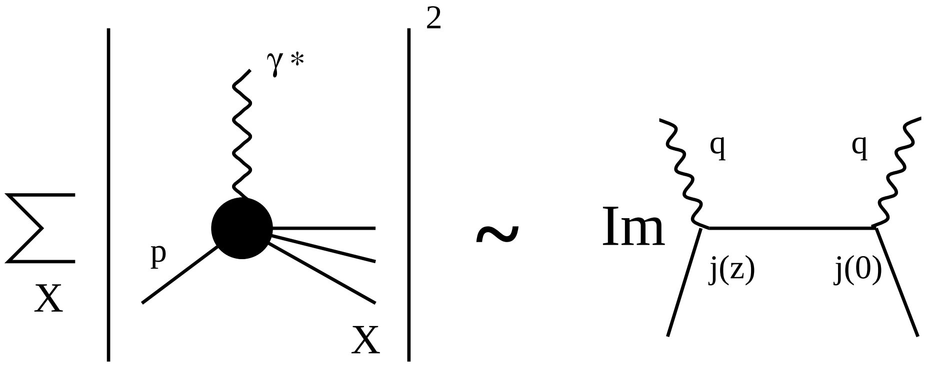

Figure 1-4: Illustration of the optical theorem. The square of the photon nucleon amplitude is related to the imaginary part of the forward photon nucleon amplitude.

where $\tilde{O}_i$ are non-singular operators and the coefficients C_i depend only on z^2. The singularities of (1.40) are placed in these coefficients. $\tilde{O}_i$ is expanded in a Taylor series as

$$\tilde{A}(z)\tilde{B}(0) = \sum_{i,j} C_i^j(z^2) z^{\mu_i,\dots\mu_j} \tilde{O}^{(i,j)}_{\mu_i,\dots\mu_j}(z,0). \tag{1.41}$$

The local operators are symmetric and of spin j. In the lightlike limit, $z^2 = 0$, they are also traceless. From dimensional arguments, the coefficient C must be of the form [27, 21, 28]

$$C_i^j(z^2) \sim (\sqrt{z^2})^{d_{\tilde{O}} - j - d_{\tilde{A}} - d_{\tilde{B}}} \tag{1.42}$$

where d denotes the mass dimension of the corresponding operators. In the lightlike limit (DIS), the term with the smallest exponent in equation (1.42) will give the dominant contribution. Since $d_{\tilde{A}}$ and $d_{\tilde{B}}$ are fixed this will correspond to the minimum of

$$\tau = d_{\tilde{O}} - j, \tag{1.43}$$

the dimension minus the spin of the corresponding operator. This quantity is called twist [29].

The result from the OPE in equation (1.41) is used to replace the current product in equation (1.40) which becomes [27, 21, 28]

$$T_{\mu\nu} = \sum_{i,j} \int d^4 z e^{iqz} C_{i,j}(z^2) z^{\mu_1 \dots \mu_j} < p|\tilde{O}^{(i,j)}_{\mu_i, \dots \mu_j}(z,0)|p > . \tag{1.44}$$

To make further discussion simpler, the Lorentz indices on $T_{\mu\nu}$ are neglected and using the relation, $z^\mu = -i\frac{\partial}{\partial q_\mu}$, equation (1.44) becomes

$$T = \sum_{i,j} (\frac{Q^2}{2})^{-j} q_{\mu_1 .. \mu_j} C_{i,j}(Q^2) < p|\tilde{O}|p > \tag{1.45}$$

where the integral in equation (1.44) has been absorbed in a new definition for the coefficients C. Equation (1.45) shows that the q dependence (momentum of the exchanged photon) of T has totally been separated from the p-dependence (momentum of the exchanged nucleon). This is called the factorization theorem [30, 31] and makes it possible to perform certain calculations on parts of the hadron structure which will give observable predictions.

The non-perturbative matrix element in equation (1.45) can be elaborated further. Since it depends only on the initial momentum of the nucleon, p, it can generally decomposed as

$$< p|\tilde{O}^{i,j}_{\mu_1 .. \mu_j}|p >= A_{i,j} p_{\mu_i} ... p_{\mu_j} + B_{i,j} g_{\mu_a \mu_b} p_{\mu_1} ... \bar{p}_{\mu_a} ... \bar{p}_{\mu_b} ... p_{\mu_j} + ... \tag{1.46}$$

where A and B are coefficients depending on the mass of the nucleon or generally the target mass. If we assume the quark model there is also a dependence on these masses. The bars on the operators indicate that these operators should be dropped and terms not written out contain more than one metric tensor $g_{\mu\nu}$. Inserting this expression in equation (1.45) results in

$$T = \sum_{i,j} C_{j,i}(Q^2) x^{-j} (A_{j,i} + \frac{B_{j,i}}{Q^2} x^2 + ...). \tag{1.47}$$

The term in (1.46) containing the metric tensor is suppressed by $1/Q^2$ compared to the leading term and further terms are suppressed by higher powers of $1/Q^2$.

Now reinstalling the Lorentz indices on T and making use of a decomposition of the hadronic tensor $W_{\mu\nu}$ by substituting a dispersion relation for T [32], an expression for the structure function F_2 is obtained [27, 28]

$$M_{i,j} \equiv \int_0^1 dx x^{j-2} F_2(x, Q^2) = \sum_{i,\tau} (\frac{1}{Q^2}) C_{i,j}(Q^2) H_{i,j}. \tag{1.48}$$

Here C can be calculated by perturbative methods and H is a non-perturbative scalar originating from the coefficients A and B in (1.46) and corresponds in the quark model to the non-calculable quark momentum distributions. The twist τ is an even number (for the unpolarized case) and has a minimum value of two, which can be shown by explicitly constructing contributing operators. In the free field case the coefficients C will be independent of Q^2 and therefore we will recapture the Bjorken scaling phenomenon in the high Q^2 limit where the higher twist term can be neglected. Thus, the QPM result is reproduced by the OPE. In this model, any observed scaling violation must be due to higher twist effects and any deviations from this suggest additional effects coming from interactions in the nucleon causing a Q^2 dependence of the coefficients $C_{i,j}$. This is calculated in QCD and discussed in the next section.

1.4.2 The renormalization group equation

The Q^2 dependence of the coefficients in (1.48) can be obtained by applying the renormalization group equation (RGE) [33, 27, 28] which is the assumption that observable quantities must stay unchanged after a change of the renomalization scale. This will reveal the dynamics of the applied theory, in this case QCD.

M_j, the moment of F_2, is a measurable quantity. Since the scalars H_{ij} in equation (1.48) correspond to the quark momentum distributions they will separately obey the renormalization group equation. This means that an equation for the coefficients can be derived and the result is [34, 28]

$$[\mu\frac{\partial}{\partial\mu} + \beta(g)\frac{\partial}{\partial g} - \gamma(i)]C_{i,j}(Q^2, \mu, g) = 0 \tag{1.49}$$

where μ is the renormalization scale, $\beta = \mu dg/d\mu$, g is the coupling strength, and γ is the anomalous dimension of the corresponding operator. The solution of this equation will give the Q^2 dependence of the moment of the structure functions which will be governed by the anomalous dimension γ. This quantity is determined by the renormalization factor of the contributing operator obtained by applying the Feynman rules to the relevant diagram. In the non-singlet case, which is particularly simple since the gluon distribution does not enter, and in lowest order and lowest twist, the solution for C is

$$C_j^{NS}(Q^2, g(\mu)) = C_j^{NS}(Q_0^2, g(\mu))(\frac{\ln t}{\ln t_0})^{d_j^{NS}} \tag{1.50}$$

where $t = Q^2/\Lambda^2$ and

$$d_j^{NS} = \frac{-\gamma_{0,NS}(j)}{2\beta_0} = \frac{16}{33 - 2n_f}[\frac{1}{2j(j+1)} + \frac{3}{4} - \sum_{n=1}^{1}\frac{1}{n}] \tag{1.51}$$

and Λ is the QCD mass scale. The zero indices mean that the quantities are given in lowest order.

Ignoring the momentum dependence of the coupling strength, it is clear that the Q^2 dependence of the non-singlet moments is controlled by the anomalous dimension. This is also true for the singlet case (quantities that are gluon dependent are called singlet). As a special case, consider only operators of spin 1 contributing to the moment in equation (1.48). Then $j = 1$ and the anomalous dimension will vanish. The integral

$$\int_0^1 \frac{F_2^p(x, Q^2) - F_2^n(x, Q^2)}{x}dx \tag{1.52}$$

where n and p denotes neutrons and proton, will then be Q^2 independent although the integrand itself depend on Q^2. Other integrals, such as the Bjorken sum rule [35] in spin dependent physics and that of F_3 [36] will also by the same reason be Q^2 independent. The observation of a momentum dependence of these integrals must then be evidence for the running of the strong coupling strength which has never been observed in deep inelastic scattering. Equation 1.52 was first calculated by Gottfried [12] in the naive quark model and has been measured experimentally by NMC [13].

1.4.3 QCD-improved parton model

The parton model can be viewed as the zero order to the perturbative expansion of QCD in powers of α_s, where α_s is the effective coupling strength of the strong interaction. In leading order correction, the Q^2 dependence of the coupling constant is written as [37]

$$\alpha_s^{LO}(Q^2) = \frac{4\pi}{\beta_0 \ln Q^2/\Lambda^2}. \tag{1.53}$$

In next-to-leading order (NLO) [37]

$$\alpha_s^{NLO}(Q^2) = \alpha_s^{LO}(Q^2)[1 - \frac{\beta_1}{\beta_0}\frac{\ln(\ln(Q^2/\Lambda^2))}{\ln(Q^2/\Lambda^2)}] \tag{1.54}$$

where $\beta_0 = 11 - \frac{2}{3}N_F$ and $\beta_1 = 102 - \frac{38}{3}$. Asymptotic freedom is expressed explicitly in equation (1.54) where α_s approaches zero as Q^2 goes to infinity. In leading order perturbative QCD, α_s describes the coupling in the Feynman diagrams (see figure 1-5). The structure function F_2 can still be viewed as a sum of momentum weighted quark distributions in leading order perturbative QCD, but now as function of both x and Q^2

$$F_2(x, Q^2) = \sum_i e_i^2 x q_i(x, Q^2). \tag{1.55}$$

In NLO, the relation between F_2 and the quark distributions become non-trivial.

The processes illustrated in figure 1-5 induce the scale violation of the structure function F_2. Intuitively it can be viewed that partons carrying a large fraction of nucleon momentum have an increased probability to emit a gluon. Hence, they lose momentum as Q^2 is

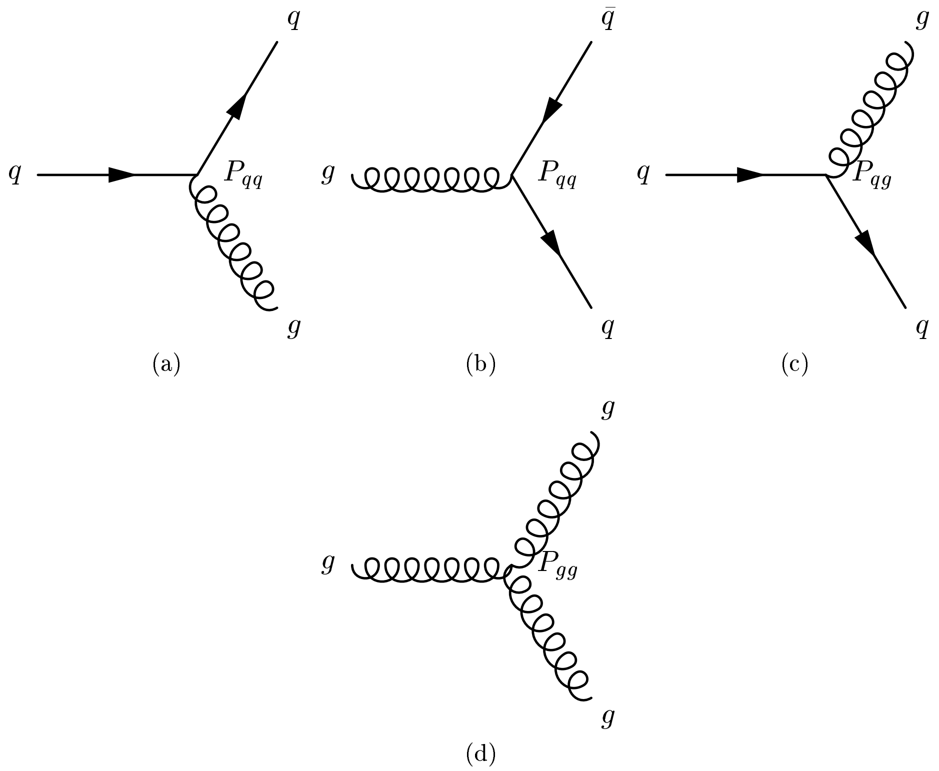

Figure 1-5: Interactions of quarks and gluons relevant to Q^2 evolution in leading order perturbative QCD.

increased. The parton distributions as a function of x will be shifted to lower values in x as Q^2 becomes larger. This effect is visualized in figure 1-6.

The parton distribution as a function of x will be shifted to lower values in x as Q^2 becomes larger. These processes [38] are described by the *splitting kernels* or *splitting functions* $P_{ab}(z)$ which can be interpreted as the probability of finding a quark q or gluon g with the momentum fraction x produced by a parton q or g with momentum fraction of y. When the scale changes by dQ^2 from Q^2, a positive contribution arises when the parent quark of an interacting quark emits a gluon. There is also a negative contribution arising from quarks that had momentum x before emitting a gluon. These two contributions can

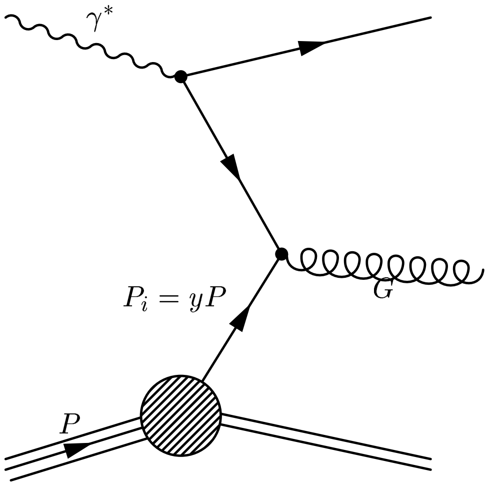

Figure 1-6: Interactions of quarks and gluons relevant to Q^2 evolution in leading order perturbative QCD.

be written in an integral-differential equation as [38]

$$\frac{dq^{NS}}{d\ln Q^2} = \frac{\alpha_s}{2\pi} P_{qq} \otimes q^{NS} \tag{1.56}$$

with

$$P \otimes q = \int_x^1 \frac{dy}{y} P(x/y) q(y) \tag{1.57}$$

for the non-singlet (NS) quark distributions. Similarly, the quark singlet (S) and the gluon distributions follow

$$\frac{dq^S}{d\ln Q^2} = \frac{\alpha_s}{2\pi}[P_{qq} \otimes q^S + N_f P_{qg} \otimes G] \tag{1.58}$$

$$\frac{dG}{d\ln Q^2} = \frac{\alpha_s}{2\pi}[P_{gq} \otimes q^S + P_{gg} \otimes G] \tag{1.59}$$

where the splitting functions P_{qg}, P_{gq}, and P_{gg} are related to Figure 1-5-(a), -(b), and (c) respectively. Every quark distribution and structure function can be decomposed into a singlet and a non-singlet distribution. The optimal coefficients of the parametrized effective quark and gluon distributions and α_s were found by minimizing the difference between the measured structure function F_2 for the proton and deutron and calculated structure function to the next-to-leading order pQCD. There are two major corrections that have to be applied:

- In all preceding formulae the mass of the nucleon target has been neglected. At low $Q^2 \sim 1$ GeV^2/C this effect becomes important. By changing the Bjorken scaling variable

$$x \to x \frac{2}{1+\sqrt{1+\frac{4M^2x^2}{Q^2}}} \tag{1.60}$$

the resulting structure functions evolve according to the DGLAP (Dockshitzer-Gribov-Lipatov-Altarelli-Parisi) evolution equations [38] which are given by

$$\frac{dq_i(x,Q^2)}{d\ln Q^2} = \frac{\alpha_s(Q^2)}{2\pi}\int_x^1 \frac{dy}{y}\left(q_i(y,Q^2)P_{qq}\left(\frac{x}{y}\right) + G(y,Q^2)P_{qG}\left(\frac{x}{y}\right)\right), \tag{1.61}$$

$$\frac{dG(x,Q^2)}{d\ln Q^2} = \frac{\alpha_s(Q^2)}{2\pi}\int_x^1 \frac{dy}{y}\left(\sum_i q_i(y,Q^2)P_{Gq}\left(\frac{x}{y}\right) + G(y,Q^2)P_{GG}\left(\frac{x}{y}\right)\right). \tag{1.62}$$

- The existence of spectator quarks in the quark-photon interaction becomes important at low values of Q^2. This effect has a $1/Q^2$ behavior and therefore the structure function F_2 is normally parametrized as

$$F_2(x,Q^2) = F_2^{LT}(x,Q^2)[1 + h(x)/Q^2] \tag{1.63}$$

and the term F_2^{LT} is given by next-to-leading order QCD.

So far, the perturbative techniques of QCD do not allow for any predictions of the quark or gluon distributions as a function of x. These have to be obtained from experiments.

However, if the distributions are known at a given value of Q^2, say Q_0^2, perturbative QCD can predict the distributions for all values of Q^2, via the DGLAP equation.

As quarks can emit gluons they obtain transverse momentum and therefore QCD predicts a non-zero value of R, via the Altarelli-Martinelli equation [39]

$$R(x,Q^2) = \frac{F_L(x,Q^2)}{(1+4M^2x^2/Q^2)F_2(x,Q^2) - F_L(x,Q^2)} \tag{1.64}$$

and

$$F_L(x,Q^2) = \frac{\alpha_s(Q^2)}{\pi}x^2 \int_x^1 \frac{dy}{y^3}(\frac{4}{3}F_2(y,Q^2) + 2\sum_i e_i^2(1-\frac{x}{y}yG(y,Q^2))). \tag{1.65}$$

1.5 Nuclear effects in structure functions

The distribution of quarks in a nucleus has been found experimentally to differ significantly from the distribution of quarks in the free nucleon. This came as a surprise when the European Muon Collaboration (EMC) measured the ratios of structure functions of iron(Fe) and deuterium in DIS scattering of muons [7]. There has been an intensive effort to understand this result and to produce a better understanding of the QPM and the implications of QCD in the nuclear many body system. In this section, the existing experimental information on nuclear effects in structure functions will be summarized and the theoretical models which attempt to explain the data (the very detailed reviews in [27, 40]) will be briefly discussed.

Figure 1-7 presents the measured structure function ratios F_2^A/F_2^d for ^{40}Ca and ^{56}Fe from various experiments. F_2^A is the structure function per nucleon of a nucleus with mass number A and $F_2^d(=F_2^D)$ refers to deuterium (^2H). In the absence of nuclear effects, the ratio F_2^A/F_2^d is normalized to unity. By neglecting small nuclear effects in the deutron, F_2^d is taken to be the isospin averaged nucleon structure function. As seen in figure 1-7, with several distinct regions of x, the nuclear effects can be characterized as a shadowing effect ($x \lesssim 0.1$), an anti-shadowing effect ($0.1 \lesssim x \lesssim 0.2$), the EMC effect ($0.3 \lesssim x \lesssim 0.8$), and the effect of Fermi motion ($x \gtrsim 0.8$).

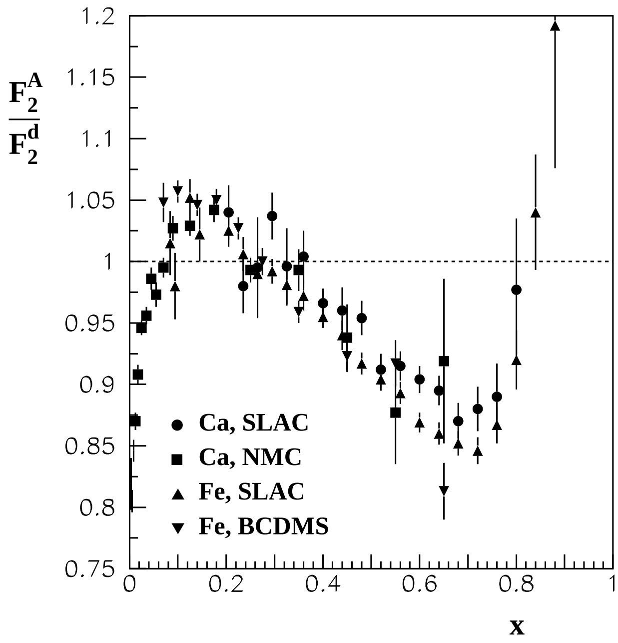

Figure 1-7: The structure function ratios F_2^A/F_2^d for ^{40}Ca and ^{56}Fe. The data are take from NMC([41]), SLAC([42]), and BCDMS([43]). This plot was directly taken from the reference [40].

- **Shadowing effect**

  In the range of $x \lesssim 0.1$ one observes a systematic reduction of the structure function ratio of F_2^A/F_2^d. The measurements of E665 at FERMILAB [44, 45, 46] and NMC [41, 47, 48, 49, 50] at CERN provide detailed and systematic information on this phenomenon in a range of nuclear targets from ^4He to ^{208}Pb.

  The usual treatment of shadowing is based on a simple two-phase process , i.e. the vector meson dominance(VMD) model for low Q^2 and a virtual photon interaction through the Pomeron for high Q^2, at the phenomenological level. According to this picture, the virtual photon interacts with the nuclear target via its fluctuations into $q\bar{q}$ pairs. If the virtuality of the photon is larger, then the fluctuation is spatially small and a parton description is relevant. However, if the virtuality is small, a VMD picture is appropriate. The shadowing effect is thought to depend only weakly on Q^2. The most precise investigation of shadowing effect has been performed by NMC [41, 47, 48, 49, 50] and has revealed shadowing decreases at most linearly with $\ln Q^2$ for $x < 0.1$.

- **Anti-Shadowing effect**

  The NMC data have established a small but statistically significant enhancement of the structure function ratio at $0.1 < x < 0.2$. The observed enhancement is of the order of a few percent and no significant Q^2 dependence is observed.

- **The EMC effect**

  The region of intermediate $0.2 < x < 0.8$ shows depletion of the structure function ratio F_2^A/F_2^d [51]. The measured structure function ratios decrease with rising x and have a minimum at $x \sim 0.6$. The magnitude of this depletion grows approximately logarithmically with the nuclear mass number A. The depletion is commonly explained with the description of rescaling models [27]. These models rescale either x (because the effective mass M is lower for bound nucleons) or Q^2 (because the radius of bound nucleons R_N is larger). Hence, the width of the Fermi motion of valence quarks $\delta x \sim \frac{1}{R_N M_q}$ becomes smaller.

- **Fermi-motion**

  The increase of the structure function for bound nucleons at large $x(> 0.8)$ due to the Fermi motion inside the nucleus.

1.5.1 Nuclear shadowing in DIS

The experimental observation that the total γ^*-nucleus cross section at small x is smaller than A times the γ^*-nucleon cross section,

$$\sigma_{tot}^{\gamma^* A} < A\sigma_{tot}^{\gamma^* N} \tag{1.66}$$

is called shadowing. Depending on the reference frame, different physical pictures are considered. In the Breit frame, the nucleus appears contracted and parton fusion leads to a reduction of the parton density in the low x region [52, 53, 54]. A very intuitive picture arises in the rest frame of the nucleus, where shadowing may be understood qualitatively in the following way: The virtual photon fluctuates into a hadronic state ([55, 56, 57, 58, 59, 60, 61, 62]) that interacts with the nucleus at it's surface and the nucleons inside have less probability to interact with the photon. Thus, the total cross section is smaller than expected naively.

In the rest frame of the nucleus, since the hadronic states must have the same quantum number as the photon, it is reasonable to write the physical photon as a superposition of vector mesons. This idea leads to the (generalized) vector meson dominance model (G)VMD. The fluctuation extends over a distance called the coherence length

$$L_c = \frac{2\nu}{Q^2 + M_X^2} \tag{1.67}$$

where M_X is the invariant mass of the fluctuation of the virtual photon. For small x this coherence length can become larger than the nuclear radius R_A. In the hadronic basis, the shadowing correction is given by [63]

$$\frac{\sigma^{tot}_{\gamma^* A}}{A\sigma^{tot}_{\gamma^* N}} = 1 - \frac{4\pi < T >}{\gamma^* N} \int d^2b \int dM_X^2 \left[\frac{d^2(\gamma^* N \to XN)}{dM_X^2 dt}\right]_{t=0} F_A^2(L_c, b) \tag{1.68}$$

in the double scattering approximation. For the case, $L_c \sim R_A$, the finite size of the nucleus has to be taken account. This is encoded in the nuclear form factor $F_A^2(L_c, b)$ given by

$$F_A^2(L_c, b) = \frac{1}{A < T >} \left| \int_{-\infty}^{\infty} dz n_A(b, z) e^{iz/L_c} \right|^2 \tag{1.69}$$

with

$$< T > = \frac{1}{A} \int d^2b T^2(b). \tag{1.70}$$

Here, $T(b) = \int_{-\infty}^{\infty} dz n_A(b, z)$ is the nuclear thickness and b is the impact parameter.

1.6 The world data for $F_2(x, Q^2)$ and $R(x, Q^2)$

Figure 1-8 citebib:mallot shows F_2 as function of Q^2 for various values of x. The scaling of the structure function, as expected if the proton was made from point-like, non-interacting partons, can be observed in the valence region at $x \sim 0.3$. At low x, however, the quark-gluon interactions must be considered, and from the observed scaling violation the gluon density, being responsible for the rise of F_2 at low x, can be extracted to a precision of $\sim$ 10%. Next to leading order (NLO) QCD fits by the H1 collaboration are in good agreement with the data over the entire kinematic range, even for Q^2 values as low as 1 GeV^2.

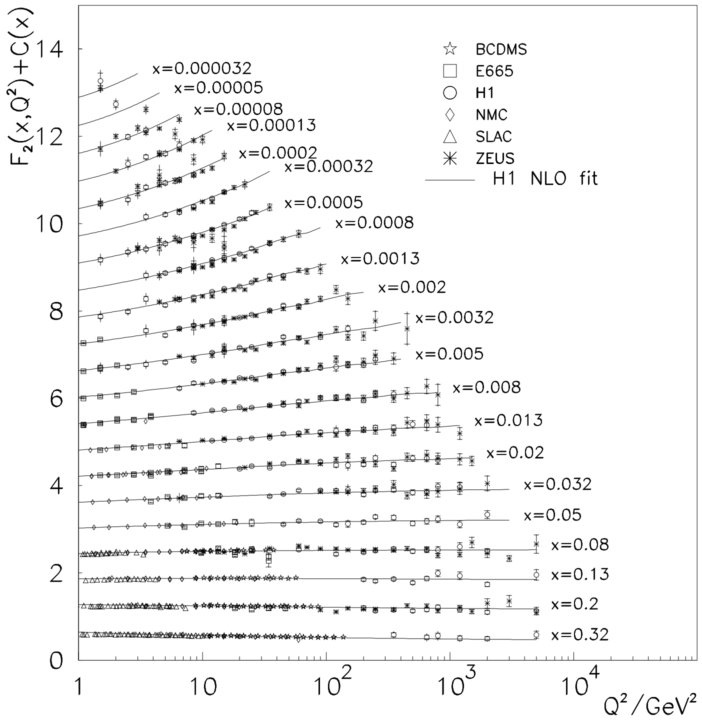

Figure 1-8: The world data set for F_2 [64]. The constant $C(x)$ is defined by $C(x) = 0.6(i - 0.4)$ with x bin number i and $i = 1$ for $x = 0.32$. In the small x region a steep rise of $F_2 \sim x^{-\lambda}$ is observed for decreasing x indicating strong scaling violations of F_2.

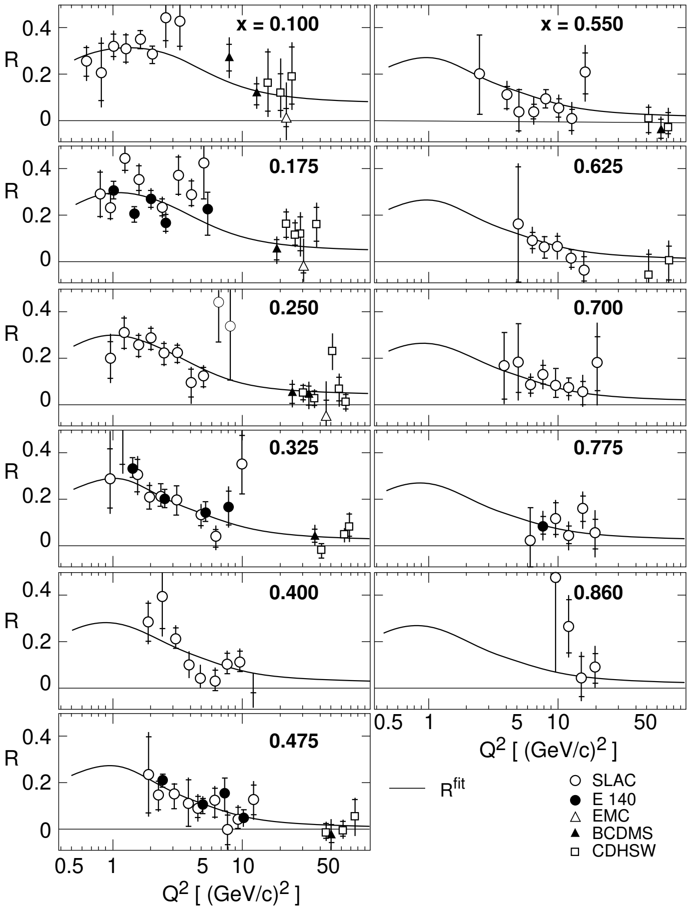

Figure 1-9: SLAC global analysis of $R(x, Q^2)$ data [65]. The solid curve is a parametrization of the measurements of R which is widely used as R1990. It should be noted that there are no data below $x < 0.1$ in this SLAC global analysis. However, the HERMES experiment takes data down to $< x >= 0.01$ with $< Q^2 >= 0.5$ GeV^2.

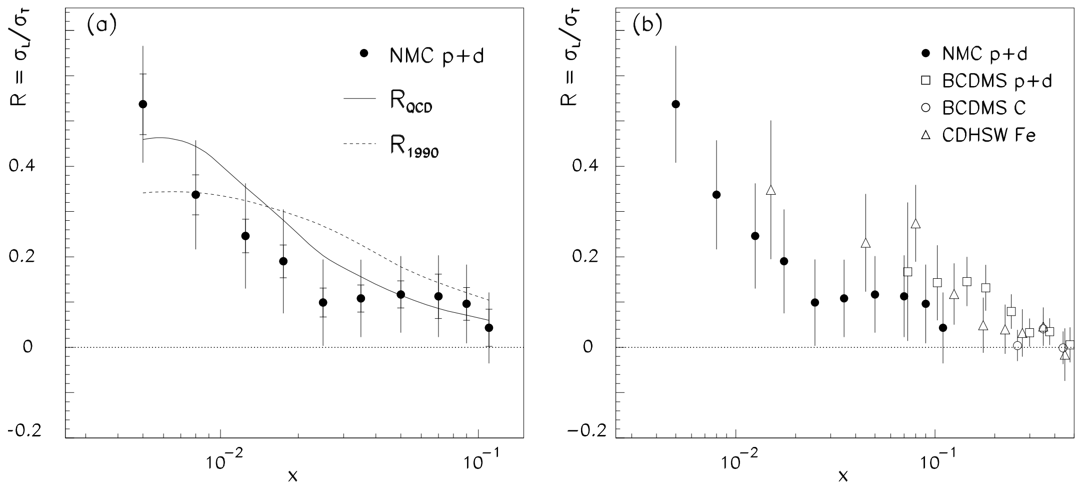

Figure 1-10: (a) NMC measurement of R as function of x with the parametrization of the R1990 (solid line) and R_{QCD} (dashed line). (b) Comparison with several other experiments.

The measurement of the structure function R as function of Q^2 is shown in figure 1-9. The result of a comprehensive global analysis [65] of the SLAC data on $R(x, Q^2)$ and some high Q^2 muon and neutrino data from CERN resulted in a phenomenological parametrization for R, often referred to as R1990. The kinematic region covered is $0.1 < x < 0.9$ and $0.6 < Q^2 < 20$ GeV^2 for the SLAC data and up to about 80 GeV^2 for the muon and neutrino data. The ratio R is rather well determined for intermediate x and Q^2, where it is found to be small. However, the behavior in the region $x < 0.1$ is uncertain. New data from the NMC experiment [66] in the small x region, $0.002 < x < 0.12$, are shown in figure 1-10. The data agree well with the rise expected from perturbative QCD and previous measurements in the region of overlap. Also, preliminary neutrino data for R from the CCFR collaboration [67] for $0.01 < x < 0.6$ and $Q^2 > 4$ GeV^2 agree well with R_{QCD}. The A-dependence of R has not been reported yet and it is shown in figure 1-11. However, its A-dependence has not been studied for low values of Q^2 and x.

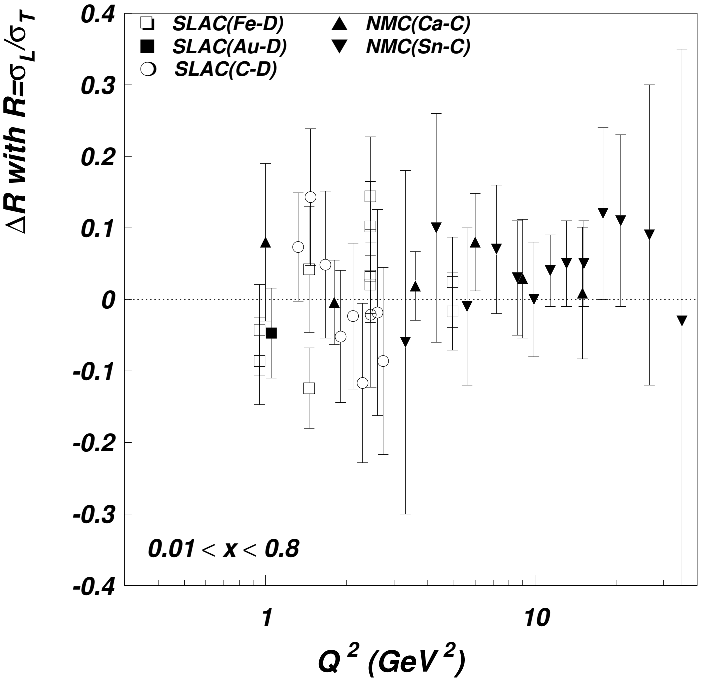

Figure 1-11: The A-dependence of R as function of Q^2 is shown. Here ΔR with $R = \sigma_L/\sigma_T$ is given by the differences of R for various targets, $\Delta R = R_{A_1} - R_{A_2}$ where A_1 and A_2 are nuclear targets.

Chapter 2

The HERMES experiment

The HERMES experiment was designed to study the spin structure of the nucleon using spin-dependent deep inelastic scattering. The experiment has contributed a high quality set of precise inclusive data to improve the world spin physics data set for the proton and the neutron. HERMES has also provided new precise semi-inclusive data using the forward acceptance of the spectrometer combined with excellent hadron identification and the purity of the internal polarized target.

At the HERMES experiment, longitudinally polarized positrons of energy 27.5 GeV are scattered from polarized internal gas targets. The beam polarization was continuously measured by Compton back-scattering and reached typical values of 55% with a systematic fractional uncertainty in the measurement of 3.4%. The HERMES polarized proton target is formed by injecting a nuclear-polarized beam of atomic hydrogen into a tubular open-ended storage cell. The target polarization was 0.79 ± 0.06 in 1996 and 0.88 ± 0.04 in 1997, where the quoted errors are systematic. In addition to studying polarized DIS using $\vec{H}$, $\vec{D}$, and $^3\vec{He}$ targets, the unpolarized data has been collected with H_2,$^2H_2$ $(= D_2)$, ^3He, and $^{14}N_2$ gases within a relatively short period of time with high statistics data sets. These data were used in the work described in this thesis.

The HERMES detector is a forward spectrometer with a dipole magnet providing an integrated field of 1.3 Tm. The magnet is divided into two identical sections by a horizontal iron plate that shields the positron and proton beams from the magnetic field. Consequently, the spectrometer consists of two identical detector systems, upper and lower, with a minimum polar angle for the acceptance of particles produced from the target region of 40 mrad. The maximum angular acceptances are ±140 mrad vertically and ±170 mrad horizontally. For charged particles with momenta from 4.5 to 27 GeV/c, the average momentum resolution $\Delta p/p$ is about 1%.

Particle identification (PID) is accomplished using a lead-glass electromagnetic calorimeter, a scintillator hodoscope preceded by two radiation lengths of lead, a six-module transition radiation detector, and a C_4F_{10}/N_2(70:30) gas threshold Čerenkov counter. The Čerenkov counter may also be used to identify pions with momenta between 4.5 and 13.5 GeV/c. Each component of the experiment will now be described in greater detail.

2.1 The HERA accelerator facility

The Hadron-Electron Ring Accelerator facility (HERA) is located at the Deutsches Elektronen-Synchrotron (DESY), in Hamburg, Germany. It collides electrons and protons at high energies. The electron and proton storage rings share the same tunnel, which is 6.335 km in circumference. A schematic layout of the HERA electron ring is presented in Fig. 2-1. Two other experiments (ZEUS and H1) take data using the collider mode of the accelerator to study ep interactions at high energies. The HERA-B experiment is in the commissioning stage and will collide the HERA proton beam with wire targets to search for CP violation in the B meson system. The HERMES experiment uses only the HERA electron ring, colliding it with a fixed internal gaseous target. The electrons circulating in the ring are arranged in 210 bunches, 96 ns apart. Each bunch contains 3.8×10^{10} electrons. The bunch length is 27 ps. The current in the ring typically reaches 30 mA.

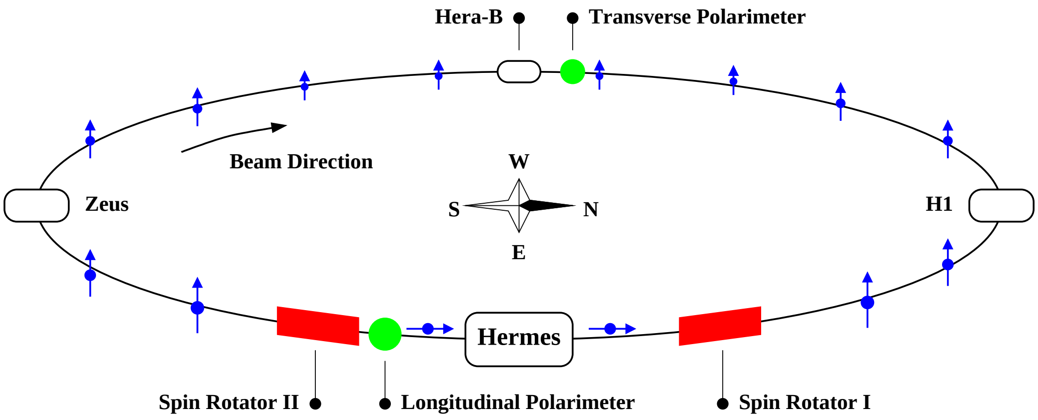

Figure 2-1: Schematic layout of the HERA accelerator. The positions of the four experiments making use of the ring (H1, HERMES, Zeus, and HERA-B) are shown, along with the positions of the two beam polarimeters and the spin rotators on either side of the HERMES experimental site.

In 1996 and 1997, HERA was operated using positrons as opposed to electrons. Positrons were used because the stored beam lifetime was substantially longer. The positrons repel positively charged ions created in collisions with residual gas in the imperfect vacuum of the ring, keeping them away from the beam axis. The ring uses a series of RF cavities to bring the positrons to energies of 27.6 GeV from the injected energy of 14 GeV. Polarization in the ring is built up over time via the Sokolov-Ternov effect [68, 69]. Sokolov and Ternov discovered that the synchrotron radiation of a circulating lepton beam will have an asymmetry. The asymmetric emission of synchrotron radiation gives rise to transverse polarization of the electrons in the ring. For electrons (positrons) the polarization is antiparallel (parallel) to the magnetic field used to bend the leptons in the synchrotron. The polarization increases with time according to the relation:

$$P(t) = P_{\max}(1 - e^{-t/\tau}) \tag{2.1}$$

where τ is the time to accumulate polarization and $P_{\max}$ is the asymptotic limit. For an ideal flat machine the maximum asymptotic limit is $P_{\max}^{\mathrm{ST}} = 0.92$. Depolarizing effects in a real machine result in a lower limit. At HERA a typical polarization maximum is $P_{\max}^{\mathrm{HERA}} = 0.55$.

For an ideal HERA machine running at 27.6 GeV, the time constant $\tau^{\mathrm{ST}} = 37$ min. Adding depolarizing effects with a typical depolarizing time τ^{D} will decrease this time according to:

$$\frac{1}{\tau} = \frac{1}{\tau^{\mathrm{ST}}} + \frac{1}{\tau^{\mathrm{D}}} \tag{2.2}$$

and will also decrease the maximum attainable polarization:

$$P_{\max} = P^{\mathrm{ST}}_{\max} \frac{\tau}{\tau^{\mathrm{ST}}}. \tag{2.3}$$

The transverse polarization is converted into linear polarization at the HERMES experimental site using spin rotators. Spin rotator I rotates the spin of the incident positrons into a longitudinal state before they reach the HERMES experiment. Spin rotator II rotates this longitudinal polarization back to the transverse direction of the rest of the ring after the positrons have passed through the HERMES experiment. For a non-flat machine (i.e. a machine with spin rotators), the above equation for $P_{\max}$ is modified with a multiplicative factor $(1+\delta)$ due to depolarizing effects from the spin rotators. The rise with time of the polarization of positrons in the HERA ring with spin rotators is shown in Fig. 2-2.

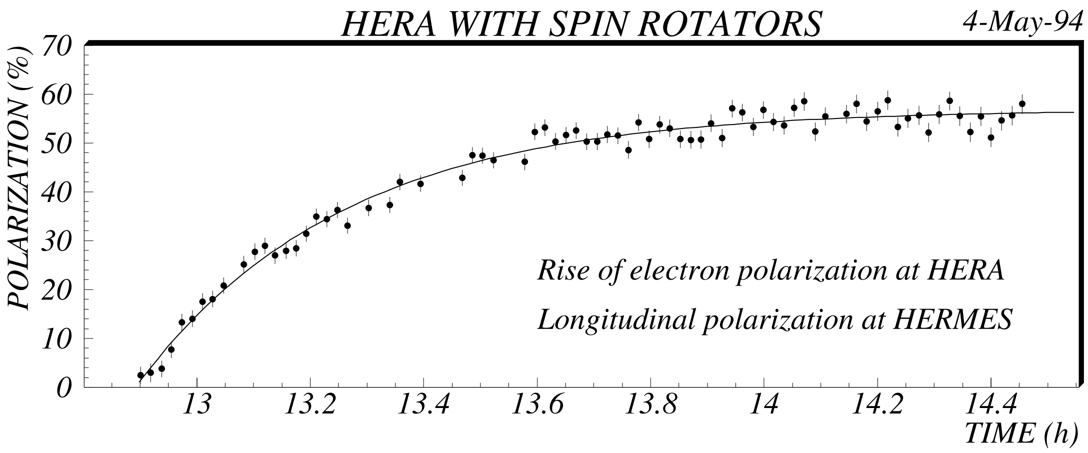

Figure 2-2: The rise of polarization in the HERA ring with spin rotators.

Two beam polarimeters continuously measure the polarization in the ring [69]. Both use high power lasers to backscatter circularly polarized Compton photons from the electrons in the ring. The transverse polarimeter measures the vertical polarization of the electrons in the ring and the longitudinal polarimeter measures the longitudinal polarization of the electrons in the ring near the HERMES interaction point.

The cross-section for the scattering of the polarized photons is dependent on the polarization of the electrons. Since only vertical (P_y) and longitudinal (P_z) components of the electron polarization $\mathbf{P}$ are measured, integrating over the horizontal component leads to:

$$\frac{d\sigma_c}{d\Omega}(\mathbf{S}, \mathbf{P}) = \frac{1}{2} r_0^2 \left(\frac{k_f}{k_i}\right)^2 [\Sigma_0 + S_1\Sigma_1 + S_3(P_y\Sigma_{2y}) + P_z\Sigma_{2z}] \tag{2.4}$$

where S_1 and S_3 are the linear and circular components of the initial photon polarization $\mathbf{S}$, r_0 is the classical electron radius, and k_i and k_f are the initial and final photon momenta in the electron rest frame. $\Sigma_{0,1,2y,2z}$ are unpolarized, single and double polarized cross sections. Σ_{2y} is used for the transverse measurement and Σ_{2z} for the longitudinal measurement.

The two polarimeters will now be described.

2.1.1 The Transverse Polarimeter

The HERA transverse polarimeter and the associated systematic error for its measurement of the beam polarization are described in detail in Ref. [70]. The transverse polarimeter is located across the HERA ring from the HERMES experiment in the West Hall. A schematic layout of the transverse polarimeter is displayed in Fig. 2-3. This polarimeter was commissioned in 1991.

An argon-ion laser provides a continuous 10 W beam of circularly polarized 2.41 eV photons which collides with the HERA electron beam. Lenses and mirrors transport the laser beam roughly 200 m to the interaction point with the electron beam. A Pockels cell is used to switch the photon polarization with a frequency of 90 Hz. The energy and

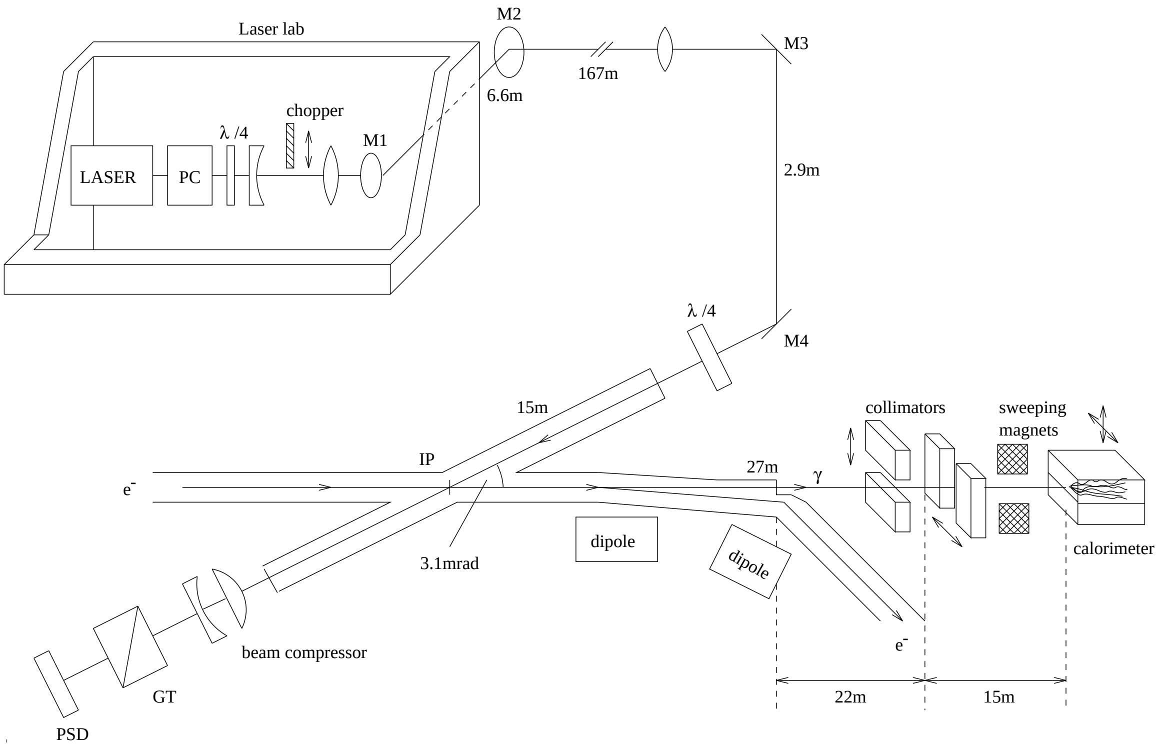

Figure 2-3: The HERA Transverse Polarimeter.

the vertical position of the backscattered Compton photons are measured in a tungsten-scintillator calorimeter located 65 m from the interaction point. The calorimeter is split into essentially identical upper and lower halves to give position sensitivity in the vertical direction.

The laser intensity is chosen so that the probability for multiple Compton photons per bunch crossing is about 1%. In this way, the energy and position of each detected photon is used for the analysis. This is commonly known as the "single photon method". By measuring the asymmetry of the energies of the photons detected in the upper and lower calorimeter $\eta(\langle y\rangle) = (E_{\text{upper}} - E_{\text{lower}})/(E_{\text{upper}} + E_{\text{lower}})$, one can determine the mean vertical position $\langle y\rangle$.

The standard method of determining the polarization P_y is from the shift of the mean vertical positions $\langle y \rangle$ measured with left and right circularly polarized light:

$$\Delta\langle y\rangle(E_\gamma) = \frac{1}{2}(\langle y\rangle_L - \langle y\rangle_R) = P_y \Delta S_3 \Pi(E_\gamma) \tag{2.5}$$

where the analyzing power $\Pi(E_\gamma) \simeq 170\,\mu$m is determined using the η to $\langle y \rangle$ transformation with the polarized cross section Σ_{2y}. The analyzing power is a function of the photon energy, measured using $E_\gamma = E_{\mathrm{upper}} + E_{\mathrm{lower}}$. The statistical precision in the transverse polarization δP_y is roughly 0.01 to 0.02 per minute.

2.1.2 The Longitudinal Polarimeter

In 1996 a second Compton polarimeter (the Longitudinal Polarimeter) was commissioned. The longitudinal polarimeter is located in the HERA tunnel roughly 50 m downstream of the HERMES experiment, before spin rotator II rotates the polarization back into its transverse state in the ring. Unlike the transverse polarimeter, the longitudinal polarimeter uses the energy distribution asymmetry of Compton photons to determine the longitudinal beam polarization $A(E_\gamma) = \Delta S_3 P_z \Sigma_{2z}$. It also uses a "multi-photon method", measuring the total energy deposited in the detector by roughly 1000 Compton photons per bunch crossing. This method is used to overcome large backgrounds from Bremsstrahlung photons which would swamp the single photon method used by the transverse polarimeter.

The layout of the longitudinal polarimeter optical path is shown in Fig. 2-4. A frequency doubled, pulsed YAG laser produces 2.3 eV photons at typically 100 Hz with pulse energies from 1-250 mJ. The laser beam is guided with remotely controlled mirrors and lenses through a 72 m long vacuum pipe to the interaction point with the electron beam. A Pockels cell switches the photon polarization with a frequency of 89 Hz. The backscattered photons are detected in a calorimeter located 54 m downstream of the interaction point. It consists of four $NaBi(WO_4)$ Cerenkov crystals, arranged in a 2×2 array. The energy of the photons is the sum of the energy detected in the four segments. The segmentation allows a determination of the x-y position of the photons. The calorimeter table is periodically

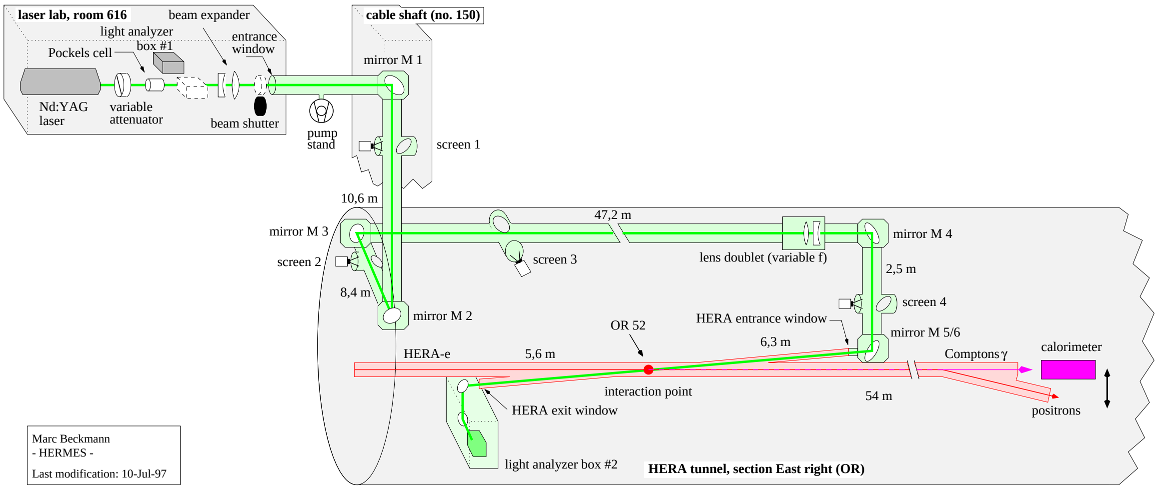

Figure 2-4: The longitudinal polarimeter

recentered using this information, if the scattered Compton photons drift too far towards the edge of the calorimeter. The recentering is necessary typically a few times per fill, due to shifts in the HERA beam position.

The longitudinal polarimeter can achieve a statistical error δP_z of 0.01 in about 40 s. The laser power is typically adjusted to keep the luminosity seen in the calorimeter constant. The bremsstrahlung background can be measured between laser pulses, but is found to be small in multi-photon mode.

2.2 The Internal Gas Target

A variety of polarized and unpolarized internal gaseous targets are available to the experiment.

The HERMES polarized target is formed by injecting a nuclear-polarized beam of ^{1}H, ^{2}H or ^{3}He into a tubular open-ended storage cell. Two different target technologies have provided polarized nuclei for study. In 1995, a source of polarized ^{3}He was used. The ^{3}He target becomes polarized through metastability-exchange optical pumping [71]. Typical polarizations were near 50% with an areal density of 1.0×10^{15} nucleons/cm^2. In 1996 and 1997, a polarized ^{1}H source was used. An atomic beam source uses permanent sextuple magnets and radio-frequency transitions to select the desired hyperfine states [72]. The target polarization was typically 80%, with an areal density of 7×10^{13} nucleons/cm^2. From 1998 to 2000, a polarized atomic deuterium source will be used, also based on atomic beam source technology. The polarized targets are used mainly to study polarized semi-inclusive deep-inelastic scattering and polarized photoproduction.

In addition to polarized targets, HERMES can also use unpolarized targets. These targets are supplied using the HERMES Unpolarized Gas Feed System. The unpolarized gaseous targets used to date are H_2, D_2, ^{3}He, and N_2. Although unnecessary for the photoproduction spin asymmetries that are the subject of this thesis, these targets have been used to extract many fascinating physics results, including:

- unpolarized structure function ratios,
- nuclear transparency of diffractive incoherent ρ^0 meson production [73],
- nuclear attenuation of charged pion production,
- ρ and ϕ angular decay distributions [74],
- spin transfer of the polarized electron beam to polarized Λ baryons in the final state [75].

The gas feed system was the responsibility of the MIT group and will be discussed in addition to the polarized ^{1}H target, though only the polarized ^{1}H target provided the data presented in this thesis.

The apparatus common to both targets systems will first be discussed. A schematic of the target region is shown in Fig. 2-5. A flow of target gas is directed into a windowless tube that confines the gas atoms in a region close to the positron beam. This storage cell is an elliptical tube mounted coaxially with the HERA positron beam. It confines the target gas

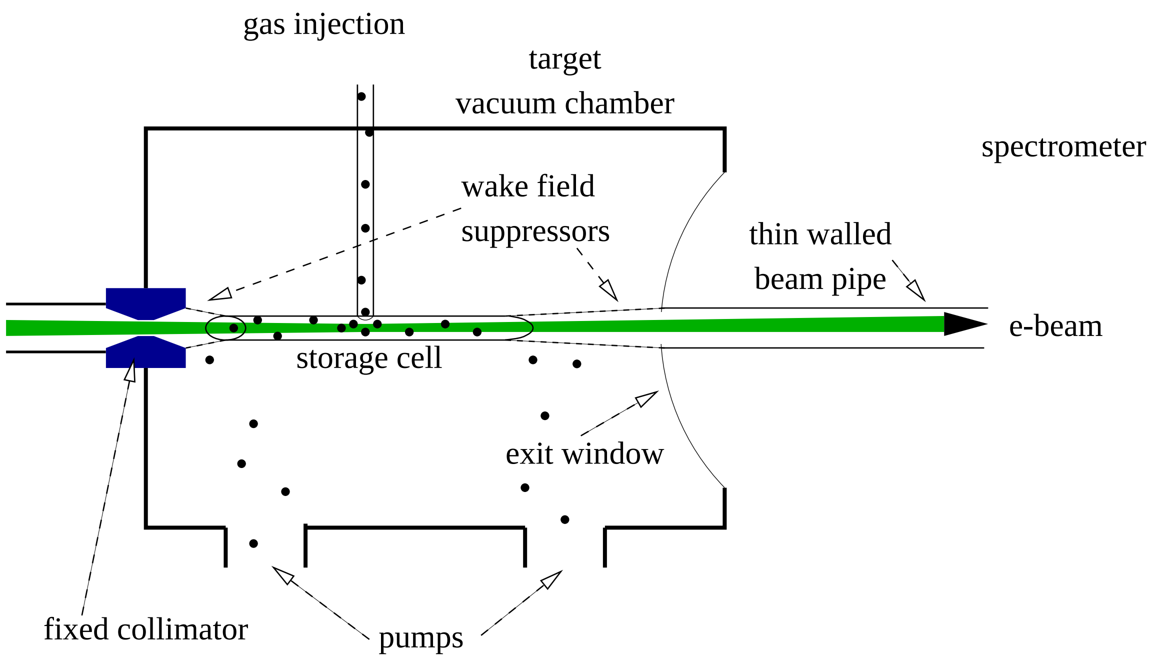

Figure 2-5: Schematic diagram of the target region.

near the high energy positron beam, increasing the target thickness by roughly two orders of magnitude compared to an atomic beam. The cell is a 29×9.8 mm^2 elliptical tube that is 400 mm long. It is made from 75 μm thick aluminum. To increase the target thickness even further, the storage cell is cooled by flowing cold helium gas through the support structure. Platinum resistance thermometers mounted on the cell support structure monitor the cell temperature. The typical operating temperature is 100 K.

The ends of the cell are windowless so that the positron beam can pass freely though the cell. To prevent contamination of the positron beam vacuum, a powerful differential pumping system with a total pumping speed of about 9000 L/s is used in the region surrounding the cell to remove the target gas. The pressure in the target region when the ABS is in operation is typically 1.5×10^{-7} mbar and this is reduced to about 5×10^{-9} mbar outside the target region.

The transition from the cell to the beam pipe was made smooth to avoid the generation of wake fields that could cause heating and increase the emittance of the beam. This was accomplished using thin perforated tubes called "wake-field suppressors".

To protect from synchrotron radiation created upstream of the HERMES area, a system of two collimators, C1 and C2, were installed upstream of the target. C2 is shown in the schematic diagram in Fig. 2-5. C1 is located 2 m upstream of the target and protects C2 from direct radiation. C1 consists of two movable collimators in the horizontal and vertical directions, separated by a half a meter. These collimators are opened during injection and are returned to a narrower setting before applying high voltage to the elements of the spectrometer. C2 has a fixed aperture and is located directly in front of the storage cell. It also protects the cell from direct radiation during injection.

Particles that scatter from the target gas and into the spectrometer exit the target chamber through a 0.3 mm stainless steel foil. The beam pipe downstream of the target chamber is also made of thin stainless steel. These thin foils present a small probability for radiation to the particles as they enter the spectrometer, thus minimizing electromagnetic showering.

2.2.1 The HERMES Polarized ^{1}H Target

The polarized atomic hydrogen target is described in detail in Refs. [76, 77]. This section is based largely on Ref. [77]. A schematic diagram of the target is shown in Fig. 2-6. A beam of polarized hydrogen atoms is formed using the atomic beam source (ABS). The injected target gas is analyzed using a target gas analyzer (TGA) and a Breit-Rabi Polarimeter (BRP). The TGA measures the fraction of the hydrogen that is in atomic form and the BRP measures the polarization of the atomic hydrogen. Significant Monte Carlo and background corrections are possible to the atomic fraction measured by the TGA, as it is hard to distinguish where the recombination occurred and thus find the true atomic fraction in the target cell.

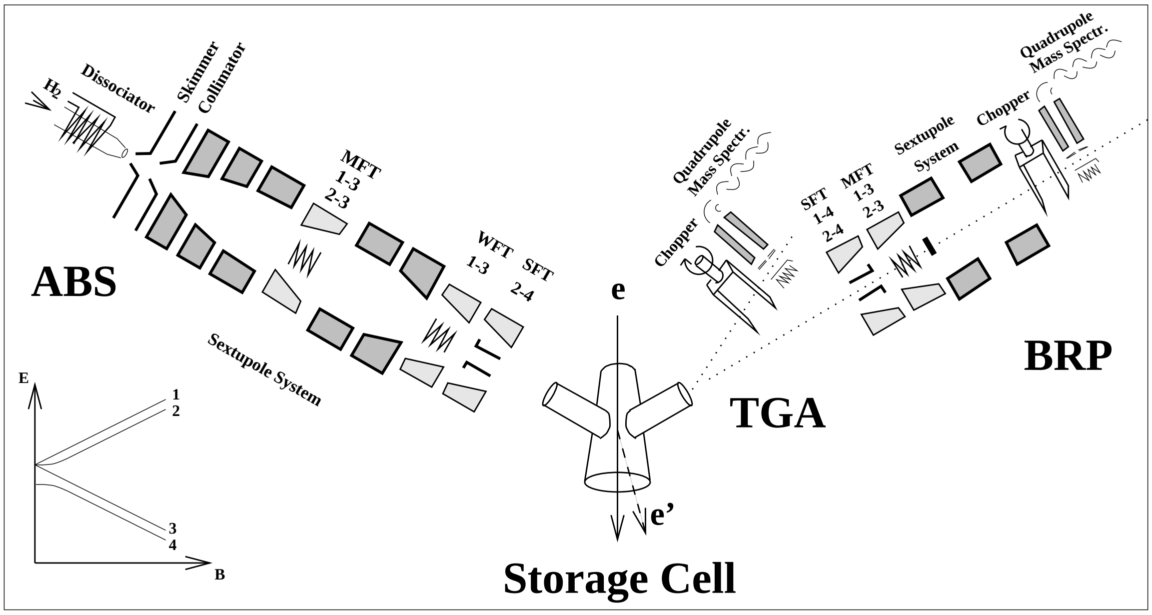

Figure 2-6: Schematic diagram of the HERMES polarized ^{1}H target. Inset: energy level diagram for atomic hydrogen.

Each part of the ^{1}H target system will now be described in greater detail, proceeding from left to right in Fig. 2-6.

The beam originates in the RF dissociator of the ABS, where injected molecular hydrogen from a gas bottle is converted to atomic form. The RF dissociator simply provides a strong RF field which completely dissociates the hydrogen molecules. The atoms have their electrons polarized by Stern-Gerlach separation in a system of five sextuple magnets. The electron polarization of the atomic beam after the magnet system is transferred to the protons by means of two adiabatic RF transitions. The weak field transition (WFT 1-3) after the magnet system provides negative proton polarization. The strong field transition (SFT 2-4) provides a positive proton polarization. By switching off the transitions, the electron polarized state created by the sextpoles is injected. Using the medium field transition (MFT 1-3/2-3), located after the third sextuple, either hyperfine state $|1\rangle$ or $|2\rangle$ can be transferred into state $|3\rangle$ which can then be deflected away by the remaining two sextpoles. Using this transition in combination with the WFT 1-3 and SFT 2-4 transitions allows the injection of each of the four possible states separately. The seven different combinations possible are cataloged in Table 2.2.1. A small diagram showing the energy level splitting of the four atomic hydrogen states may be found in the inset of Fig. 2-6. To minimize

ABS transitions on	injected states	S_z^e	S_z^p
none	$\|1\rangle$ or $\|2\rangle$	$+1$	0
WFT 1-3	$\|2\rangle$ or $\|3\rangle$	0	-1
SFT 2-4	$\|1\rangle$ or $\|4\rangle$	0	$+1$
MFT 2-3, SFT 2-4	$\|1\rangle$	$+1$	$+1$
MFT 1-3, WFT 1-3	$\|2\rangle$	$+1$	-1
MFT 2-3, WFT 1-4	$\|3\rangle$	-1	-1
MFT 1-3, SFT 2-4	$\|4\rangle$	-1	$+1$

Table 2.1: Injection modes of the ABS [78].

false asymmetries from systematic drifts in the detector, the target polarization is reversed frequently (every 30 seconds).

The polarized atomic hydrogen is injected into the cell through a 100 mm long, 10 mm diameter entry tube and then diffuses out of the ends of the storage cell. The cell is located in a vacuum chamber surrounded by a super conducting magnet which provides a quantization axis for the proton and electron spins. The field is produced by four coils resulting a non-uniformity of $\frac{\Delta B}{B} = \pm 1.5\%$ along the cell axis at the working point of $B = 355$ mT. To economize on cold helium usage, the superconducting target magnet uses the same helium supply as the target cell. The target gas is sampled in the middle of the cell through a 100 mm long 5mm diameter sample tube. A 10 mm diameter 120 mm long extension tube is connected to the sample tube to direct gas into the TGA and BRP.

The TGA measures the relative fluxes of atomic and molecular hydrogen coming through the sample tube. The TGA is mounted off axis by 7° so that is doesn't interfere with the gas entering the BRP. Two baffles collimate the beam entering the TGA. A quadrupole mass spectrometer is used to analyze the resulting beam. A chopper allows the subtraction of background due to residual gas.

The BRP uses a similar RF and sextuple magnet system as the ABS to analyze the atomic polarization of the atoms from the sample tube. The BRP also has elements similar to the TGA to collimate and analyze the beam using a chopper and a quadrupole mass spectrometer. Switching between the four possible states of the two RF transitions and measuring the ^{1}H rate using the mass spectrometer gives a determination of the occupation probabilities for the four hyperfine states. From the occupation probabilities and a knowledge of the guide field, the polarization of the atomic hydrogen can be calculated. To calibrate the BRP, the transition efficiencies of the RF transitions and transmission probabilities of the sextuple system must be measured. The extraction of these factors can be done by switching the ABS and BRP transitions through all possible combinations.

The target polarization is determined using the formula [78]:

$$P_T = \alpha_0[\alpha_r + (1-\alpha_r)\beta]P_T^{\mathrm{atom}} \tag{2.6}$$

where α_0 is the initial atomic fraction, α_r is the fraction of atoms surviving recombination and β is the polarization of the recombined molecules relative to the polarization of the atomic hydrogen P_T^{atom}. The quantity β is essentially unknown and the lack of knowledge is assigned to a portion of the systematic error on the target polarization. To determine the true α_r and P_T^{atom} in the target cell from the measurements of these quantities from in the TGA and BRP, α_r^{TGA} and $P_{\mathrm{T}}^{\mathrm{BRP}}$, respectively, sampling corrections c_α and c_P must be introduced:

$$\alpha_r = c_\alpha \alpha_r^{\mathrm{TGA}}, \tag{2.7}$$

$$P_T^{\mathrm{atom}} = c_P P_T^{\mathrm{BRP}}. \tag{2.8}$$

The sampling corrections account for effects which might change the measured values due to the fact that the atoms must travel some distance before reaching the TGA and BRP. Possible resulting effects on the measurement of α_r by the TGA are recombination within the gas and on the cell and sample tube walls. Possible effects on the measurement of the atomic polarization are spin exchange in collisions within the gas and spin changes in wall collisions. A Monte Carlo was developed to estimate these corrections and was used to assign a systematic error.

Using these corrections, the injected proton polarization was determined to be typically 95.5%. The average polarization loss was determined to within 2.5% from spin exchange collisions and 1% from wall collisions. The final result was $P_T^{\mathrm{atom}} = 0.92 \pm 0.03$ (syst.). The value for c_α is easier to constrain when α_r^{TGA} is close to unity, as was the case in 1997, resulting in $\alpha_r = 0.93 \pm 0.04$. The range for β was taken to be $0.2 \leq \beta \leq 1.0$, constrained by HERMES estimates when operating the target at low α_r [76, 79]. The result for the target polarization was 0.88 ± 0.04 (syst.) in 1997. For the 1996 data taking, the value for α_r^{TGA} was not as close to 1, resulting in larger Monte Carlo uncertainties. The value for the target polarization in 1996 was roughly 0.85 ± 0.12 (syst.). The error in the 1996 target polarization can be reduced by renormalizing the result to the 1997 results using the deep-inelastic asymmetry.

2.2.2 The Unpolarized Gas Feed System

The Unpolarized Gas Feed System (UGFS) is used to supply a variety of pure unpolarized gaseous targets for the HERMES experiment. Several unpolarized measurements carried out by the experiment were described briefly in section 2.2. The UGFS is also used for the calibration of the polarized target. This includes determinations of the unpolarized flows needed to fully determine α_0 for the calculation of the target polarization, such as background pressure in the target chamber due to finite pumping capacity of the HERMES pump-stands in the target region. The UGFS is also used to check the relative calibrations of the ion gauges in the pump-stands in the target region, upon which many of the BRP and TGA calibration parameters depend.

A schematic of the UGFS is shown in Fig. 2-7. The various valves are used to control the direction of flow of the gas, while the pressure gauges and transducers monitor the pressure

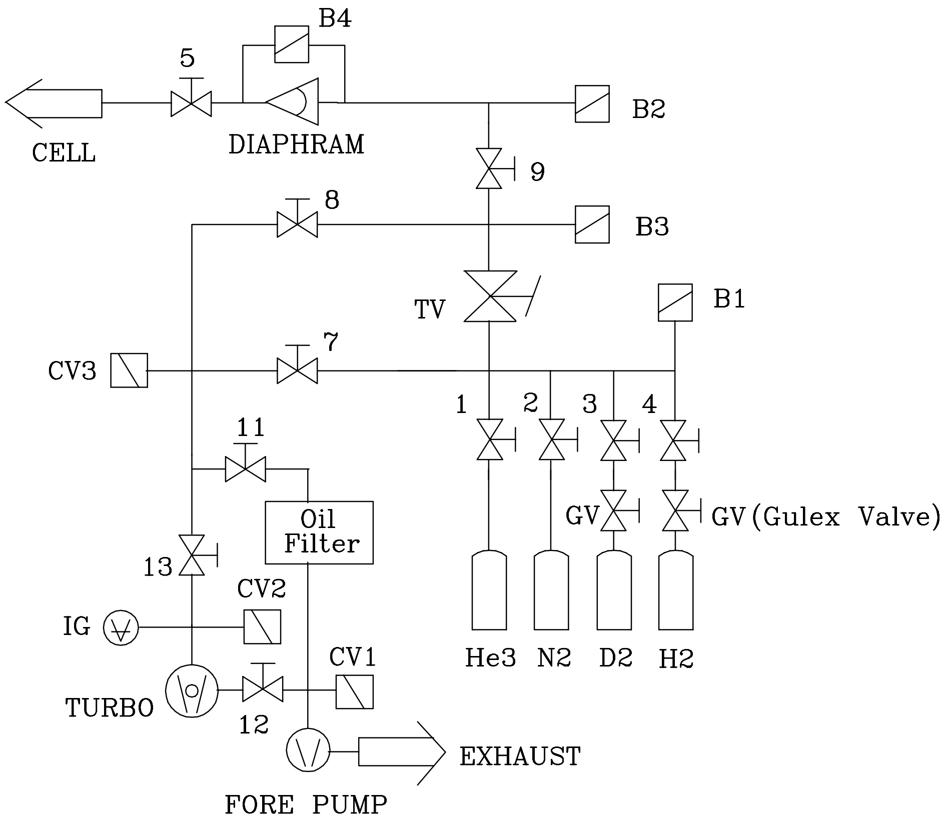

Figure 2-7: Schematic diagram of unpolarized gas feed system as configured for 96 running. Displayed in the figure are the locations of solenoid valves (numbered 1 through 13), Gulex valves (labeled GV), a thermo-valve (TV), a diaphragm, Convectron pressure gauges (labeled CV1 through CV3), Baratron pressure transducers (labeled B1 through B4), an ion gauge (IG), and bottles filled with different gases. Also displayed are possible ways for gases to leave the system (through the target chamber, target cell, or exhaust), and the turbo and fore pumps for the system.

of the particular gas as it is flowing through the system. The turbo and fore pumps are used to clear gas out of the system quickly, e.g. when changing gas types.

In normal operation, valves 5 and 9 and the bottle valve for the desired gas are left open so that gas flows from the bottle through the thermo-valve and diaphragm into the target cell. Valve 6 is used to flow into the target chamber, simulating the background conditions when the polarized ^{1}H target is in operation. This provides a calibration of part of α_0 for the polarized ^{1}H target [76].

The important feature of the system is the ability of the diaphragm and thermo-valve to regulate the pressures in the system in order to supply a constant density of the order 10^{15} nucleons/cm^2 to the target cell. Calibrating the diaphragm conductance as a function of the pressures measured by B2 and B4 then allows for an absolute determination of the flow rate. The flow rate has a known dependence on the type of gas that is flowing, so the calibration was performed for only one gas. Calculating the conductance of the target cell then allows for a determination of the target density. The target density calculated using this method has been calibrated to within 20% A. The uncertainty is the uncertain determination of the diaphragm conductance and the cell conductance.

2.3 The HERMES spectrometer

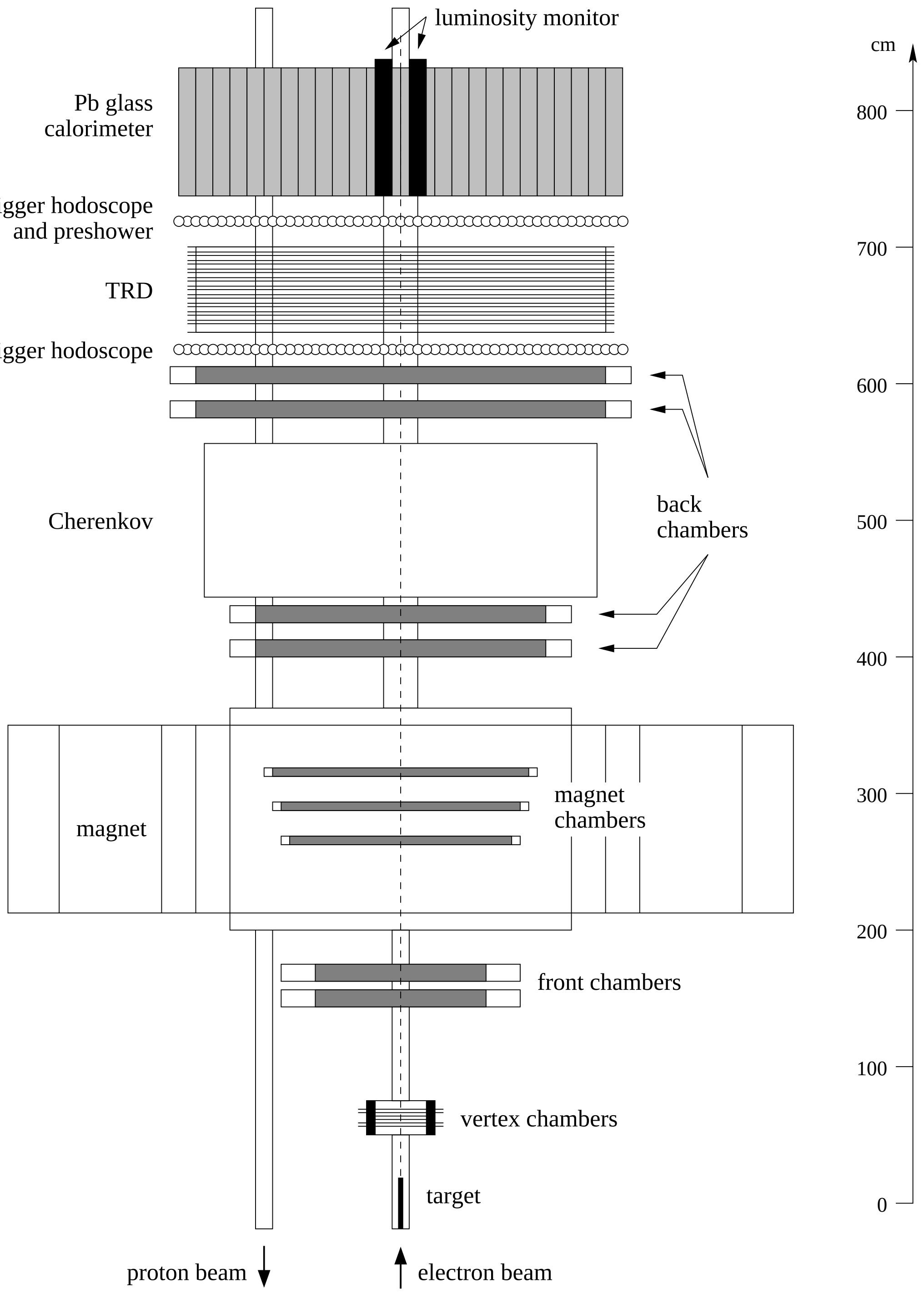

Figure 2-8: The HERMES spectrometer (top view).

The collimators and the storage cell had to be positioned at the beam waist. Since the halls were built to accommodate collider experiments, the detector was foreseen to be heavily asymmetric, and of course biased toward the forward region with respect to the proton ring. Hence, the HERA halls were not built symmetrically around the beam waist, allowing only 8.5 meters for the installation of the spectrometer.

The HERMES spectrometer was built on a movable platform. This was done for several reasons. Firstly, it allowed the spectrometer to be assembled outside the shielding in the hall during the machine operation. This also meant that major damage to the spectrometer could be repaired after installation of a replacement beam pipe, allowing the machine operation to resume while the repairs are made. Secondly, it allowed for a rapid removal of the experiment in case the HERA TRAM needed to be inserted. The TRAM is a versatile transport and installation vehicle designed specifically for the HERA tunnel. In case of a major failure in the accelerator, HERMES must remove its spectrometer within 24 hours to allow the TRAM to access the tunnel.

The combination of fixed target and high energy beam means that the angular distribution of the scattered particles is strongly peaked in the forward direction. To be able to study a large kinematic region the spectrometer was designed with a large angular acceptance. Especially the minimal scattering angle is important since it determines the smallest value of x that the experiment can access. It was limited by the fast increase in the synchrotron radiation background at small angles. The minimal vertical angle was 40 mrad, the maximum 140. The horizontal acceptance is ± 170 mrad.

The background for the experiment consists mainly of synchrotron radiation, scattering of the beam halo from the collimator system and protons lost in the proton ring. The first two sources of background can be minimized by a good beam tune. The proton background is out of time with the electron bunches and can be eliminated by a simple trigger gate. Only "side-bunches" of protons can therefore cause backgrounds in the spectrometer. A veto detector was set up to monitor this background.

2.3.1 The spectrometer magnet

As can be seen in figure 2-8, the core of the HERMES spectrometer is a large conventional spectrometer magnet. The dipole field has an integrated strength of 1.5 T-m, but it was operated at only 1.3 T-m for the experiment. The magnet frame is an H-type with the coils internal to the magnet steel. The variation in the integrated field strength for particles within the geometric acceptance is less than 10%. The power consumption of the magnet is 729 kW at the design strength.

The influence of this field on the beams would be unacceptable, so an iron septum plate was mounted in the beam plane. Both beam pipes pass through this plate. To further reduce both dipole and higher order fields several coils were built into the septum plate. Careful field mapping alternated with adjustments in coil current distribution was needed to cancel the stray field effects. To reduce the influence of the stray fields on the spectrometer performance field clamps were mounted on the sides of the magnet. This reduced the stray fields in the tracking detectors from 0.32 T to 0.1 T. In the target region the fields were still on the order of 20 Gauss with a gradient of about 220 mGauss/mm. This was enough to warrant serious studies for the helium target, resulting in the addition of a compensating coil to the target assembly to reduce the depolarizing gradient.

2.3.2 The tracking detectors

The tracking detectors consist of several sets of chambers. The distribution of these chambers can be seen in figure 2-9. For tracking purposes we divide the detector into three regions with respect to the spectrometer magnet: forward, back and magnet. The forward region is covered by the vertex chambers (VC) and forward chambers (FC). This region determines the angle of the track and its scattering vertex. The back region is covered by two sets of back chambers (BC). Together with the track in the forward region this determines the angle of deflection of the particle in the spectrometer magnet and hence its momentum. It is of course crucial to match both tracks up correctly. For this reason additional chambers were inserted inside the magnet. These magnet chambers (MC) can also be used to increase the acceptance of the detector for low energetic particles. All chambers

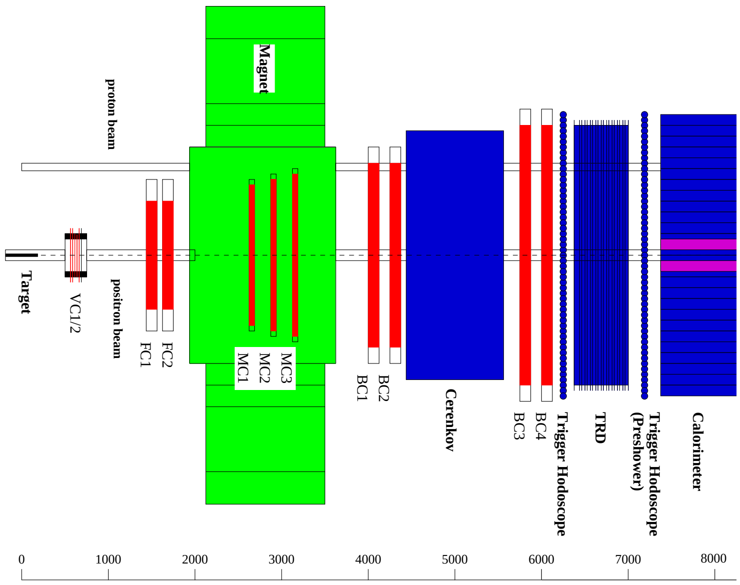

Figure 2-9: Schematic view of the tracking chambers in the HERMES detector.

measure three coordinates: u, v and x. The x-coordinate is in the plane of the beams, so the x-detection wires need to be vertical. The u and v coordinates are measured with wires that are mounted at an angle of 30° with respect to the vertical. The use of horizontal wires to measure the y-component of the hits directly would have been preferable, but it was not pursued for practical reasons. The fact that all chambers measure the same coordinates makes it possible to reconstruct the tracks in all three projections before combining them. This allows for a more robust and faster reconstruction algorithm. A reconstructed event highlighting the use of all detectors is shown in figure 2-10. This event is not very typical since it is a high multiplicity event. The average multiplicity is only 1.3 tracks per event. In figure **??** the transverse and longitudinal coordinates of the reconstructed vertex are shown. It is clear from those plots that no scattering from the cell walls or the collimators interferes with the measurement.

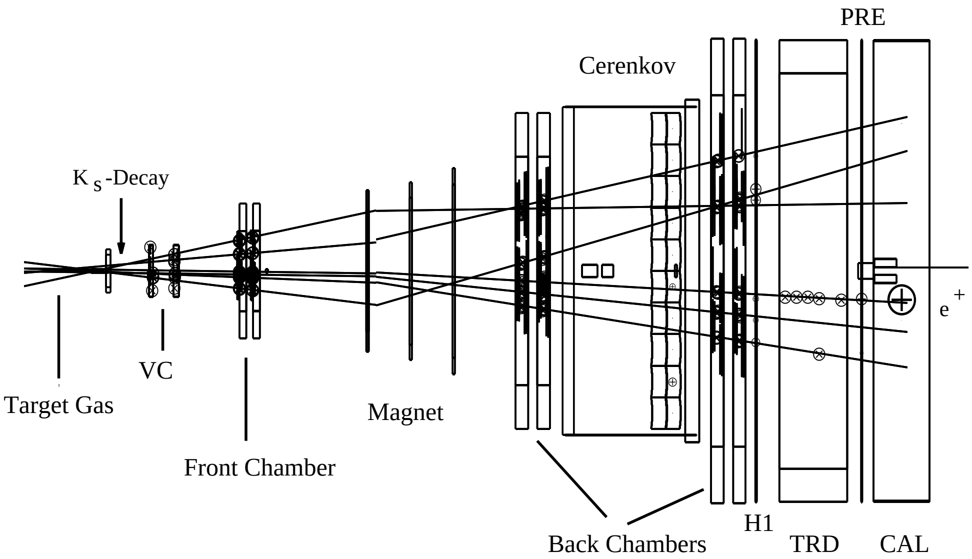

Figure 2-10: Reconstructed high multiplicity event containing a decaying K_s.

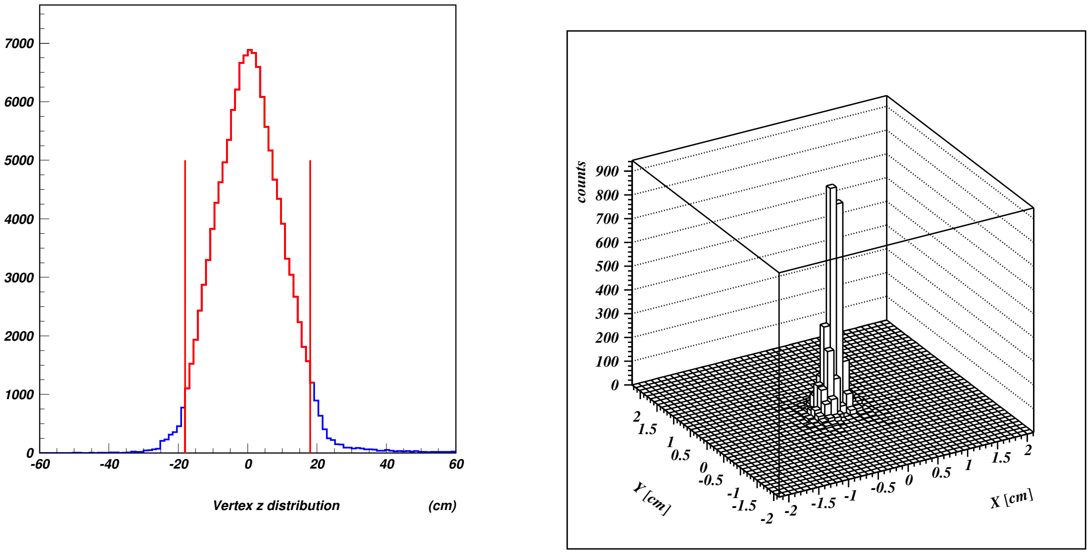

Figure 2-11: The distributions of the reconstructed vertices.

2.3.2.1 The vertex chambers

The vertex chambers have to sustain very large background rates and provide enough precision to determine the vertices accurately. HERMES used micro-strip gas chambers for this purpose. Each chamber consists of two modules, with each one plane for the u-, v- and x-direction. Each plane consists of a planar cathode foil and an anode plane. The cathode foil provides a 5 kV/cm drift field over the 3 mm volume between the foil and the substrate. The gas in this volume is a mixture of 60% DME and 40% CO_2. The anode plane consists of a 300 μm thick glass substrate covered with 1 μm thick aluminum anode and cathode strips. The anode strips are 7 μm wide and 193 μm apart, giving a cell size of 0.2 mm. The anodes are interlaced with 90 μm wide cathode strips.

This design has about three times the gain level of silicon detectors of the same thickness. A spatial resolution of 45 μm per module was obtained, translating into a 200 μrad angular resolution for the chamber. This is comparable to the uncertainty due to multiple scattering in the exit window.

During the 1995 data taking the vertex chambers did not function properly. Sustained oscillations in the electronics reduced their efficiency to a level at which they could not be used for standard tracking. Using the VC's for tracking we did construct a smaller data set with which other tracking methods could be checked for systematic biases. The read-out electronics were redesigned and new chips were installed for the 1996 data taking period.

2.3.2.2 The forward chambers

The second set of tracking chambers in the forward region is a drift chamber with a conventional horizontal drift configuration. Each plane is a layer of drift cells consisting of a wire plane of alternating anode and cathode wires between a pair of cathode foils. Each chamber consists of 6 planes, two for each coordinate u, v and x. The second plane for each coordinate is staggered with respect to the first to resolve left-right ambiguities. The gas mixture consists of 90% Argon, 5% CF_4 and 5% CO_2.

The drift cell size of only 7 mm was chosen to reduce the influence of the background. The resolution was expected to be 150 μm, but pick-up from the target RF discharge reduced the observed resolution to $\sim$400 μm.

2.3.2.3 The back chambers

The back region tracking is done with two sets of drift chambers BC1/2 and BC3/4, positioned respectively at 3.95 and 5.70 meter downstream of the interaction point. They use the same horizontal drift configuration as the forward chambers but with a cell size of 15 mm. The gas mixture was common to both chambers, simplifying the operation of the tracking chambers. Despite their larger cell size a resolution of 150 μm was expected. This is due to the high drift velocity in the $Ar/CF_4/CO_2$ gas. Indeed, even in the larger cell the maximum drift time is 150 nsec, which compares favorably with the HERA bunch crossing time of 96 nsec. This means very few mixing of hits from different bunches will occur. However, the realistic resolution obtained during the 1995 data run was $\sim$400 μm.

Each chamber consists of two modules containing 6 planes. This means that BC1/2 and BC3/4 each contains 24 planes, 12 above and 12 below the beam plane, for a total of 48 planes in each detector half.

2.3.2.4 The magnet chambers

The magnet chambers were added to make the matching of front and back tracks easier in case of high multiplicity events. The presence of the strong magnetic field and the low requirement on the resolution directed the choice of the proportional chamber technology for these chambers. The anode wires are separated by 2 mm, resulting in a resolution of 577 μm. Three chambers are present, each containing three planes (u, v and x). The gas used is a mixture of 65% Argon, 5% CF_4 and 30% CO_2.

An unexpected sensitivity of the backplane electronics to the magnetic field resulted in serious damage to the readout electronics early in the year. The limited accessibility of the chambers (inside the magnet) made it impractical to perform repairs. For the 1995 data the magnet chambers were therefore not used, except for specific studies of small-momentum particles, in particular for rare decays.

2.3.3 The particle identification detectors

For the study of inclusive reactions a good hadron-positron separation is necessary. The semi-inclusive processes require further identification of the hadrons. To accomplish these tasks HERMES uses the combination of several particle identification detectors. All are located in the back region of the detector.

2.3.3.1 The calorimeter

The calorimeter is built in two halves (like every other HERMES detector), with each half containing 42×10 radiation resistant lead glass (F101) blocks. Each block has a surface of 9×9 cm^2 and is 50 cm long. This corresponds to 18 radiation lengths. At the back of each block a photo multiplier tube is mounted to measure the energy deposited in the form of electromagnetic radiation in the block. The violent impact of the scattered positron causes electromagnetic showers. The energy is usually deposited within a cluster of 3×3 adjoining blocks. The spatial resolution of the calorimeter can then be improved over the size of the blocks by analyzing the shape of the energy cluster. The resolution that can be achieved in this manner is about 0.5 cm.

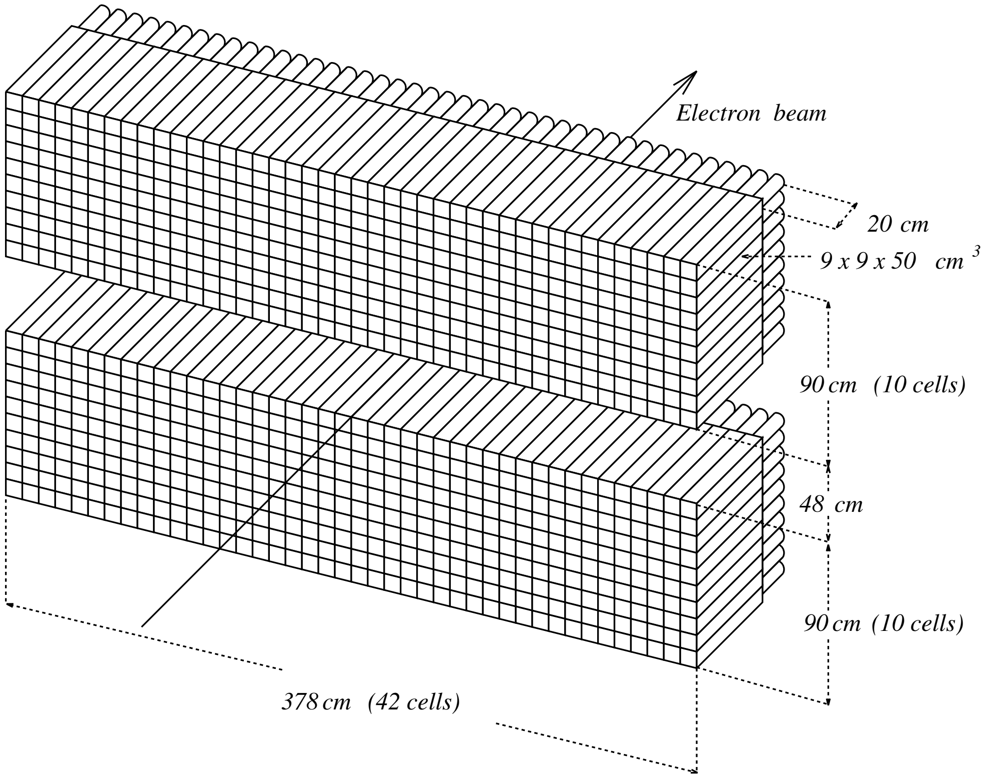

Figure 2-12: Isometric view of the HERMES calorimeter.

Pions and other hadrons cause hadronic showers. These particles will usually travel further in the blocks while just losing energy by ionization, since the nuclear reaction length is much larger than the radiation length. The reaction is also much more violent, and the energy is spread wider, covering more calorimeter blocks. A simple comparison of the energy deposited in the calorimeter with the energy determined by track bending in the magnet provides a way to distinguish hadrons and positrons.

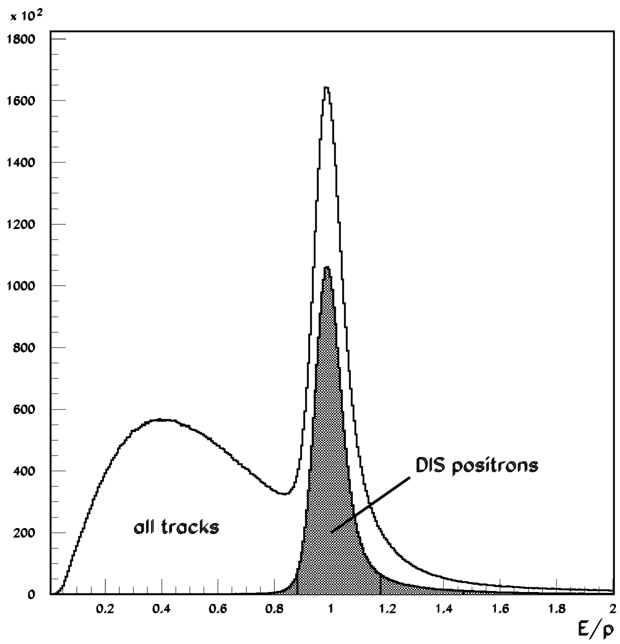

Figure 2-13: Ratio of energy deposited in the calorimeter to momentum determined by the magnet bending radius.

The rejection factor is limited by the presence of the charge exchange reaction that transforms the charged pions into neutral pions that decay into two photons, leading to two electromagnetic showers that cannot be distinguished from a normal positron shower. The charge exchange cross section makes up about 1% of the total inelastic cross section for πN reactions. The rejection factor (disregarding the relative fluxes) for pions is therefore about 100:1 for energies in the 1-10 GeV range. As shown in figure 2-13 there is a fairly large number of events with $E/p < 1$. This is due to pre-magnet bremmstrahlung and attenuation effects in the lead glass. The former effect is easy to understand: the energy lost in the bremmstrahlung is not measured for p, but the bremmstrahlung photon is very likely to end up in the positron impact cluster and will hence be counted towards E. The latter effect is somewhat more subtle and is caused by the preponderance of electromagnetic showers that are started in the preshower. These showers will develop at the start of the calorimeter block. Positrons that do not shower in the preshower will start showering later in the calorimeter block, which means closer to the phototubes. Hence the light from these showers is less attenuated, and as long as all the energy is deposited in the calorimeter, the signal will be higher. The calorimeter is calibrated to give the right average answer, and is therefore biased towards the showers that start in the preshower.

To reduce the possibility of radiation damage, the calorimeter is moved away from the beam pipe during beam injection and ramp-up as well as beam dumps. It is moved in when the stored beam is stable. To continuously monitor the radiation damage as well as other fluctuations affecting the gain of the calorimeter blocks an extensive gain monitoring system was developed and installed. The energy resolution of the calorimeter is energy dependent:

$$\frac{\sigma(E)}{E} = 1.47\% + \frac{5.14\%}{\sqrt{E/GeV}}. \tag{2.9}$$

2.3.3.2 The preshower detector

The preshower detector consists of an 11 mm thick lead sheet followed by an array of 42 plastic scintillator paddles identical to the H1 hodoscope (figure 2-15). Each paddle covers one vertical column of lead glass blocks in the calorimeter. The lead sheet corresponds to 2 radiation lengths, but only 6.4% of a nuclear interaction length. This will increase the difference in the hadronic and electromagnetic showers, as explained in section 2.3.3.1 and hence improve the hadron-positron differentiation in the detector.

The signal from a hadron passing through the preshower is typically close to that of a minimum ionizing particle. On the other hand, positrons usually start showering, and the energy deposited is much larger. Increasing the thresholds for preshower "hits" would increase the rejection factor of the detector. However, in the test beam at CERN it was found that this would induce a large instability due to gain shifts. The thresholds were therefore set below the minimum ionizing peak.

The preshower-calorimeter combination improves the rejection factor of the calorimeter alone by a factor of 50 for an electron efficiency of 95% per block.

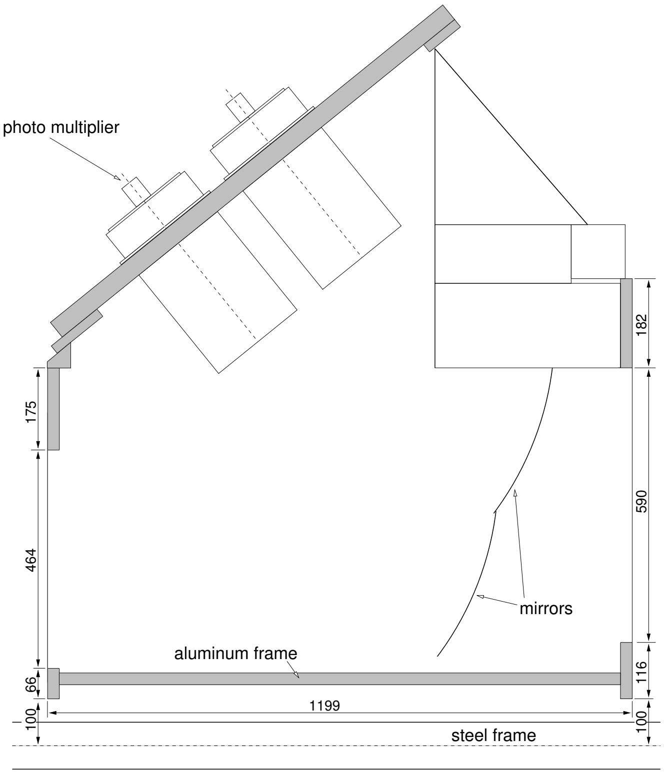

Figure 2-14: Sideview of the HERMES Čerenkov detector.

2.3.3.3 The Čerenkov detector

The straightforward separation in β for hadrons from positrons is used in the Čerenkov detector. This detector is a threshold counter, relying on the choice of the radiator gas to determine the threshold at which a particle will radiate:

$$\beta_{threshold} = \frac{1}{n_{radiator}} \tag{2.10}$$

where $n_{radiator}$ is the index of refraction. The choice of gas determines the window in which the detector will provide particle identification. For 1995 the radiator was nitrogen gas, which results in a pion threshold around 5.5 GeV, a kaon threshold of 19 GeV and a proton threshold of 38 GeV. The pions can be identified cleanly for energies between 5.5 and 19 GeV by the fact that they are the only hadrons radiating at that energy.

The Čerenkov detector consists of a gas radiator and a set of 20 mirrors and PMT's to detect the radiated photons. The total thickness of the detector is only 3.5% of a radiation length, making it possible to insert the detector between the two back region tracking chambers without compromising the momentum measurement.

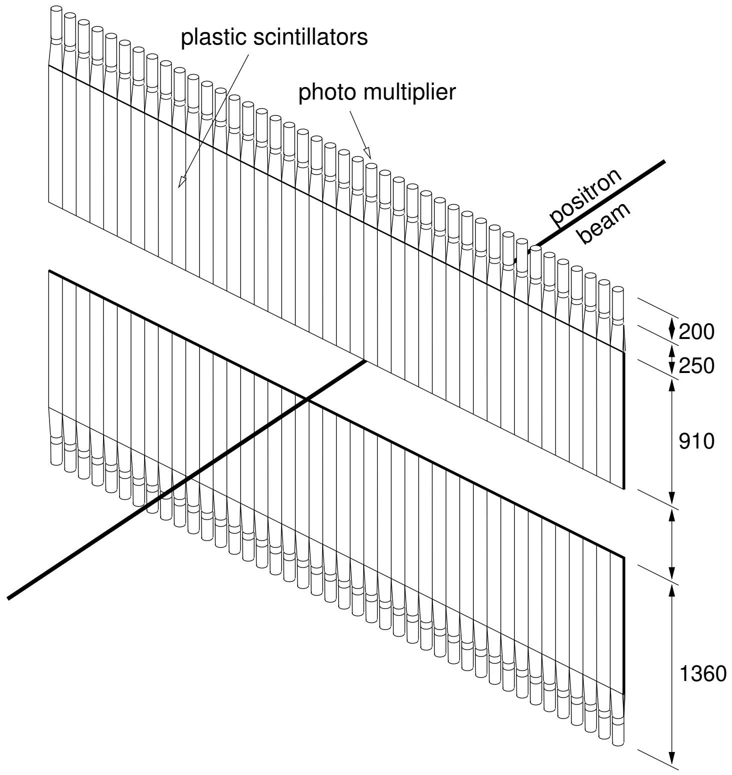

Figure 2-15: Isometric view of the HERMES hodoscope.

2.3.3.4 The hodoscope H1

The hodoscope consists of 42 plastic scintillator paddles with a size of 9.3 × 91 × 1 cm^3, each matching a vertical column of calorimeter blocks. No acceptance holes are present since the paddles overlap by 1.5 mm. The H1 hodoscope's main function is in the first-level trigger, but it is also used for low-energy time-of-flight particle identification. As a part of the first-level trigger its short radiation length (2.3%) provides a photon rejection factor of 50 to 1. This is useful to remove triggers by high energy photons (for example coming from π_0 decay). As a time-of-flight particle identification detector it can be used for energies up to 2 GeV.

2.3.3.5 The transition radiation detector

A lesser known relative of the Čerenkov radiation, transition radiation (TR) is generated at the boundary between two media with different refractive indices. The easiest way to think of TR is however as a phenomenon complementary to bremmstrahlung. Bremmstrahlung is the emission of photons by a particle of rapidly varying velocity in a medium of constant refractive index. TR is the emission of photons by a particle of constant velocity going through a medium of rapidly varying refractive index. There are several treatises describing transition radiation in detail, such as references [80] and [81]. The crucial step in creating a working detector is to make the particles go through many transitions. For the HERMES TRD the radiator consists of loosely packed propylene fibers with diameters between 17 and 20 μm. Although the ideal radiators are thin foils, the fibers are much easier to manage in the mechanical construction of the detector. Since the performance of the fibers is fairly close to that of the foils the mechanical design considerations were allowed to prevail.

There are 6 consecutive modules of 6.5 cm thick radiator followed by an X-ray detector consisting of a planar proportional wire chamber with 0.5 cm wide cells. The gas in the X-ray detector is a mixture of xenon (90%) and methane (10%). Since the object is the detection of several KeV X-rays, the high Z noble gases xenon and krypton are the natural candidates for the wire chamber gas. The decision to use xenon was based on the superior total absorption of X-rays for this gas. Indeed, krypton has a smaller absorption length for energies over 10 KeV, but the secondary X-rays it emits can escape fairly easily (mainly the K shell lines). The secondaries emitted after capture by xenon are easily absorbed (absorption is 80% for the L lines within 1 cm) and further converted. The methane is added as a quench-gas to allow larger gains without causing continuous discharges in the proportional chamber. It is important to keep oxygen out of the chambers since it would severely impact the gains. Since it is very hard to guarantee a tight closure for a chamber this size, the wire chambers were protected by flush gaps on either side. Nitrogen was circulated through these gaps to eliminate the chance that oxygen would find its way into the chamber.

In each module the hadrons will deposit energy of the usual ionization type, while positrons will produce 1-2 TR photons. The energy deposited is about 15 KeV for hadrons, with a peak at 12 KeV, and about 35 KeV for positrons. The six modules are combined in a "truncated mean", which is a mean of the six responses after removing the largest response. This significantly reduces the tail in the distributions, enhancing the separation between the hadron and positrons peaks. The final performance figure is the pion rejection factor. This figure will change with the energy of the particles because of saturation effects in the TRD modules. The pion rejection factor for 90% positron efficiency is about 50 at low momentum and rises to about 200 at high momentum. A significant improvement in the rejection factor can be achieved by a full probability analysis of the 6 module responses. A preliminary analysis indicates the pion rejection factor could exceed 1400.

2.3.4 The luminosity monitor

To monitor the luminosity a set of two small calorimeters was installed close to the beam pipe at a distance of 7.2 meters behind the target. This allows the measurement of the Möller or Bhabha scattering from the target gas. This provides the density-current product. This is very important considering the rapid and large change in this quantity over the course of a fill.

To withstand the intense radiation the calorimeter blocks are $NaBi(WO_4)_2$ crystals of size $22\times22\times200$ mm^3. As is the case with the calorimeter, the luminosity monitor can be moved away from the beam for the injection and dumping of the beams. This significantly reduces the radiation dose received.

2.3.5 The trigger

The goal of the HERMES trigger is to select deep inelastic scattered events with scattered lepton energies above 3.5 GeV. Positrons with lower energy cannot fulfill the y-cut imposed to keep radiative corrections small. A multilevel trigger system was designed with this goal in mind. The first level trigger consisted of a coincidence of the trigger hodoscope H1, the preshower H2 and the calorimeter CAL. It starts the conversion for the DAQ modules and needs to make a decision within a few hundred nanoseconds. A second level trigger initiates the readout of the DAQ by the online computers. At this level the processing speed is about 100 μsec. The third level trigger controls the tape writing and has an average processing speed of 10 msec.

The first level trigger adds each column of calorimeter blocks and makes the sum of each two adjoining columns. One of those two-column sums has to be above a threshold which corresponds to an energy deposit of 3.5 GeV. This eliminates scattered positrons that would be cut by the y-cut anyway and reduces false triggers by pions. It requires a threshold signal in the preshower, suppressing the amount of false triggers by hadrons. The coincidence requirement with the H1 hodoscope then suppresses triggering by photons. The three requirements have to be fulfilled within a short time window which is defined by the time when an electron bunch passes through the target. This time window is derived from the ring-wide HERA clock. This timing requirement reduces triggering by proton background from the proton ring.

The background events that do pass the trigger tests are the following:

1. A high energy charged pion that undergoes a nuclear reaction in the calorimeter, depositing most of its energy and that had an unusually large energy deposit in the preshower.

2. A high energy photon triggers the calorimeter while at the same time a charged hadron (from the same event) triggers the hodoscope H1.

3. A shower from the proton beam coming from a satellite bunch. Satellite bunches are formed by protons leaving their RF buckets. They arrive off-time with the proton bunch signal, and within the time window for the positron beam bunch. In principle they were suppressed by a veto signal from scintillators installed behind the calorimeter.

Currently second and third level triggers are unnecessary since the DAQ can easily handle the rates.

2.4 HERMES software

The HERMES software is divided into two categories by their functions although this is not strictly applied. The first is the online software which runs experiment and takes raw data for taping. The second is the offline software which is used to make production data for analysis. The main software [82] modules in HERMES are as following:

- ADAMO: This is the core database module based on entity-relationship. The logical structure of data is formulated by using the Data Definition Language (DDL). DDLs are translated into data structures by ADAMO. Also ADAMO supports various data formats such as the Generic ADAMO File (GAF).

- DAD: By employing a client-server scheme, distributed databases are used in HERMES[83]. This module allows the central maintenance and distribution of all data and is implemented efficiently in ADAMO format.

- PINK: Together with the Tcl/Tk package, PINK allows the easy creation of Graphical User Interfaces (GUIs) for visualization of ADAMO format data.

- HMC: This is the HERMES Monte Carlo based on GEANT[84]. It consists of various physics event generators and is able to do very detailed simulations of all HERMES detectors [85].
- HDC: HDC converts the raw data in EPIO[86] format into ADAMO format.
- HRC: HRC[83] reconstructs tracks using either HMC or HDC events as input.
- ACE: ACE [74] calculates unbiased(*i.e.* absolute) efficiencies of the various tracking chambers by using tracks that are calculated by HRC.

2.4.1 Data production

Figure 2-16 shows the basic layout of the HERMES data production scheme. The raw data in EPIO format is decoded by HDC into physical quantities (energy deposition in calorimeter, drift times in the wire chambers, etc). The output of HDC is plugged into HRC to determine tracks using hit patterns of the tracking chambers and furthermore calculates PID information. ACE uses the output of HRC to calculate efficiencies of the tracking chambers. The tracking information is stored in a GAF. Also, slow-control information is partly processed by HDC and online monitoring programs. Slow control information is updated every 10 seconds, which is known as a burst.

2.4.2 HRC

The single most important part of the program modules is the HRC [83] which reconstructs the full track of a event. The tracking is separately done for forward and backward parts of the tracking detectors by using the detector hits in each of the three wire directions (x, u and v). The underlying algorithm of finding a partial track from the hits on the planes of tracking detectors is so the called tree-search [83]. Figure 2-17 shows the typical steps of a tree-search algorithm to find a partial track. Here the tree-search algorithm is demonstrated for two tracks. First, one coarse pattern with high road width which matches the detector

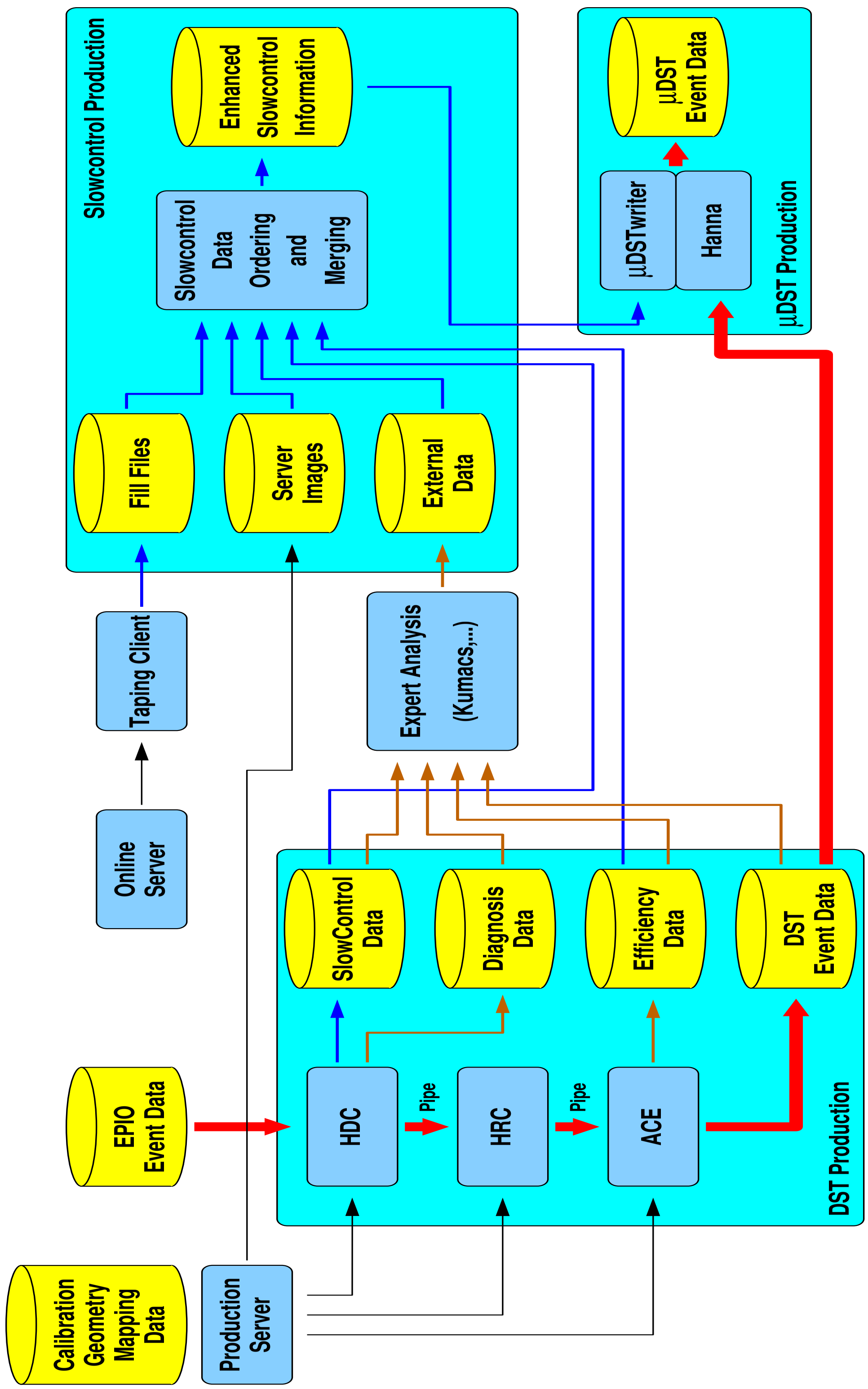

Figure 2-16: Layout of the data production in HERMES[82].

information is selected. Then the road width is recursively bisected by matching daughter patterns with higher resolution.

After a track projection was identified by the tree-search, the track parameters such as slope, offset, and uncertainties are calculated by a least squares method. Then combining the u and v information and comparing the result to find the x projection provides a 3-dimensional partial track.

The partial tracks found in the forward and backward detectors are combined to full tracks by the forced-bridged method. This method relies on the fact that the extrapolation of the back track to the center of the magnet coincides to within 1.0 cm (for low energetic particles) with the extrapolation of the front track. Considering average track multiplicity, this forced-bridge method is quite reliable. Once a matching of two partial tracks is decided the parameters of forward track(position and angle at the magnet center) is used to consult a look up table which contains the position and direction after the magnet for discrete momentum values. The precise determination of the track momentum is done by interpolation by taking into account the bending angle. The resolution of the lookup table is chosen such that the precision of the track momentum is better than $\triangle p/p = 0.5\%$. The low-momentum tracks which are deflected with a large angle by the dipole magnet do not have back track information. In such a case, the fitting of the magnet chamber hits is used to determine the momentum of the tracks.

2.4.3 ACE efficiencies

ACE calculates the efficiencies of the tracking chambers by using tracks as calculated by HRC. The efficiency [74] for a plane i is defined as

$$\eta_i = \frac{\text{number of tracks with hit in plane i}}{\text{total number of tracks in plane i}} \equiv \frac{N_h}{N_T} \tag{2.11}$$

ACE calculates two efficiencies:software efficiency and hardware efficiency. The software efficiency only consider hits which were inside the road width corresponding to the road

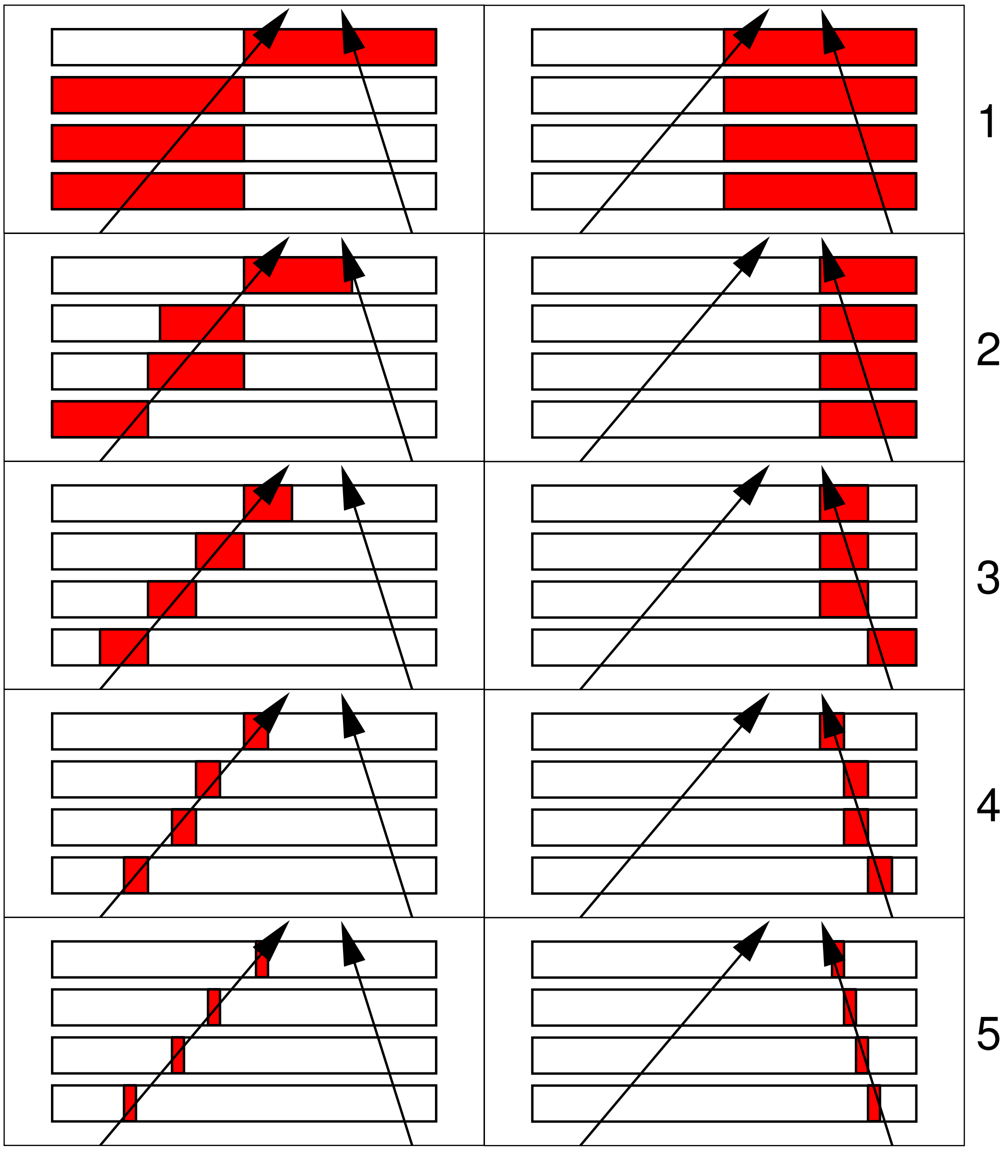

Figure 2-17: Pattern matching and Tree-Search[82, 83].

width used by HRC. The software efficiencies can be used to calculate the overall tracking efficiency. The hardware efficiency is calculated by means of looking for hits in a wider area of a particular plane. This is mainly intended for debugging purposes since a road width of several strips would introduce too much noise and background signals. The total tracking efficiency for a single full track is given by

$$\eta_{total} = \eta_{front} \cdot \eta_{back}\ cot\eta_{forced-bridge}. \tag{2.12}$$

2.5 Particle identification scheme

In order to separate the positrons from hadrons in the data, the PID information is used. Generally there are two ways of using PID responses in HERMES. The first method is by using *straight cuts*. This method utilizes each PID detector response which is shown in figure 2-18 over the relevant range of energies for both hadrons and positrons. In each of the spectra from the PID detectors, cuts separate the positrons from hadrons. The second method uses the *likelihood* technique from all detector responses. The unconditional likelihood for a detector uses the conditional probability based on the Bayes theorem[87]:

$$\mathcal{L}^e_{det} = \frac{\mathcal{P}^e_{det}}{\mathcal{P}^e_{det} + \mathcal{P}^h_{det}} \tag{2.13}$$

where $\mathcal{P}^{e/h}_{det}$ are the probabilities for positron/hadrons. Then using each likelihood from the PID detectors, the PID35 has been used in this analysis and the definition is given as

$$PID3 + PID5 = log_{10}[\frac{\mathcal{P}^e_{Cal}}{\mathcal{P}^h_{Cal}}\frac{\mathcal{P}^e_{Pre}}{\mathcal{P}^h_{Pre}}\frac{\mathcal{P}^e_{Cer}}{\mathcal{P}^h_{Cer}}\frac{\mathcal{P}^e_{TRD}}{\mathcal{P}^h_{TRD}}]. \tag{2.14}$$

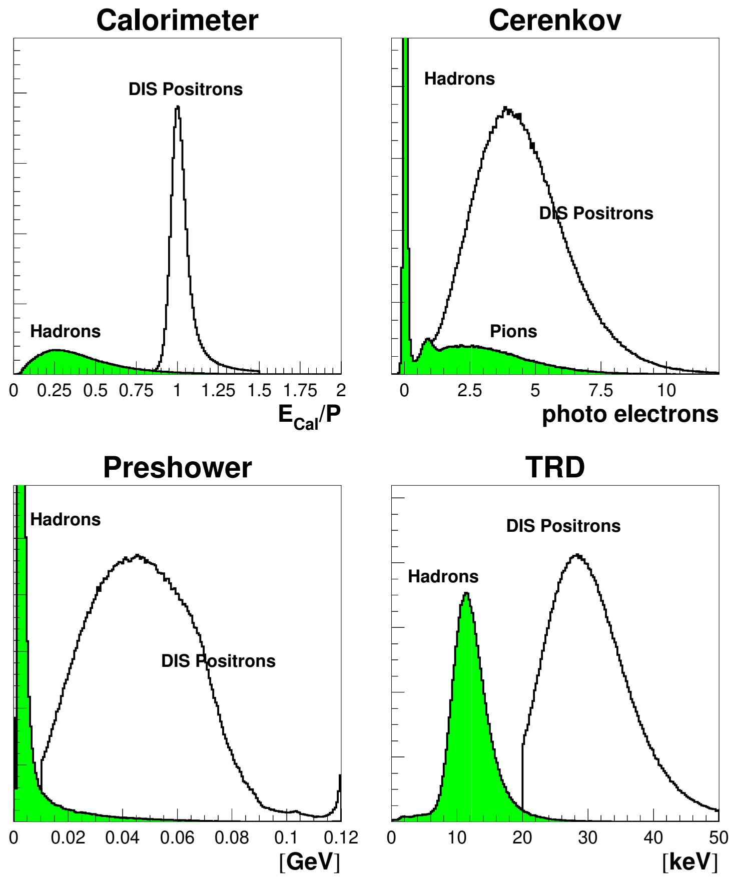

Figure 2-18: Responses of the PID detectors. The reconstructed positrons and hadrons from a Monte Carlo study of the PID detectors are shown.

Chapter 3

The Data Analysis

The HERMES experiment produces a large amount of DIS physics events in a given running period. In addition to physics data, a considerable amount of status information reflecting the conditions of different detectors during data taking is taped and stored as slow log files. Using custom written HERMES software, the data (called smDST) contain synchronized information at the event and burst level. This chapter describes the quality checks and analysis cuts to extract the unpolarized physics results.

3.1 Data quality

The data quality study for the unpolarized physics analysis is relatively simple compared to that used in the polarized physics analysis in HERMES since there is no requirement of synchronization of the spin bit. However, all of the resulting data are not good. The HERMES spectrometer consists of many different detectors and requires many levels of quality checks. Most of the information concerning detectors for data quality is incorporated into slow control events which are written to tape every 10 second. By relying on the information from slow control events, the good runs and bursts are selected. The physics event cuts for DIS are also applied at the event level.

3.1.1 Burst Selections

The burst selection was done for top and bottom detectors, separately. Using various burst level information from different components of the HERMES detector and DAQ, the good/bad burst was assigned. The main burst level quality cuts for unpolarized data analysis are as follows:

3.1.1.1 DAQ

- Reject the first and last burst in each run.
- Require Live-time: $0.8 < T_{live} < 1.0$.
- Require Burst-length: 9 sec $< \Delta t <$ 11 sec.

3.1.1.2 Tracking Efficiency

- Require front ACE plane efficiency for top and bottom: $0.8 < \epsilon_{ACE,front} < 1.0$
- Require back ACE plane efficiency for top and bottom: $0.8 < \epsilon_{ACE,back} < 1.0$
- Require front tracking efficiency for top and bottom: $0.8 < \epsilon_{front} < 1.0$
- Require back tracking efficiency for top and bottom: $0.8 < \epsilon_{back} < 1.0$
- Require total tracking efficiency for top and bottom: $0.8 < \epsilon_{total} < 1.0$

3.1.1.3 High Voltage

The high voltage(HV) information on the FC, BC, and Calorimeter was usd to determine tracking chamber data quality. Whenever there is a HV trip in FC, BC, and Calorimeter, the burst was rejected.

3.1.1.4 Others

- smDST quality: g1Quality_iExpment was required to be 1 and iTRDDQ was required to be 3 for 96 data only.
- GMS data quality:If there was information from the GMS, bursts were eliminated if there was one or more dead blocks in the bottom of the calorimeter, or at least one dead block in either the top of the calorimeter or preshower.

3.1.2 Run and fill selection

Runs were verified to be unpolarized by a check of the target log-books, hand written entries of the target type, and run summaries. These target types are checked with smDSTs, again. During the two weeks of dedicated unpolarized data taking period, total of 1239 runs (=23 fills) was taken and taped. Thus, 1085 runs (340 runs for H_1,467 for D_2, and 181 for ^3He) out of 1239 runs were used for analysis after various data quality studies. The information used for selecting runs is as follows:

- The fill information is mainly obtained from the experimental log books to verify data producing fill instead of testing detectors.
- The electronic experimental log book is widely used to decide between a good production and a test production.
- The high voltage (HV) information in the hand-written log-book has been checked.
- The normalized yields for different targets for each fill has been checked.
- The ratio of the number of good bursts to all bursts for each run is required to be greater than 65 %.

3.1.3 Kinematic and other event level cuts

Tracking was done using the forced-bridge method (see HERMES software section in Chapter 2), using only the FCs for tracking in the front region. The vertex chamber (VC) was not used in this analysis. In order to select valid DIS positrons and hadrons, the following event level cuts were applied.

- Fiducial volume cut: This cut was implemented by cutting on the iSelect bit in the smDST. An explicit cut on $|\theta_y| > 40$ mrad was also included.
- Vertex position: |Z_vx| < 18 cm and |Z_tr| < 0.75 cm.
- Positron Identification: $PID3 + PID5(PID35) > 2.0$
- Hadron Identification: $PID3 + PID5(PID35) < -2.0$
- Kinematic cuts for positrons: The highest momentum positron was required to pass the following DIS cuts: $Q^2 > 0.3$ GeV^2, $W^2 > 4$ GeV^2, $y < 0.85$. Additionally, the calorimeter cluster energy was required to be $E_{calo} > 3.5$ GeV.

For the calculation of the kinematics, the beam energy was taken as $E_{beam} = 27.57$ GeV and the mass of the proton as $m_p = 0.938272$ MeV/C^2.

3.2 Normalized yield

The normalized yield is defined as the ratio of the number of reconstructed positrons to integrated luminosity with dead time corrected and is given as:

$$Y \equiv \frac{N_{e^+}}{L\Delta t_{burst} T_{accepted}/T_{generated}} \tag{3.1}$$

where N_{e^+} is the number of reconstructed DIS positrons; L is the lumi rate; Δt_{burst} is the burst length; $T_{accepted}/T_{generated}$ is the ratio of triggers accepted to generated for live-time.

Since the luminosity monitor is measuring e^+e^- scattering rates, the normalized yield for different targets serves as a good check on the data quality. Figure 3-1 shows the normalized yields of top and bottom detector for ^{1}H , ^{2}H , and ^{3}He of unpolarized targets in 1996 data taking. This plot shows the clear distinction between different gases for top and bottom

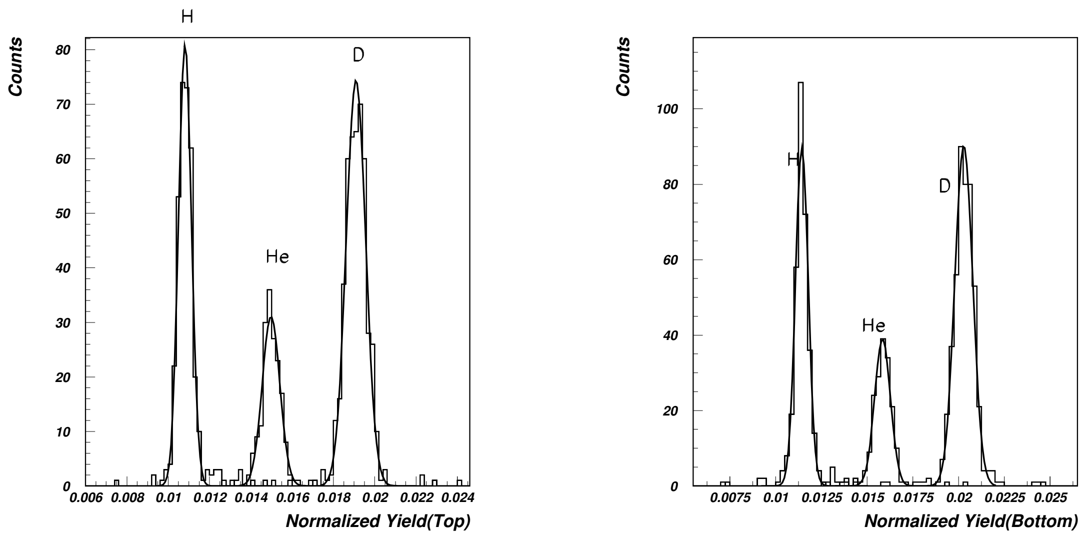

Figure 3-1: The normalized yields for top and bottom detectors.

detectors. Although eliminating some runs from the Gaussian distribution tail for each target does not alter any physics results, this analysis applied a 1-σ cut for each target as mentioned in 3.1.2.

3.2.1 Normalized yields in fills

Although experimental conditions are usually kept constant throughout the data taking, there is a possibility of time dependence in the data. Many effects of instrumental systematics could appear in the normalized yields as a function of time during the course of a fill. Figure 3-2 shows the normalized yields of ^{1}H , ^{2}H , and ^{3}He for top and bottom detectors, separately, for each fill.

In order to check the consistency of the normalized yield for each target in a fill, the confidence level (CL) [88] is calculated and shown in figure 3-3 as a function of fill. Here the CL is the probability that a random variable having a χ^2-distribution with $N \geq 1$ degrees of freedom assumes a value which is larger than a given value $\chi^2 \geq 0$, i.e.

$$CL(\chi^2|N) = \frac{1}{\sqrt{2^N}\Gamma(\frac{1}{2}N)} \int_{\chi^2}^{\infty} \exp^{-\frac{t}{2}} t^{\frac{N}{2}-1}\, dt. \tag{3.2}$$

The CL distributions for three targets for top and bottom detectors suggest that the reduced $\chi(=\chi^2/dof)$ distributions in some fills are not quite statiscally distributed. This study thus suggests some systematic fluctuations of the normalized yields for some fills.

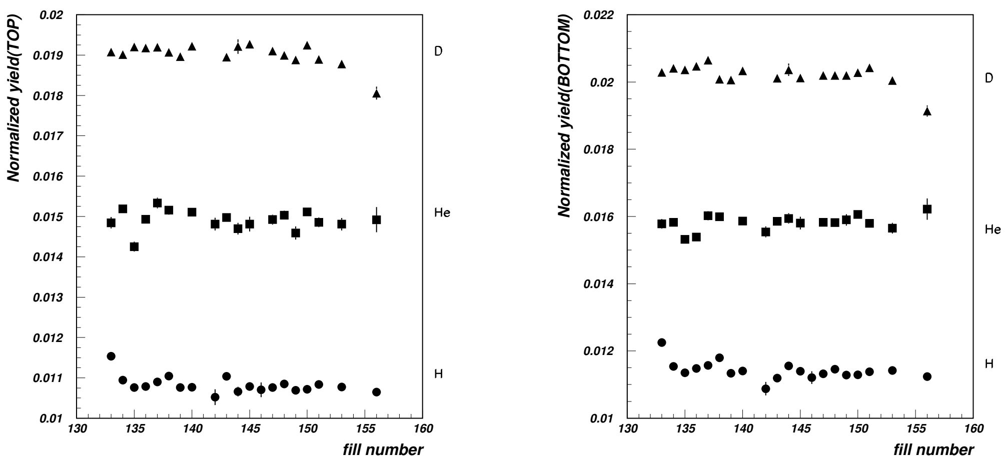

Figure 3-2: The normalized yields for top and bottom detectors as a function of fill number are shown.

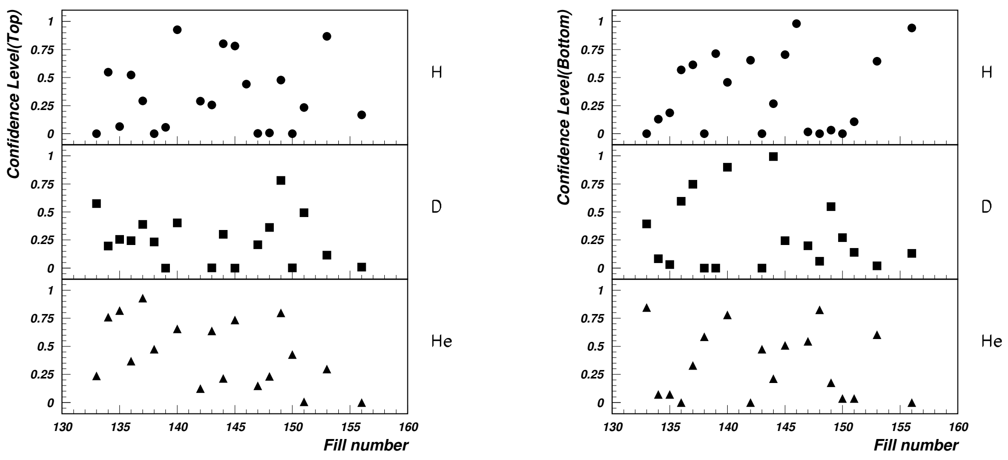

Figure 3-3: The confidence level (CL) of the each fill using the normalized yield for top-half and bottom-half detector is shown.

3.2.2 Yield vs current

The confidence levels for each fill suggested that there are additional systematic fluctuations in the normalized yields during data taking. To find more stable yield distributions during the course of data taking, the normalized yield as function of beam current is plotted for top and bottom detectors in figure 3-4. The normalized yields for each target is decreasing as the beam current is increasing. The beam current usually starts around 40 mA during ramping of the beam energy and then exponentially decays as a function of time. Therefore, the plots for the normalized yields as a function of beam current indicate that the yield is rising during the course of fill. This yield rise has been also observed in the polarized data.

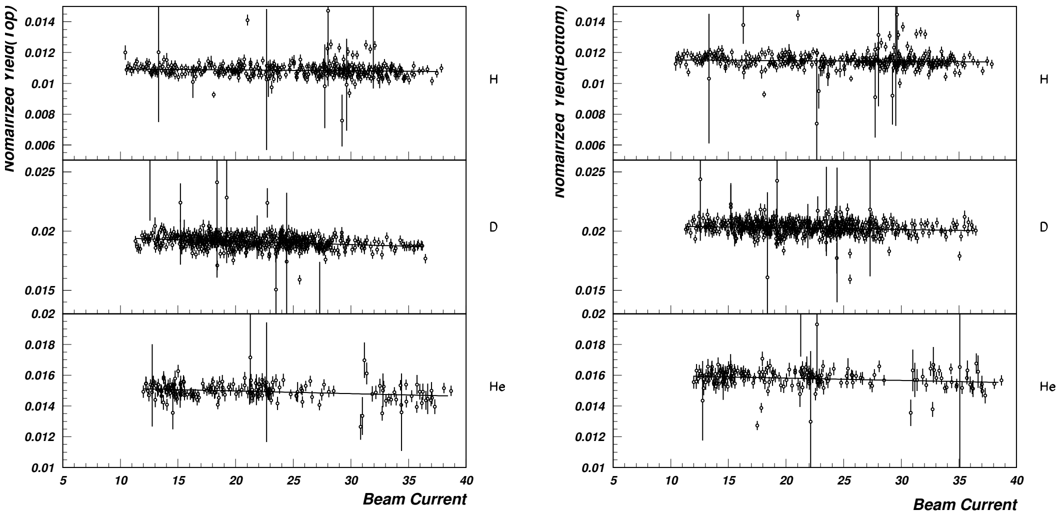

Figure 3-4: The normalized yield as a function of current is shown for the top and bottom detectors. The normalized yield is rising as the beam current decreasing.

There have been many attempts to understand and quantify the yield rise but none has been very successful. Therefore, in this thesis, the systematic uncertainty due to the normalized yield rise in the physics result will be discussed in the next chapter in the context of the extraction of the structure function ratios.

Chapter 4

Extraction of the structure function ratios

This chapter describes the procedure to extract the structure function ratios from the inclusive measurements with unpolarized ^{1}H , ^{2}H , ^{3}He from 1996 runs and ^{2}H and ^{14}N from 1997. The cross section is given by

$$\sigma(x,Q^2) = \frac{N_{DIS}(x,Q^2)}{\mathcal{L}(x,Q^2)}\eta(x,Q^2) \tag{4.1}$$

where $N_{DIS}(x,Q^2)$ is the number of DIS positrons; $\mathcal{L}(x,Q^2)$ is the integrated luminosity corrected for data-taking dead time ; $\eta(x,Q^2)$ is the radiative correction factor.

4.1 Formalism of structure function ratios

4.1.1 F_2^n/F_2^p

To extract the structure function ratio of neutron to proton, F_2^n/F_2^p , the ^{1}H and ^{2}H targets are used. Again, the double differential cross section from one photon exchange is

$$\frac{d^2\sigma}{dxdQ^2} = \frac{4\pi\alpha^2}{Q^4x}F_2(Q^2,x)[(1-y-\frac{Q^2}{4E^2}) + \frac{y^2+Q^2/E^2}{2(1+R(Q^2,x))}] \tag{4.2}$$

or by using σ_{Mott} and ϵ, explicitly

$$\frac{d\sigma}{dE'd\Omega} = \sigma_{Mott}\frac{2MxF_2(x,Q^2)}{\epsilon Q^2}[\frac{1+\epsilon R(x,Q^2)}{1+R(x,Q^2)}]. \tag{4.3}$$

Under the assumption that $\epsilon = 1$ or $R(Q^2,x)$ is the same for different nuclei, $R^d(x,Q^2) = R^p(x,Q^2)$[89], so the cross section ratio becomes a structure function ratio as

$$\frac{\sigma^d(x,Q^2)}{\sigma^p(x,Q^2)} = \frac{F_2^d(x,Q^2)}{F_2^p(x,Q^2)}.$$

Further, assuming the DIS lepton scatters incoherently from the ^{2}H target, i.e. $F_2^d = (F_2^n + F_2^p)/2$ (the deuterium is a sum of neutron and proton only without any nuclear binding effect), then the structure function ratio of neutron and proton becomes

$$\frac{F_2^n(x,Q^2)}{F_2^p(x,Q^2)} = 2\frac{\sigma^d(x,Q^2)}{\sigma^p(x,Q^2)} - 1. \tag{4.4}$$

4.1.2 $F_2^{^3He}/F_2^d$ and F_2^N/F_2^d

To make the ratio of F_2 with a non-isoscalar target to deuterium, an isoscalar correction should be applied. The iso-scalar correction factor is defined as

$$f_{iso} = \frac{A}{2}\frac{1+F_2^n/F_2^p}{Z+NF_2^n/F_2^p} \tag{4.5}$$

and is given for ^{3}He as

$$f_{iso} = \frac{3}{2}\times\frac{1+F_2^n/F_2^p}{2+F_2^n/F_2^p}. \tag{4.6}$$

Then the structure function ratio of ^{3}He to ^{2}H , $F_2^{^3He}/F_2^d$, becomes

$$\frac{F_2^{^3He}(x,Q^2)}{F_2^d(x,Q^2)} = \frac{\sigma^{^3He}(x,Q^2)}{\sigma^d(x,Q^2)} f_{iso}^{^3He}. \tag{4.7}$$

Now, using the definition of F_2^n/F_2^p in equation (4.4), the $F_2^{^3He}/F_2^d$ ratio is written

$$\frac{F_2^{^3He}(x,Q^2)}{F_2^d(x,Q^2)} = \frac{3\sigma^{^3He}(x,Q^2)}{\sigma^p(x,Q^2)+2\sigma^d(x,Q^2)}. \tag{4.8}$$

In the case of F_2^N/F_2^d , it is simply the cross section ratio

$$\frac{F_2^N(x,Q^2)}{F_2^d(x,Q^2)} = \frac{\sigma^N(x,Q^2)}{\sigma^d(x,Q^2)}.$$

4.2 Radiative corrections

Radiative corrections are both the glory and the curse of electromagnetic probes [27]. They are very important because the lepton and photon propagators lead to a strong dependence of the experimental cross section on the kinematic variables. For example, in an experiment that detects only the outgoing lepton, one cannot distinguish a high Q^2 one-photon-exchange event with large ν from a class of lower Q^2 events in which an extra photon is radiated. The larger cross section at lower Q^2 can partially compensate for the extra power of α_{em} involved in the radiative event. With electromagnetic probes, these corrections can be accurately, although quite laboriously, calculated.

Most of the earlier work on radiative corrections is based on the formalism of Mo and Tsai [90, 91, 92]. It is model-indepenent in the sense that it does not assume anything about the structure of the proton and calculates the contributions to the vertex only. However, it uses an infrared cutoff parameter to treat the infrared divergent part of the soft photon emission separately. The alternative formalism, which does not introduce an artificial division in the infrared dependence, has been developed at Dubna by Achundov *et al.* [93, 94, 95]. It does not contain any cutoff parameter, the divergence of the photon emission and vertex correction cancelling in the integration over the whole photon phase space. It uses the QPM in the sense that it considers scattering off pointlike quarks at the hadron vertex. This allows an explicit calculation of the hadron current correction. In this analysis, TERAD, which is based on the second formalism, is adapted. However, studies have shown that if the same physics is included, the numerical results of the two formalisms are the same to the level of 1-2% [96].

The measured cross section (σ_m) for inelastic lepton scattering in the experiment contains the contributions from elastic, quasi-elastic and (deep) inelastic scattering, as well as higher order electromagnetic processes. The radiative correction factor η is defined as

$$\eta(x, Q^2) = \frac{\sigma_{1\gamma}(x, Q^2)}{\sigma_m(x, Q^2)} = \frac{\sigma^B(x, Q^2)}{\sigma_m(x, Q^2)} \tag{4.9}$$

where $\sigma_{1\gamma}(\sigma^B)$ is the one photon exchange (Born) cross section. Then to extract the one photon exchange cross section from the measured cross section, the radiative correction factor $\eta(x, Q^2)$ should be applied to each nuclear target as

$$\frac{\sigma^A_{1\gamma}(x, Q^2)}{\sigma^D_{1\gamma}(x, Q^2)} = \frac{\eta^A \sigma^A_m(x, Q^2)}{\eta^D \sigma^D_m(x, Q^2)}. \tag{4.10}$$

4.2.1 TERAD

In the Dubna scheme [93, 94, 95], the measured cross section for a given x and Q^2 phase space is described as follows

$$\frac{d^2\sigma^A_m}{dxdQ^2} = \frac{d^2\sigma^B}{dxdQ^2}(e^{\delta_R} + \delta_{VR}) + \frac{d^2(\sigma_{in.tail} - \sigma_{IR} + \sigma_{QPM} + \sigma_{el.tail})}{dxdQ^2}. \tag{4.11}$$

Here, the $d^2\sigma^B/dxdQ^2$ cross section denotes the full Born cross section for deep inelastic scattering, *i.e.* the cross section containing both the one photon and one Z^0 boson exchange contribution and the δ_R is responsible for those parts of the soft and hard collinear photon emissions which could be resummed to all orders using the covariant exponential procedure. The δ^{VR} correction factor is a remnant of the exponential and of the substraction procedure used to disentangle the infrared divergent terms from the $\sigma_{in.tail}$ and contains vertex corrections. Therefore, σ_{IR} is necessary to cancel the singularity. The $\sigma_{in.tail}$ describes the inelastic radiative tail for the lepton current correction only and $\sigma_{el.tail}$ represents the contribution from elastic, quasi-elastic, and resonance radiative tails. The σ_{QPM} involves calculations based on the Quark Parton Model and reflects among other processes, the scattering with single photon emission by the quark, double photon exchange and vertex corrections on the quark line. Figures 4-1 and 4-2 show the Feynman diagrams of the radiative processes mentioned above.

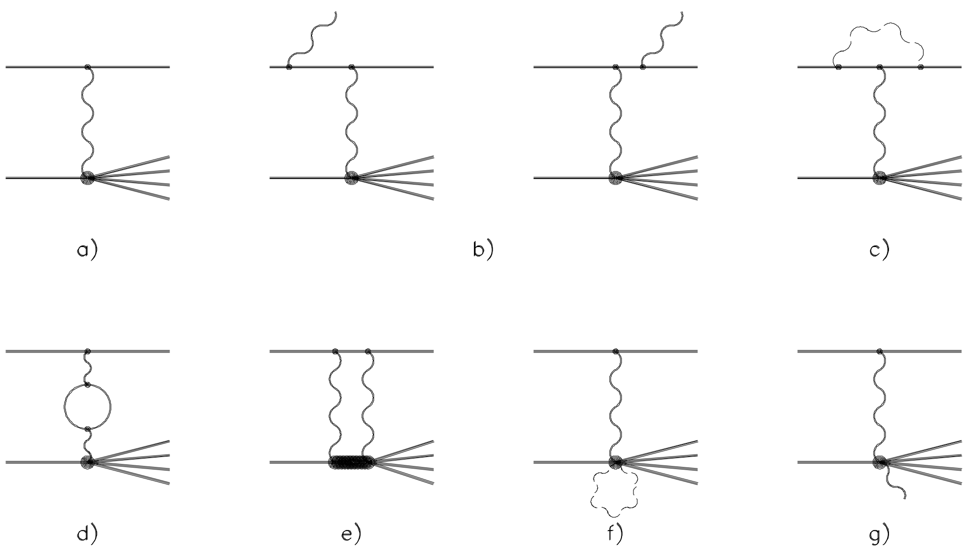

Figure 4-1: Feynman diagrams [96] for DIS in the one photon exchange approximation (a) and lowest order radiative process: real photon bremsstrahlung from the charged lepton (b), vertex corrction (c), vacuum polarization (d), double photon exchange (e), hadron current correction (f,g).

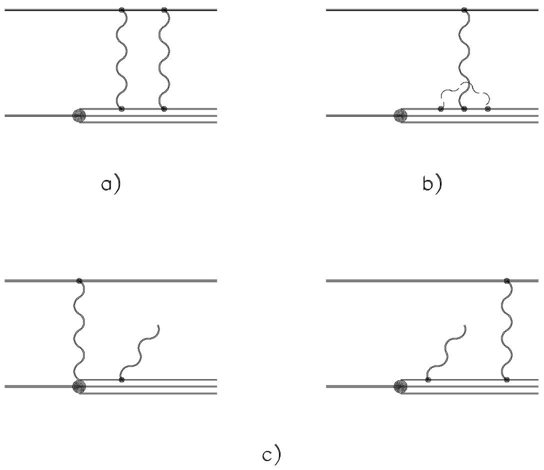

Figure 4-2: Double photon exchange (a) and hadron current corrections (b,c) are shown.

4.2.2 Standard input to the calculation

As the radiative correction calculation needs a description of the internal nucleon structure, the structure functions $F_2(x, Q^2)$ and $R(x, Q^2)$ are needed as input. This is one of the main reasons why $F_2(x, Q^2)$ is being extracted in an iterative way. Other necessary input are the electromagnetic form factors of the nuclear targets. The standard input for the radiative correction process in this analysis is as follows:

- The contribution from elastic scattering (where the radiatian of a photon changes the lepton kinematics such that it looks like a DIS event) requires the knowledge of the elastic form factor of the nucleus.
- For the similar contribution from quasielastic scattering (scattering on a nucleon inside the nucleus) the form factors of the nucleon are needed. Additionally, the probability for quasielastic scattering in this nucleus (the so called suppression factor) is needed.
- The calculation of the probablility for the radiation of a photon in a DIS event requires the knowledge of the Born cross section, i.e. the two structure functions $F_2(x, Q^2)$ and

$R(x, Q^2)$. As one wants to extract those from the measurement this usually requires an iterative procedure. Only in the case of the structure function ratio F_2^n/F_2^p which is well known from previous measurements was this iterative procedure not necessary. The major complication in the calculation of this "inelastic tail" comes from the fact that the Born cross section has to be known also outside the measured region, especially in the limit of $Q^2 \to 0$ and $W^2 \to 0$, i.e. in the so called resonance region.

Tables 4.1 and 4.2 present the set of parametrizations used in the calculations for nuclear targets. The correction for the non isoscalarity of ^{3}He was done using a simple x dependent parametrization of F_2^n/F_2^p. The most important contributions to the radiative corrections are shown in figure 4-3 for hydrogen, deuterium, ^{3}He, and nitrogen.

input	$F_2(x, Q^2)$ [97]	$R(x, Q^2)$ [65]
proton	NMC parametrization of F_2^p (1995) $x < 0.1$, $Q^2 < 0.5$: model of Badelek and Kwicienski	R_{1990}
deuteron	NMC parametrization of F_2^d (1995) $x < 0.1$, $Q^2 < 0.5$: model of Badelek and Kwicienski	R_{1990}
^{3}Helium	$F_2^d(x, Q^2))\cdot$ measured ratio measured ratio = result of final iteration (corrected for non isoscalarity)	R_{1990}
Nitrogen	$F_2^d(x, Q^2) \cdot F_2^C/F_2^d$ (NMC97)	R_{1990}

Table 4.1: Parametrizations of the Born cross section. The low x and Q^2 behavior of F_2 is described by vector meson dominance and the QPM in the model from Badelek and Kwicienski.

input	nucleon form factor [98]	nuclear form factor	suppresion factor
proton	Gari and Krümpelmann	none	none
deuteron	Gari and Krümpelmann	Locher+Svarc [99]	Bernabeu [100]
^{3}Helium	Gari and Krümpelmann	L.I.SHIFF [101]	Relativistic Fermi gas model [102]
Nitrogen	Gari and Krümpelmann	Fourier transformation of Fermi charge distribution [103]	Relativistic Fermi gas model [102]

Table 4.2: Parametrization of elastic and quasielastic scattering.

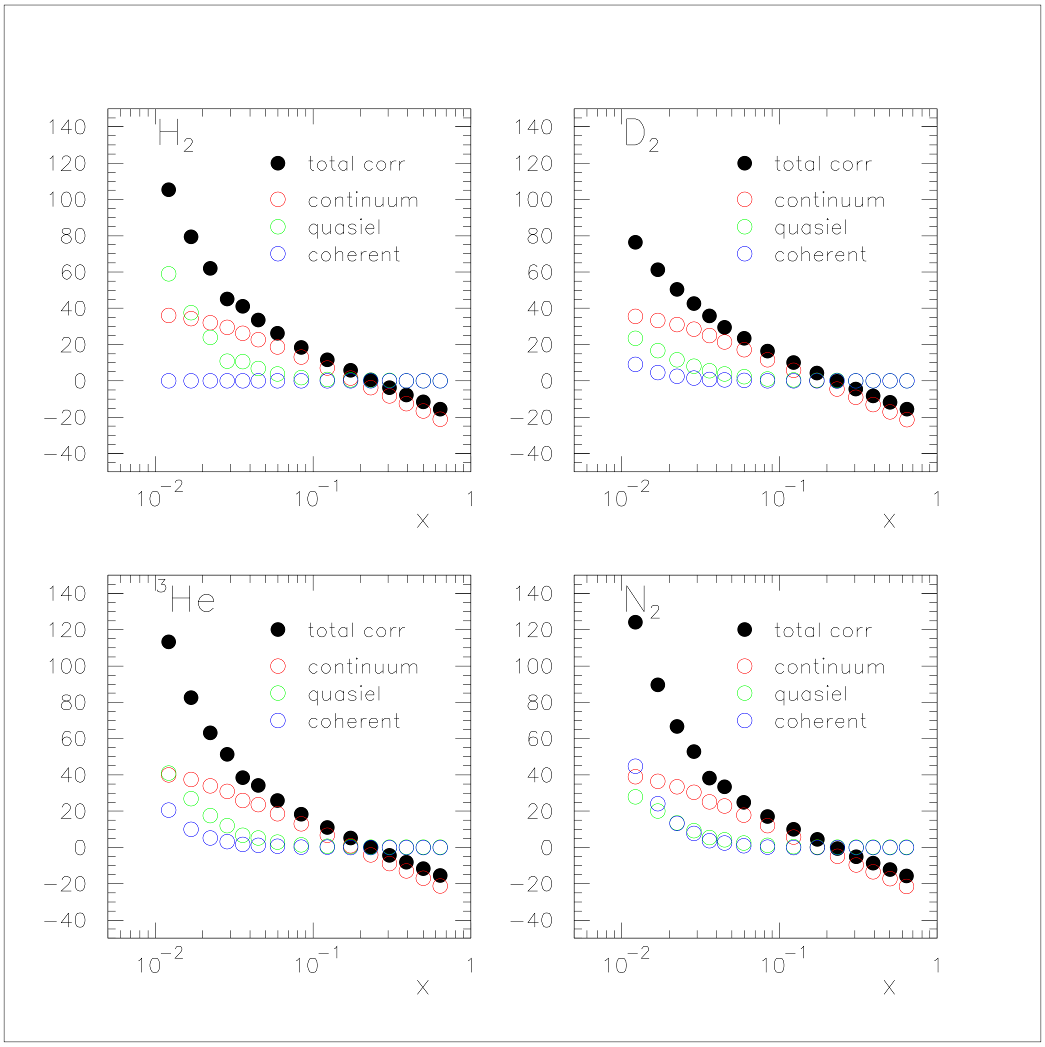

Figure 4-3: Different contributions to the total radiative corrections.

4.2.3 Iteration process

In order to check the iteration procedure, the iteration for $F_2^{^3He}/F_2^d$ was done twice:
i) starting with the assumption that $F_2^{^3He} = 1/3 \cdot (2F_2^d + F_2^p)$
ii) starting with the assumption that $F_2^{^3He} = F_2^{Pb}$. In both cases the result converged after 5 iteration steps. Convergence was defined to be reached if the deviation from the previous iteration was below 0.2% for all x bins. Despite the very different starting points, the results from the two iterations agree well with a maximum difference of 0.5 % at the lowest x bin of $x = 0.0122$. The final calculation of the radiative corrections for ^{3}He was done with a fit to the average of the two iteration results.

4.3 Systematic uncertainty

There are largely two categories of systematic uncertainties in this analysis. One is the instrumental systematic uncertainty arising from the variation of the detector responses with different data taking conditions. This systematic uncertainty is investigated with the study of the normalization uncertainty and hadron contaminations on the reconstructed positrons. The other major systematic uncertainty is from the radiative correction due to the various form factor models or parametrizations used.

4.3.1 Radiative correction uncertainties

In order to estimate the systematic uncertainties arising from the radiative corrections, all input parametrizations mentioned above have been varied. Of special importance is the influence of the parametrization of the Born cross section in the unmeasured kinematic range, i.e. its behaviour for $Q^2 \to 0$ and $W^2 \to 0$. Relatively good data exist on this for hydrogen and deuterium where the cross section in the resonance region has been measured at SLAC. This has resulted in two different parametrizations of the structure functions of the proton and the deuteron: the first includes the measured resonances while the second averages over the resonance region. The radiative corrections to F_2^n/F_2^p calculated with these two parametrizations agree to better then 0.5% over the whole x range of our measurement.

To estimate the uncertainty due to the (unknown) resonance structure of ^{3}He, the following procedure has been used for $F_2^{^3He}/F_2^d$: First, it was assumed that the functional form of $F_2^{^3He}$ in the unmeasured region is just the same as F_2^d. This assumption was used in the iteration. As an alternative a "mixture" of the proton and the deuteron has been used, i.e. $F_2^{^3He} = 1/3(2F_2^d + F_2^p)$. For both assumptions the two different parametrizations of F_2^p and/or F_2^d have been used in the calculation for ^{3}He. The resulting deviations in $F_2^{^3He}/F_2^d$ (labeled Δ^a $F_2^{^3He}/F_2^d$) are given in the following table.

As this procedure does not necessarily account for the full uncertainty in ^{3}He, an additional uncertainty has been estimated using a similar procedure: here no knowlegde of the functional form of F_2^d in the unmeasured region has been assumed and F_2^d was calculated from F_2^p and the ratio F_2^n/F_2^p ($F_2^d = 0.5F_2^p$ $(1+F_2^n/F_2^p)$). Again, different parametrizations of F_2^p have been used (in fact even more parametrizations are available for F_2^p). The resulting deviations in F_2^n/F_2^p are summarized in the following table for all x bins. The estimate of the additional uncertainty in $F_2^{^3He}/F_2^d$ (Δ^b $F_2^{^3He}/F_2^d$) is given as well and amounts to a maximum of 1.4% in the lowest x bin. The same systematic uncertainty has been assigned to the ratio F_2^N/F_2^d. An impression of the different parametrizations of F_2^p and F_2^d in the region not measured in deep inelastic scattering is given in figures 4-4 and 4-5.

The uncertainties from the other inputs to the calculation have been estimated by variations in the parametrizations and/or model assumptions. These variations included the following:

- different parametrization of the proton and neutron form factors [104]
- different parametrizations of the nuclear form factors (including the magnetic form factor for ^{14}N) [105, 106, 107, 108, 109, 110]
- different parametrizations for the nuclear suppression factors (including parametrizations of the y-scaling approach for ^{3}He and ^{14}N) [111]

x	Q^2	$\Delta^a\ F_2^{^3He}/F_2^d$ (%)	$\Delta F_2^n/F_2^p$ (%)	$\Delta^b\ F_2^{^3He}/F_2^d$ (%)
0.0122	0.49	1.7	2.8	1.4
0.0169	0.65	1.4	2.4	1.2
0.0244	0.80	0.9	2.3	1.2
0.0286	0.98	0.8	2.2	1.1
0.0359	1.15	0.6	2.0	1.0
0.0449	1.34	0.3	1.7	0.9
0.0596	1.61	0.2	1.2	0.6
0.0841	1.94	0.1	0.7	0.4
0.123	2.33	0.1	0.7	0.4
0.173	2.70	0.1	0.6	0.3
0.232	3.02	0.1	0.6	0.3
0.305	3.44	0.1	0.6	0.3
0.392	4.19	0.1	0.6	0.3
0.502	5.32	0.1	0.5	0.2
0.643	7.37	0.1	0.5	0.2

Table 4.3: Uncertainties in the radiative corrections due to uncertainties in the unmeasured part of the Born cross section.

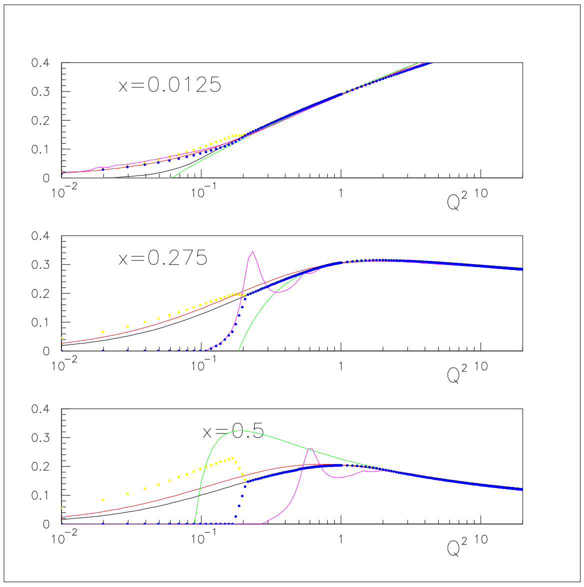

Figure 4-4: Different parametrizations of F_2^p in the unmeasured region.

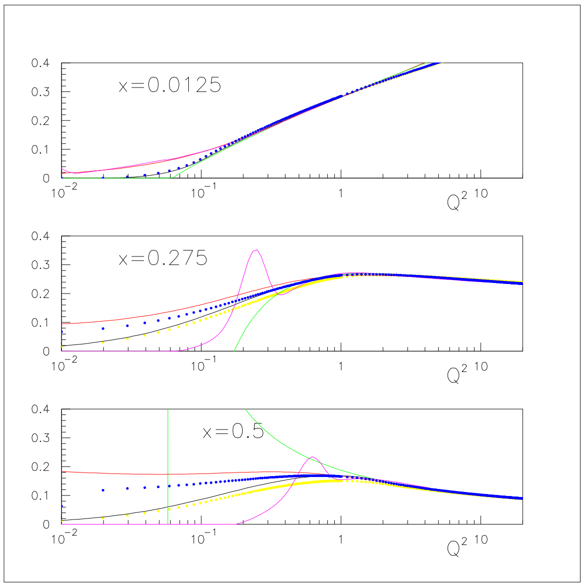

Figure 4-5: Different parametrizations of F_2^d in the unmeasured region.

- upper/lower limits for $R(x, Q^2)$
- different functional forms of the F_2^d parametrization
- upper/lower limit of the world parametrization of F_2^d

All contributions to the systematic uncertainty in F_2^n/F_2^p, $F_2^{^3He}/F_2^d$, and F_2^N/F_2^d originating from radiative corrections are summarized in tables 4.4, 4.5 and 4.6 (in %). Finally,the total uncertainties due to radiative corrections have been estimated as the quadratic sum of the different contributions and are given in table 4.7. It is worth while to note that some inputs have to be varied for the nuclear target and the deuterium target at the same time. This is true for the nucleon form factors and the parametrizations of $R(x, Q^2)$ and $F_2^d(x, Q^2)$. Consequently, only the difference between the uncertainties given for ^{3}He (^{14}N) and ^2H has been included in the total systematic uncertainties.

x	Q^2	nucleon form factors	nuclear form factor	suppression factor	$R(x, Q^2)$	$F_2(x, Q^2)$
0.0122	0.49	0.2	0.3	0.7	0.7	1.2
0.0169	0.65	0.2	0.4	0.2	0.6	1.0
0.0244	0.80	0.1	0.1	0.2	0.3	1.0
0.0286	0.98	0.0	0.0	0.2	0.1	0.6
0.0359	1.15	0.0	0.0	0.1	0.1	0.6
0.0449	1.34	0.0	0.0	0.0	0.1	0.3
0.0596	1.61	0.0	0.0	0.0	0.0	0.2
0.0841	1.94	0.1	0.0	0.0	0.0	0.1
0.123	2.33	0.1	0.0	0.0	0.0	0.2
0.173	2.70	0.0	0.0	0.0	0.0	0.3
0.232	3.02	0.0	0.0	0.0	0.0	0.2
0.305	3.44	0.0	0.0	0.0	0.0	0.1
0.392	4.19	0.0	0.0	0.0	0.0	0.1
0.502	5.32	0.1	0.0	0.0	0.0	0.1
0.643	7.37	0.1	0.0	0.0	0.0	0.3

Table 4.4: Summary of other uncertainties in F_2^n/F_2^p due to radiative corrections.

4.4 PID contamination

The DIS positrons were identified with the PID35 scheme as defined in equation (2.14). However, since each detector cannot have 100 % efficiency, the PID35 method which is a combined log-likelihood PID cannot perfectly separate the DIS positrons from hadron contamination. The DIS positrons are more likely contaminated by positively charged hadrons. Although the contamination from hadrons in DIS positron samples could be estimated by considering the parent flux distributions of different particles, the same goal has been studied with a so called "shape study".

The shape study method uses the PID35 distributions with respect to some kinematic variables. The typical PID35 distribution in this analysis usually shows the two Gaussian distributions for positive and negative values of PID35. The pid cuts are applied to PID35 > 2.0 for positrons. However, the cuts cannot completely separate the hadrons since the Gaussian distribution has such a long tail that there are some unwanted hadrons in the DIS positron sample. The PID35 distribution using all 96 unpolarized data is shown in figure 4-

x	Q^2	nucleon form factors		nuclear form factors		suppression factors		$R(x,Q^2)$		$F_2(x,Q^2)$	
		^{3}He	D	^{3}He	D	^{3}He	D	^{3}He	D	^{3}He	D
0.0122	0.49	0.1	0.0	4.0	0.4	0.1	1.3	1.9	1.6	1.0	0.9
0.0169	0.65	0.0	0.0	2.6	0.2	0.4	0.8	1.2	1.0	0.9	1.0
0.0244	0.80	0.0	0.0	1.3	0.1	0.5	0.9	1.0	0.8	1.1	1.0
0.0286	0.98	0.1	0.0	0.7	0.1	0.5	0.9	0.7	0.7	0.6	0.7
0.0359	1.15	0.1	0.1	0.3	0.0	0.4	0.7	0.4	0.4	0.4	0.4
0.0449	1.34	0.1	0.1	0.2	0.0	0.3	0.1	0.3	0.3	0.4	0.4
0.0596	1.61	0.1	0.1	0.1	0.0	0.2	0.1	0.2	0.2	0.2	0.2
0.0841	1.94	0.1	0.1	0.0	0.0	0.2	0.0	0.1	0.1	0.2	0.2
0.123	2.33	0.0	0.0	0.0	0.0	0.1	0.0	0.0	0.0	0.2	0.2
0.173	2.70	0.0	0.0	0.0	0.0	0.1	0.0	0.0	0.0	0.2	0.2
0.232	3.02	0.0	0.0	0.0	0.0	0.0	0.0	0.0	0.0	0.3	0.3
0.305	3.44	0.0	0.0	0.0	0.0	0.0	0.0	0.0	0.0	0.4	0.4
0.392	4.19	0.1	0.0	0.0	0.0	0.0	0.0	0.0	0.0	0.4	0.4
0.502	5.32	0.0	0.0	0.0	0.0	0.0	0.0	0.0	0.0	0.3	0.3
0.643	7.37	0.0	0.1	0.0	0.0	0.0	0.0	0.0	0.0	0.3	0.3

Table 4.5: Summary of other uncertainties in $F_2^{^3He}/F_2^d$ due to radiative corrections.

x	Q^2	nucleon form factors		nuclear form factors		suppression factors		$R(x,Q^2)$		$F_2(x,Q^2)$	
		^{14}N	D	^{14}N	D	^{14}N	D	^{14}N	D	^{14}N	D
0.0122	0.49	0.0	0.0	6.1	0.4	1.2	1.3	2.1	1.6	1.0	0.9
0.0169	0.65	0.0	0.0	4.3	0.2	0.2	0.8	1.4	1.0	0.7	1.0
0.0244	0.80	0.0	0.0	3.2	0.1	0.0	0.9	1.0	0.8	0.9	1.0
0.0286	0.98	0.0	0.0	2.1	0.1	0.0	0.9	0.8	0.7	0.6	0.7
0.0359	1.15	0.1	0.1	1.2	0.0	0.0	0.7	0.4	0.4	0.4	0.4
0.0449	1.34	0.1	0.1	1.1	0.0	0.0	0.1	0.4	0.3	0.4	0.4
0.0596	1.61	0.1	0.1	0.6	0.0	0.0	0.1	0.2	0.2	0.2	0.2
0.0841	1.94	0.1	0.1	0.3	0.0	0.0	0.0	0.1	0.1	0.2	0.2
0.123	2.33	0.0	0.0	0.1	0.0	0.0	0.0	0.0	0.0	0.2	0.2
0.173	2.70	0.0	0.0	0.0	0.0	0.0	0.0	0.0	0.0	0.1	0.2
0.232	3.02	0.0	0.0	0.0	0.0	0.0	0.0	0.0	0.0	0.2	0.3
0.305	3.44	0.0	0.0	0.0	0.0	0.0	0.0	0.0	0.0	0.3	0.4
0.392	4.19	0.0	0.0	0.0	0.0	0.0	0.0	0.0	0.0	0.4	0.4
0.502	5.32	0.0	0.0	0.0	0.0	0.0	0.0	0.0	0.0	0.3	0.3
0.643	7.37	0.1	0.1	0.0	0.0	0.0	0.0	0.0	0.0	0.3	0.3

Table 4.6: Summary of other uncertainties in F_2^N/F_2^d due to radiative corrections.

x	Q^2	$\Delta\ F_2^n/F_2^p$ (%)	$\Delta\ F_2^{^3He}/F_2^d$(%)	$\Delta F_2^N/F_2^d$ (%)
0.0122	0.49	3.2	4.7	6.8
0.0169	0.65	2.7	3.3	4.8
0.0244	0.80	2.5	2.3	3.7
0.0286	0.98	2.3	1.8	2.7
0.0359	1.15	2.1	1.5	1.8
0.0449	1.34	1.7	1.0	1.5
0.0596	1.61	1.2	0.7	0.9
0.0841	1.94	0.7	0.5	0.5
0.123	2.33	0.7	0.4	0.4
0.173	2.70	0.7	0.3	0.3
0.232	3.02	0.6	0.3	0.3
0.305	3.44	0.6	0.3	0.3
0.392	4.19	0.6	0.3	0.3
0.502	5.32	0.5	0.2	0.2
0.643	7.37	0.6	0.2	0.2

Table 4.7: Total uncertainties in F_2^n/F_2^p and $F_2^{^3He}/F_2^d$ due to radiative corrections.

6. The line-shaded area (PID35 $>$ 2.0) is for positrons and the dot-shaded area (PID35 $>$ -2.0)) is for hadrons. Therefore, by comparing the area of the two distributions over the region of PID35 $>$ 2.0, the hadron contamination in the positron sample is evaluated at the kinematics of the measurement. Figure 4-7 shows PID35 distributions in 15 x bins. By comparing the integrals of two Gaussians over the region of PID35 $>$ 2.0, the hadron contamination in the positron samples is evaluated. The results for 15 x bins are given in Table 4.8.

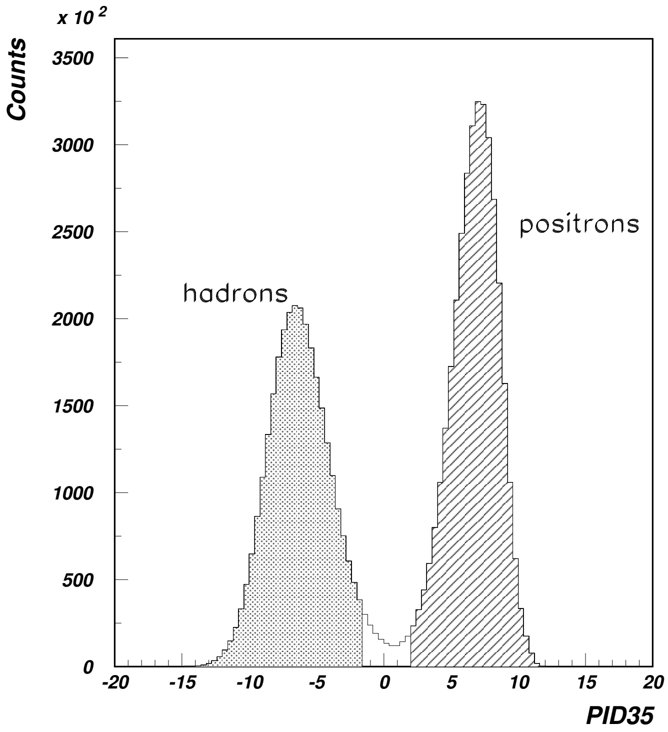

Figure 4-6: The PID35 distributions. The line-shaded area is for positrons and the dot-shaded area is for hadrons.

4.5 Normalization uncertainty

To evaluate the normalization uncertainty in the structure function ratios due to the various systematic variations of instruments or time dependence during data taking peroids, an absolute knowledge of the cross section is needed. Then the normalization uncertainty in the structure function ratios could be determined. The same goal could be achieved by the

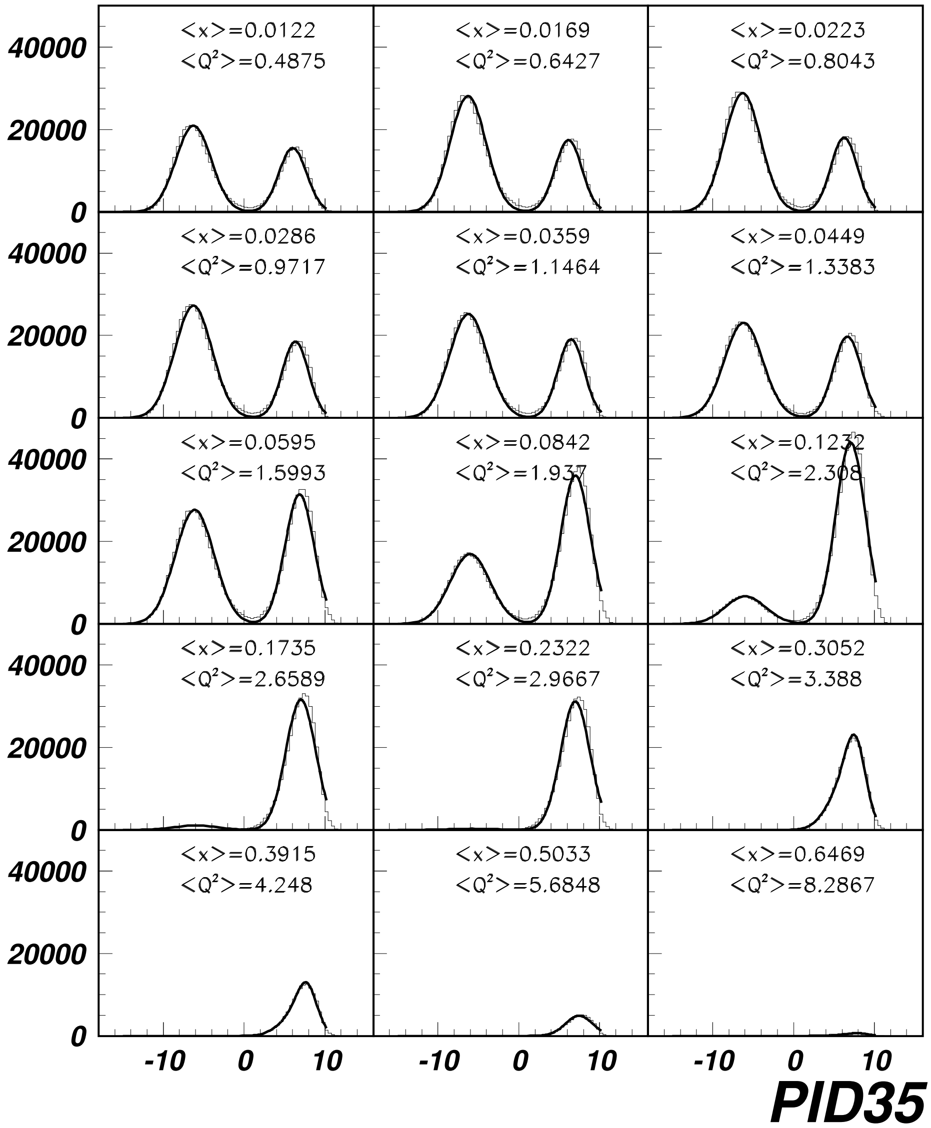

Figure 4-7: The PID35 distributions for 15 x bins are shown. The hadron contamination in the PID35 $>$ 2.0 sample is calculated using the two Gaussian fits from both positron and hadron distributions. The integrals from both distributions are thus calculated from the two Gaussian function with the range of $2.0 <$ PID35 $< \infty$.

$< x >$	$< Q^2 >$	h contamination(%)
0.0122	0.4875	0.4
0.0169	0.6427	0.5
0.0223	0.8043	0.6
0.0286	0.9717	0.7
0.0359	1.1464	0.7
0.0449	1.3383	0.7
0.0595	1.5993	0.6
0.0842	1.9370	0.5
0.1232	2.3080	0.2
0.1735	2.6589	0.1
0.2322	2.9667	0.0
0.3052	3.3880	0.0
0.3915	4.2480	0.0
0.5033	5.6848	0.0
0.6469	8.2867	0.0

Table 4.8: The hadron contaminations of the positron sample for given $< x >$ and $< Q^2 >$ are calculated using the double Gaussian function fit and the results are given in %.

use of similar measurements from other previous experiments. In the case of the measurement of F_2^n/F_2^p, there are already very precise data from the NMC and E665 experiments. Therefore, the HERMES extraction of F_2^n/F_2^p in this thesis is compared with the NMC parametrization of F_2^n/F_2^p .

Although detector efficiency cuts are applied to isolate good or bad performance of the detectors, the rise in the normalized yield during the course of a fill (see figure 3-4) suggests unknown effects which can change the cross section ratio measurements. Therefore, the study of normalization uncertainties involves finding the maximum variation of the structure function ratios with respect to different data samples. The idea is that any extraction method of the structure function ratios using different means to group the data should yield the same result within statistical uncertainties.

The typical way to extract the structure function ratios is to use a fill-by-fill analysis. Considering each fill as an independent experiment, it produces a structure function ratio r_i

Type	Target Combinations
A	D - He - H
B	He - H - D
C	H - D - He
D	D - H - He
E	H - D - He - H - D - He
F	He - H - D - He - H - D

Table 4.9: Most frequently used target running patterns in the 1996 data taking period.

with uncertainty σ_i^2. Thus, the final weighted average result from all fills can be determined. The formulae for the average ($\hat{\mu}$) and variance($\hat{\sigma}^2$) are as follows:

$$\begin{aligned} \hat{\mu} &= \frac{\sum r_i/\sigma_i^2}{\sum 1/\sigma_i^2} \\ \hat{\sigma}_i^2(\mu) &= \frac{1}{\sum 1/\sigma_i^2} \end{aligned} \tag{4.12}$$

A fill usually lasted for about 8 hours for unpolarized target runs during data taking and the running time of one target usually lasted about 1 - 2 hours. If the running time for a given target is very short and randomly distributed during the course of a fill, the normalization uncertainty due to the yield rise or time dependence would be minimized. However, the fill-by-fill method could be blinded from the possible effects of the yield rising. A possible systematic effect could occur when the target exchanges in a fill are not perfectly random and combined in the fill-by-fill analysis. Table 4.9 summarizes the target-running-order which was used in the 96 unpolarized data taking period.

Figure 4-8 illustrates a possible effect from the yield rising in a fill. In this plot, if we assume that the quantity we try to calculate is $f = Y_1/Y_2$, it is easy to see that the ratio of Y_1 to Y_2 could be quite different from the group pairs which could be expressed as a pair of (Y_1, Y_2) using the given number in the figure. For example, the ratio of Y_1 to Y_2 from (1,1) will be very different from (1,5) since the slopes of normalized yields Y_1 and Y_2 are different. Therefore, the normalization uncertainties for F_2 ratios are estimated by

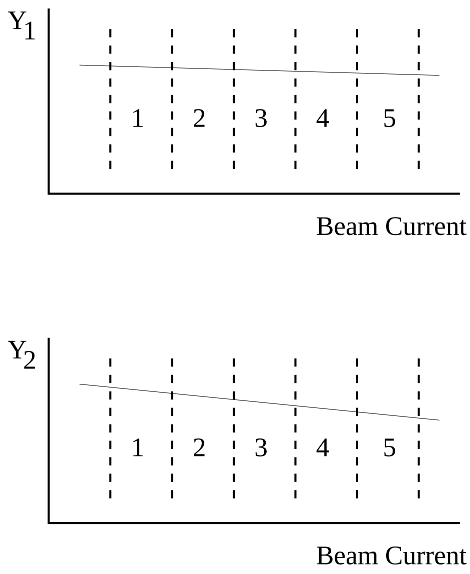

Figure 4-8: The normalized yield as function of beam current is shown with arbitrary group.

comparing the results from various extraction methods such as fill-by-fill, beam-current-binning, and whole-run method.

4.5.1 F_2^n/F_2^p

4.5.1.1 HERMES F_2^n/F_2^p vs NMC

Figure 4-9 shows the previous measurements of F_2^n/F_2^p from the NMC, SLAC, and E665 experiments. To estimate the normalization uncertainty for the extraction of F_2^n/F_2^p from HERMES data, the F_2^n/F_2^p ratio from NMC [89] is parametrized as a function of x with modified Q^2 value for HERMES. For a given x, the NMC parametrization of F_2^n/F_2^p is given as

$$\frac{F_2^n}{F_2^p} = p1(\frac{Q^2}{20})^{p2}(1 + x^2Q^2) \tag{4.13}$$

with

$$
\begin{aligned}
Q^2 &= 0.070895 + 37.107x - 227.38x^2 + 735.41x^3 - 1058.7x^4 + 568.88x^5 \\
p1 &= 0.979 - 1.692x + (2.797x^2) - (4.313x^3) + 3.075x^4 \\
p2 &= -0.171x^2 + 0.244x^3.
\end{aligned}
\tag{4.14}
$$

The uncertainty associated with the NMC F_2^n/F_2^p parametrization is estimated as 0.2% for the entire x range. Using this parametrization, the ratios of HERMES and NMC F_2^n/F_2^p for 15 x bins are calculated and then applied to make a straight line fit. From the best fit, the slope and error are quoted as normalization uncertainty and its error.

Figure 4-10 displays the results of three extraction methods with the NMC parametrization and figure 4-11 and table 4.10 summarizes the fits and their results. The maximum deviation from the NMC result is observed in beam-current-binning extraction method, as expected.

	r	δ r	χ^2/dof	$\sqrt{\chi^2}/dof \times \delta r$
Whole-run	1.0043	0.26517E-02	0.2972E+01	0.26517E-02
beam-current-binning	1.0114	0.24072E-02	0.3950E+01	0.24072E-02
Fill-by-fill	1.0073	0.27424E-02	0.2560E+01	0.27424E-02

Table 4.10: The ratio fit results for different extraction methods. The current grouping of data (beam-current-binning) shows the maximum deviation from unity with reasonable error.

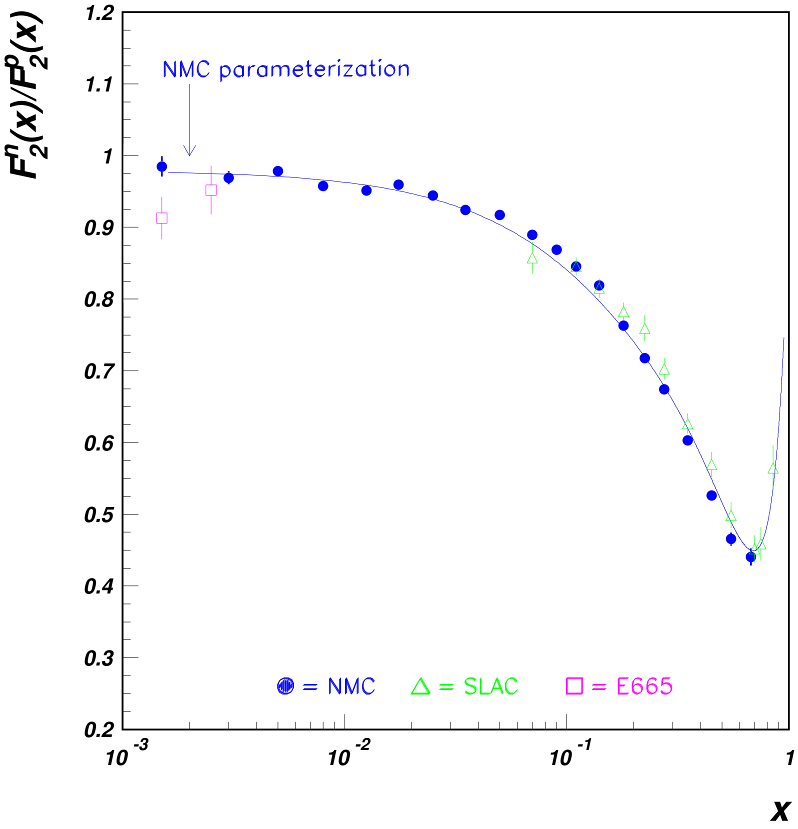

Figure 4-9: The NMC, SLAC, and E665 measurements of F_2^n/F_2^p as a function of x is shown. The NMC parametrization of F_2^n/F_2^p is used for the absolute measurement with 0.2% of normalization uncertainty. E665 data points at lower x values are not shown.

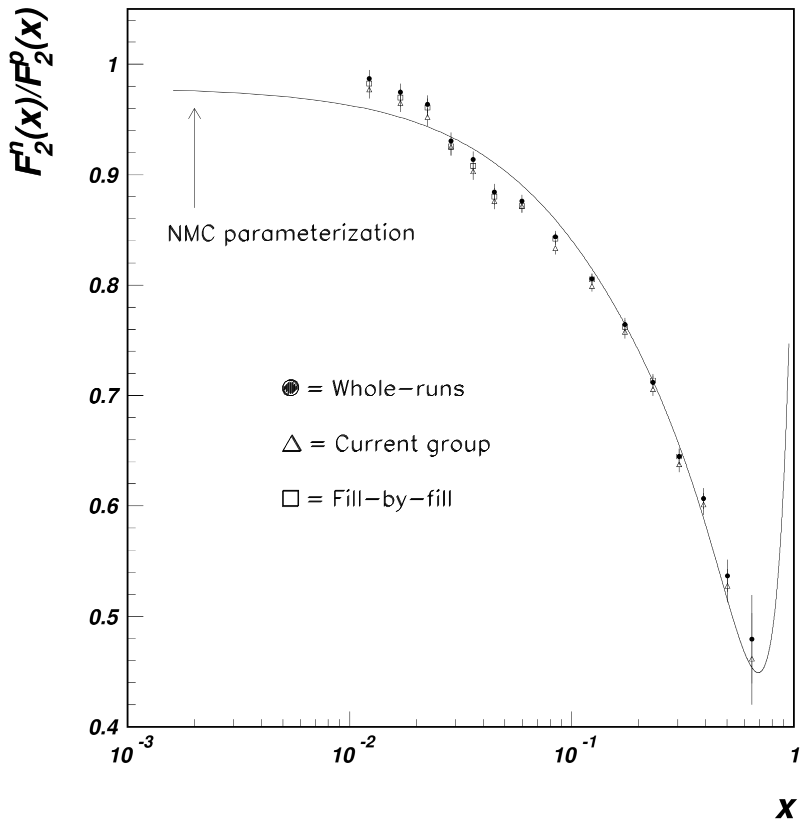

Figure 4-10: F_2^n/F_2^p from HERMES data using the three different extraction methods.

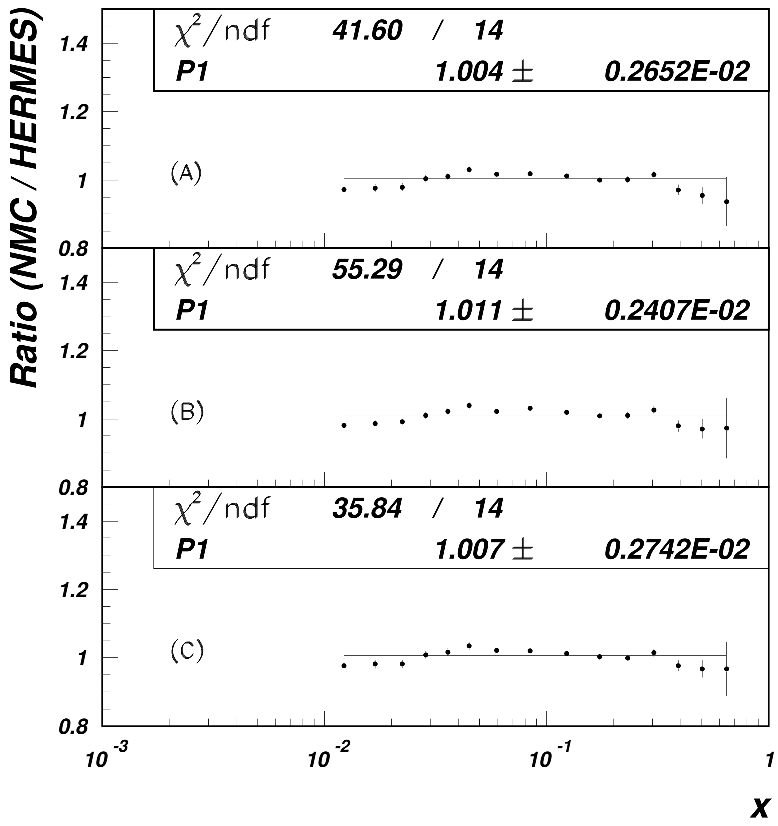

Figure 4-11: The ratio fit of F_2^n/F_2^p of NMC to HERMES as function of x. The (A) panel is the ratio fit of NMC to Whole-runs, (B) is NMC to Current group ,and (C) is NMC to fill-by-fill.

4.5.1.2 Fluctuation Study

Fluctuations were studied in the same way as in the previous section. The only difference is that no use was made of the NMC parametrization of F_2^n/F_2^p. For instance, in the case of the fill-by-fill extraction method, the 18 fills are available. After extracting F_2^n/F_2^p from each fill, the ratio fits among 18 fills was attempted to determine the fluctuation of fill-by-fill results. The number of pairs out of 18 fills is 153. Figure 4-12 shows the ratios and χ^2/dof for 153 pairs from 18 fills and 4-13 shows the 10 pairs from the 5 current groups. Also, Table 4.11 summarizes the mean and variation of data samples with respect to different extraction methods. The maximum variation from unity is also observed in the beam-current-binning method.

	r	δr	r	$\sqrt{\chi^2}/dof \times \delta r$
beam-current-binning	1.013840	0.002614	1.013708	0.002632
Fill-by-fill	0.994688	0.001575	0.997729	0.001487

Table 4.11: The ratio fit results for different extraction methods. The current grouping of data shows the maximum deviation from unity with reasonable error.

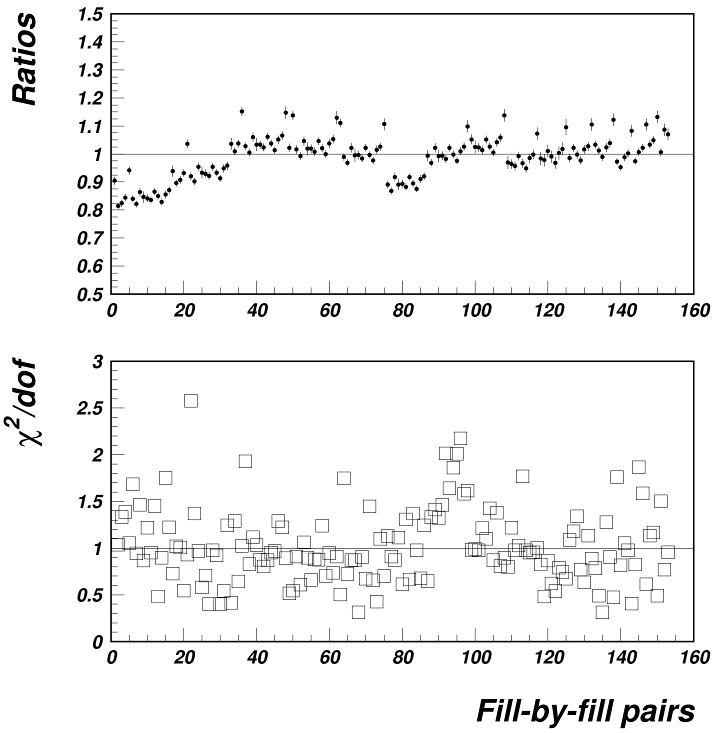

Figure 4-12: The top panel shows the results for F_2^n/F_2^p ratio fits from the 153 pairs in the fill-by-fill extraction method and the χ^2/dof of the fits is shown in the bottom panel.

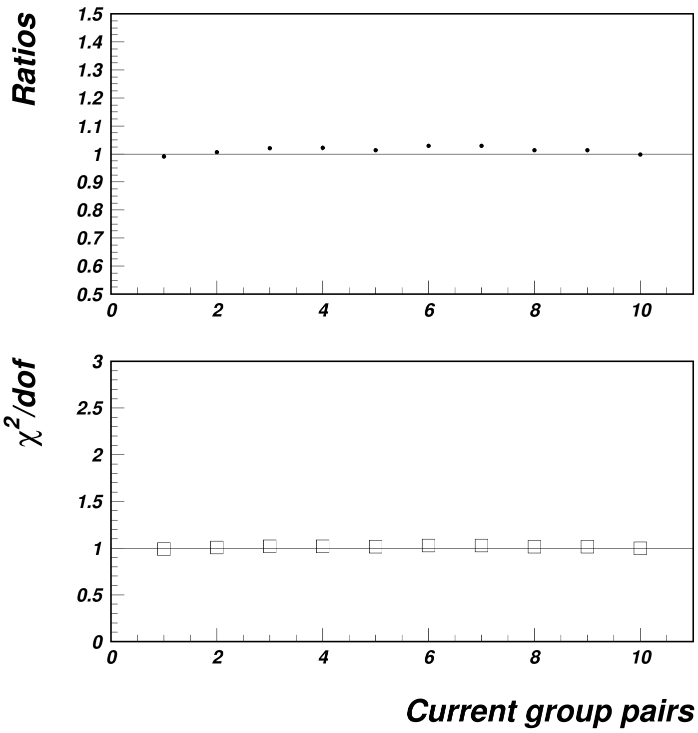

Figure 4-13: The top panel shows the results for F_2^n/F_2^p ratio fits from the 10 pairs in the beam-current-binning extraction method and the χ^2/dof of the fits is shown in the bottom panel.

4.5.2 $F_2^{^3He}/F_2^d$

The study of the normalization uncertainty of $F_2^{^3He}/F_2^d$ could be done with exactly the same methods used for F_2^n/F_2^p . However, it is not possible to do the same studies for $F_2^{^3He}/F_2^d$, since there is no previous measurement of $F_2^{^3He}/F_2^d$. Also, if the nuclear effects on F_2 ratios are known to good precision, the modification to ^{3}He could be applied to make the F_2 ratio of ^{3}He to ^{2}H by using the NMC [41] data. However, this is not very reliable since so many models are involved and futhermore in the interesting low x range very reliable phenomenological models cannot be applied. Therefore, a different approach for the normalization study of $F_2^{^3He}/F_2^d$ was done using two extraction formulae for $F_2^{^3He}/F_2^d$. One method is to use ^{3}He and ^{2}H data with an isoscalar correction function f_{iso} using the NMC parametrization of F_2^n/F_2^p ; the second is to use ^{3}He , ^{2}H and ^{1}H data without an isoscalar correction function. In this thesis, the normalization study of $F_2^{^3He}/F_2^d$ is done by comparing two results from three different extraction methods.

4.5.2.1 Two target and three target methods

The two different expressions with the same physics are rewritten as below:
The two-target method:

$$\frac{F_2^{^3He}(x,Q^2)}{F_2^d(x,Q^2)} = \frac{\sigma^{^3He}(x,Q^2)}{\sigma^d(x,Q^2)} f_{iso}^{^3He} \tag{4.15}$$

The three-target method:

$$\frac{F_2^{^3He}(x,Q^2)}{F_2^d(x,Q^2)} = \frac{3\sigma^{^3He}(x,Q^2)}{\sigma^p(x,Q^2) + 2\sigma^d(x,Q^2)}. \tag{4.16}$$

Allowing 0.2 % of error from the NMC F_2^n/F_2^p parametrization, the two-target and three-target method are applied to extract $F_2^{^3He}/F_2^d$ with three different extraction methods: fill-by-fill, beam-current-binning, and whole-run. Figure 4-14, 4-15, and 4-16 illustrate the results of the comparisons. All extraction methods show excellent agreement of the three-target and the two-target method within 0.3 % over the entire x range. These results clearly indicate that the evaluation of the normalization uncertainty for $F_2^{^3He}/F_2^d$ is needed using only the three-target method with different extraction methods.

4.5.2.2 Normalization uncertanity

A study of the normalization uncertainty using whole-run, fill-by-fill, and beam-current-binning extraction methods was carried out. The comparison of the different extraction methods with the three-target method is shown in figure 4-17 and the ratio fit for each method is shown in figure 4-18. These results indicate that the maximal deviation in the ratio between whole-run and beam-current-binning is 0.4%.

4.5.2.3 Fluctuation study

As in the case of F_2^n/F_2^p, the same fluctuation study is conducted and the results are shown in figures 4-19 and 4-20. Table 4.12 summarizes the results.

	r	δr	r	$\sqrt{\chi^2}/dof \times \delta r$
Beam-current-binning	1.002882	0.001356	1.003168	0.001140
Fill-by-fill	0.989279	0.000824	0.988743	0.000819

Table 4.12: The ratio fit results for different extraction methods. The current grouping of data (beam-current-binning) shows the maximum deviation from unity with reasonable error.

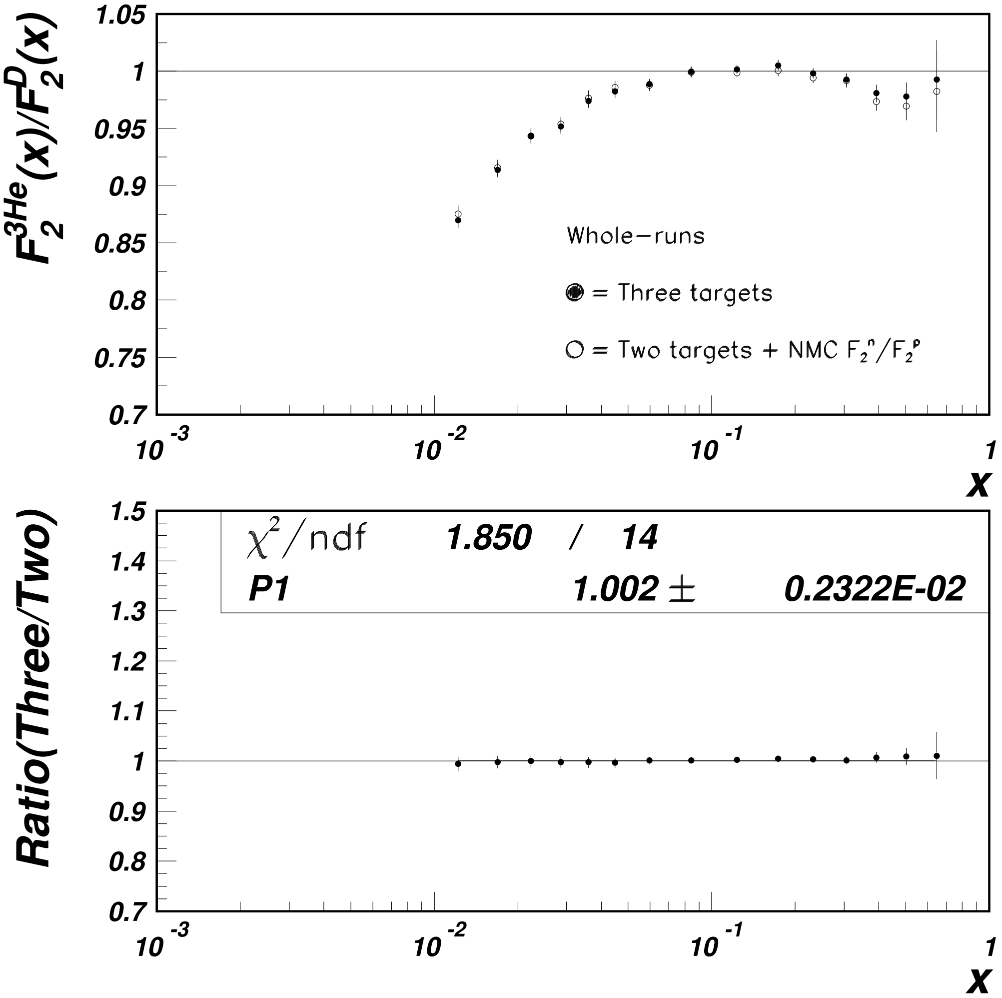

Figure 4-14: The comparison of the two-target method and three-target method with NMC F_2^n/F_2^p data using the whole-run extraction method for $F_2^{^3He}/F_2^d$ is shown in the top panel. The ratio of the two results is shown in the bottom panel.

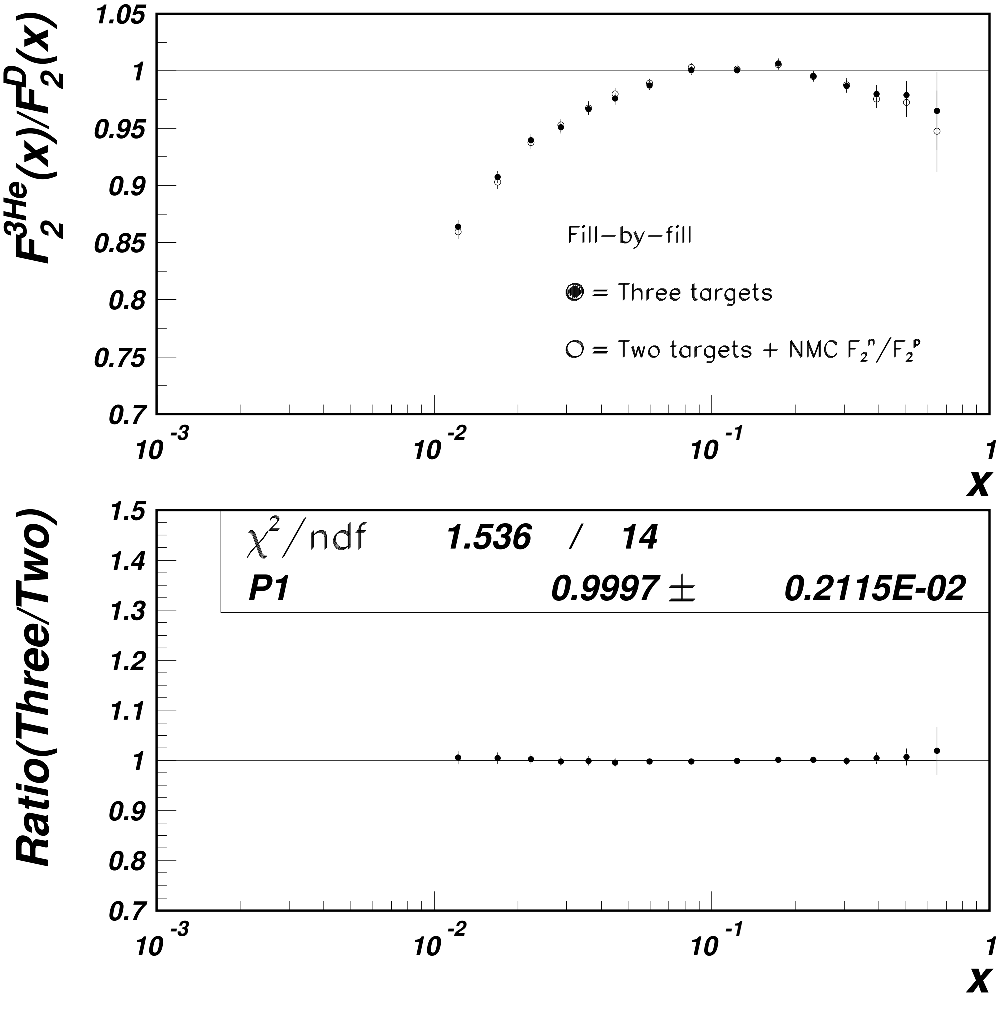

Figure 4-15: The comparison of the three-target method and two-target method with NMC F_2^n/F_2^p data using fill-by-fill extraction for $F_2^{^3He}/F_2^d$ is shown in the top panel. The ratio of the two results is shown in the bottom panel.

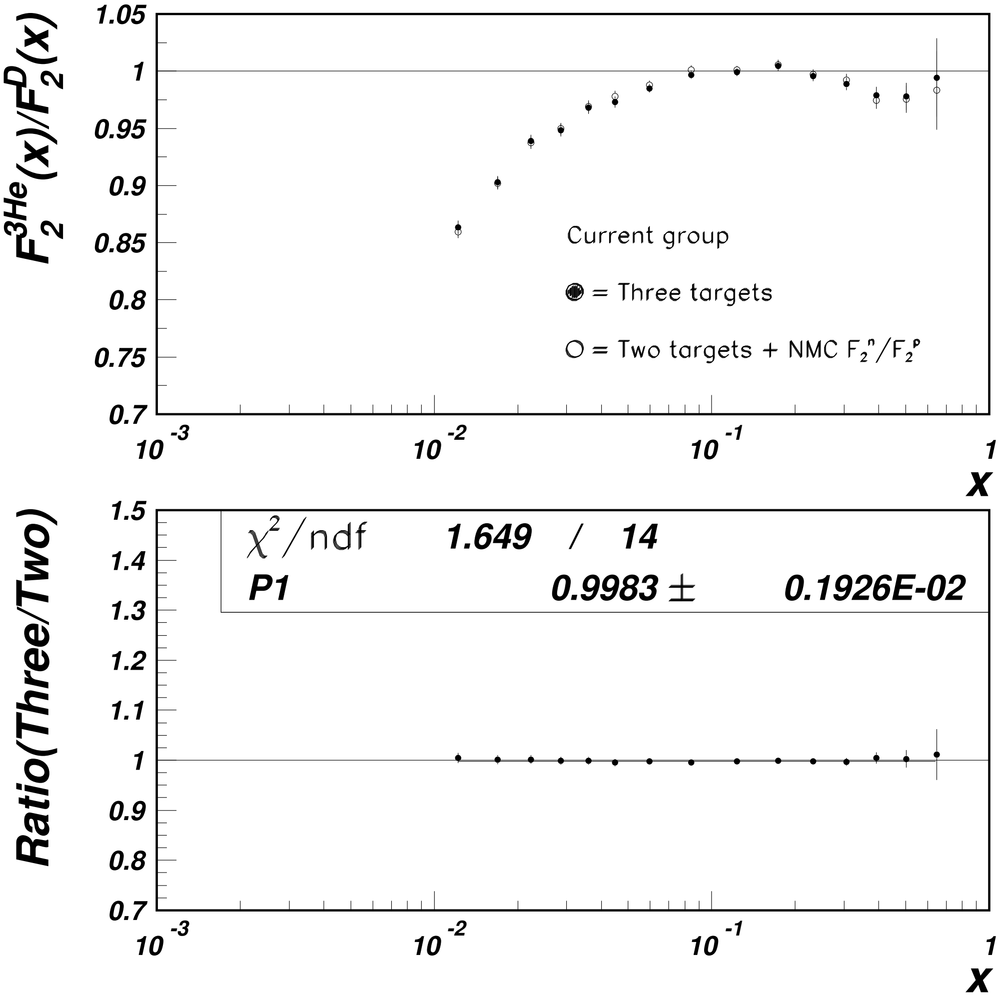

Figure 4-16: The comparison of the three target method and the two target methods with NMC F_2^n/F_2^p data using the beam-current-binnig extraction method for F_2^{3He}/F_2^d is shown in the top panel. The ratio of the two results is shown in the bottom panel.

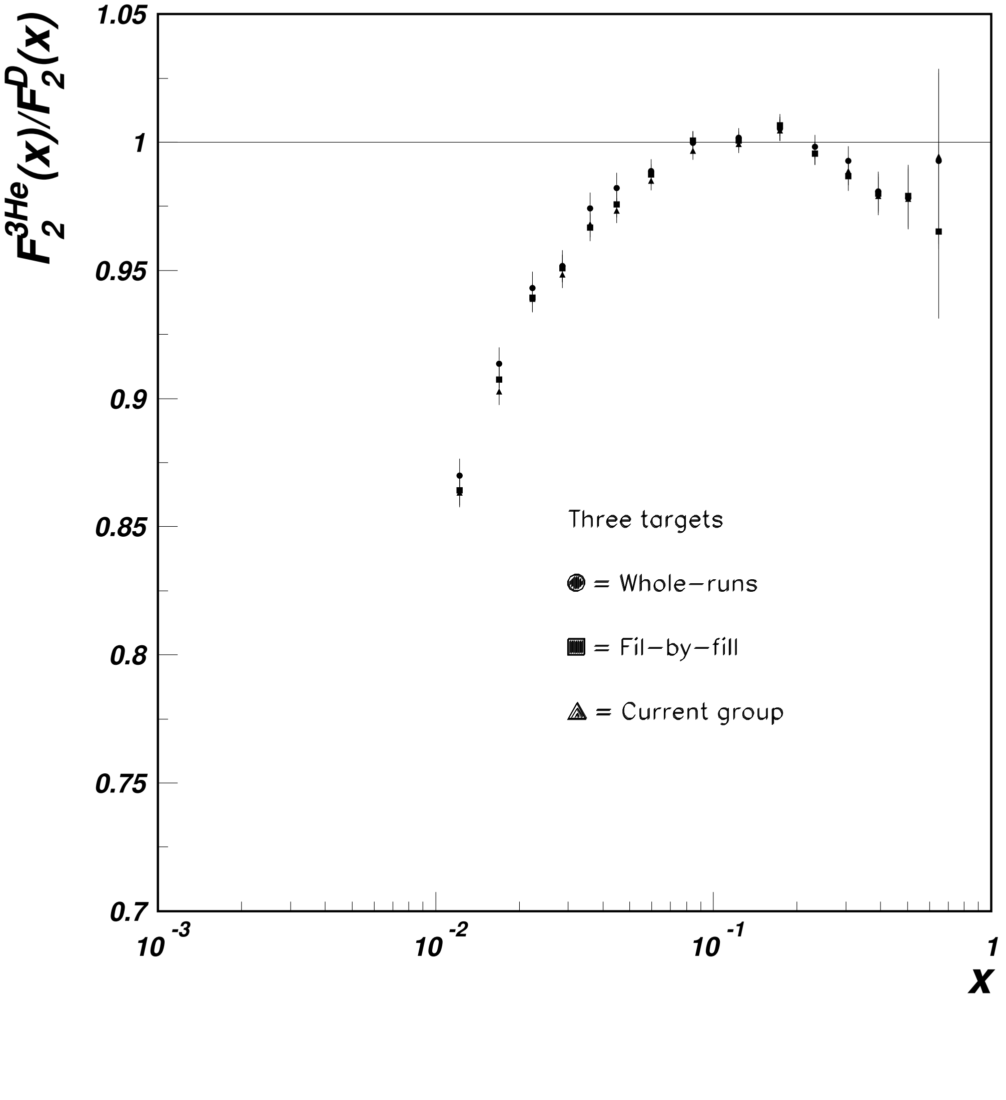

Figure 4-17: The three-target method results for $F_2^{^3He}/F_2^d$ using whole-run, fill-by-fill, and beam-current-binning extraction methods is shown.The three results are in good agreement within statistical errors.

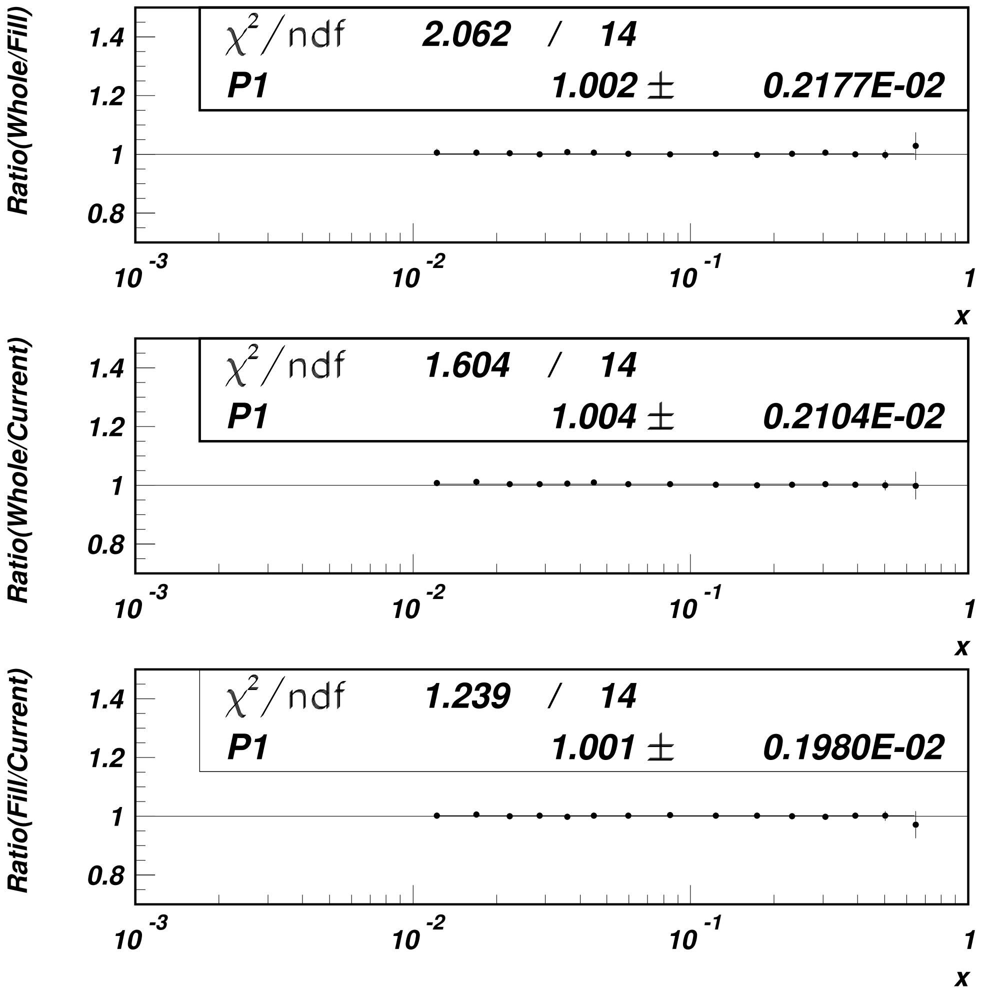

Figure 4-18: The ratio fit between whole-run and the fill-by-fill extraction methods using the three-target method is shown in the top panel; the ratio fit between the whole-run and the fill-by-fill extraction method is shown in the middle panel; the ratio fit between the fill-by-fill and the beam-current-binning extraction method is shown in the bottom panel.

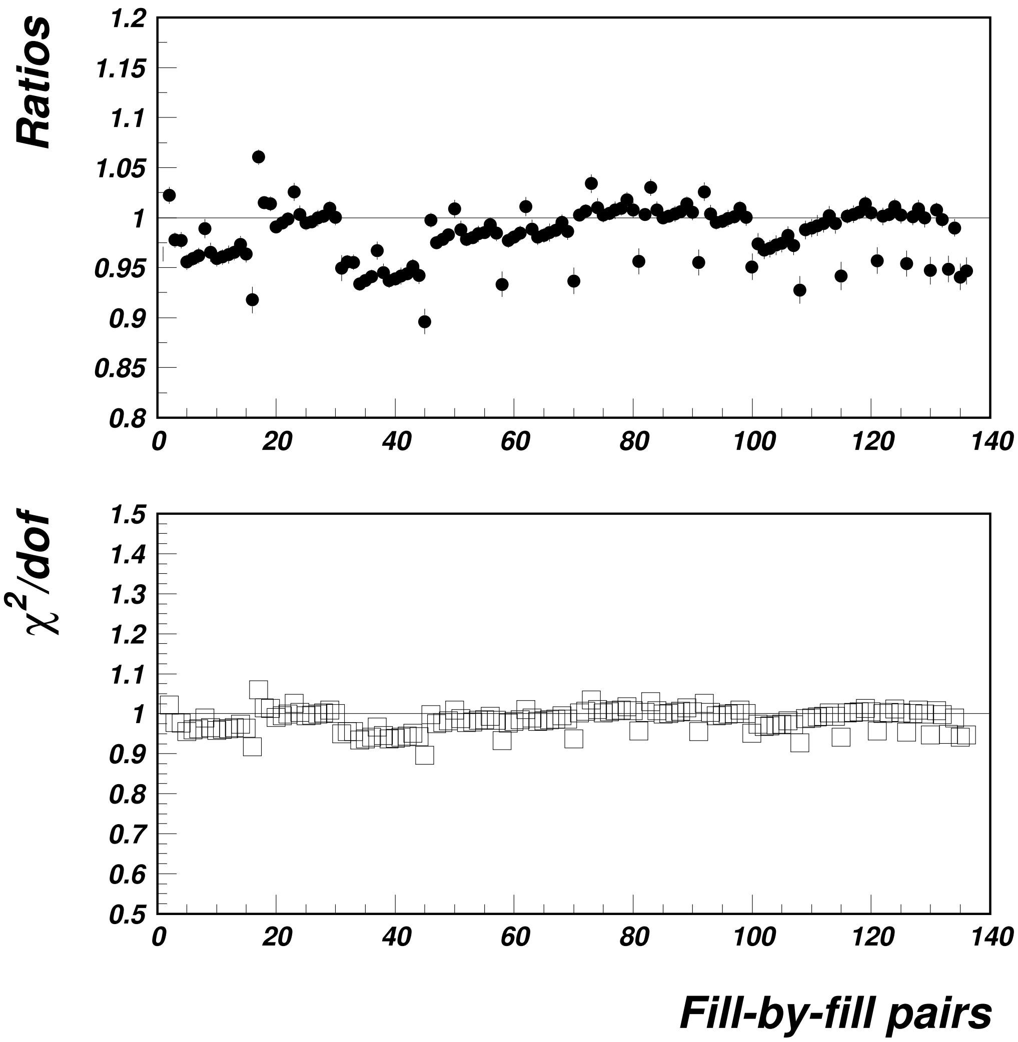

Figure 4-19: The top panel shows the results of $F_2^{^3He}/F_2^d$ ratio fits from the 136 pairs using the fill-by-fill extraction method and the χ^2/dof of the fits are shown in the bottom panel.

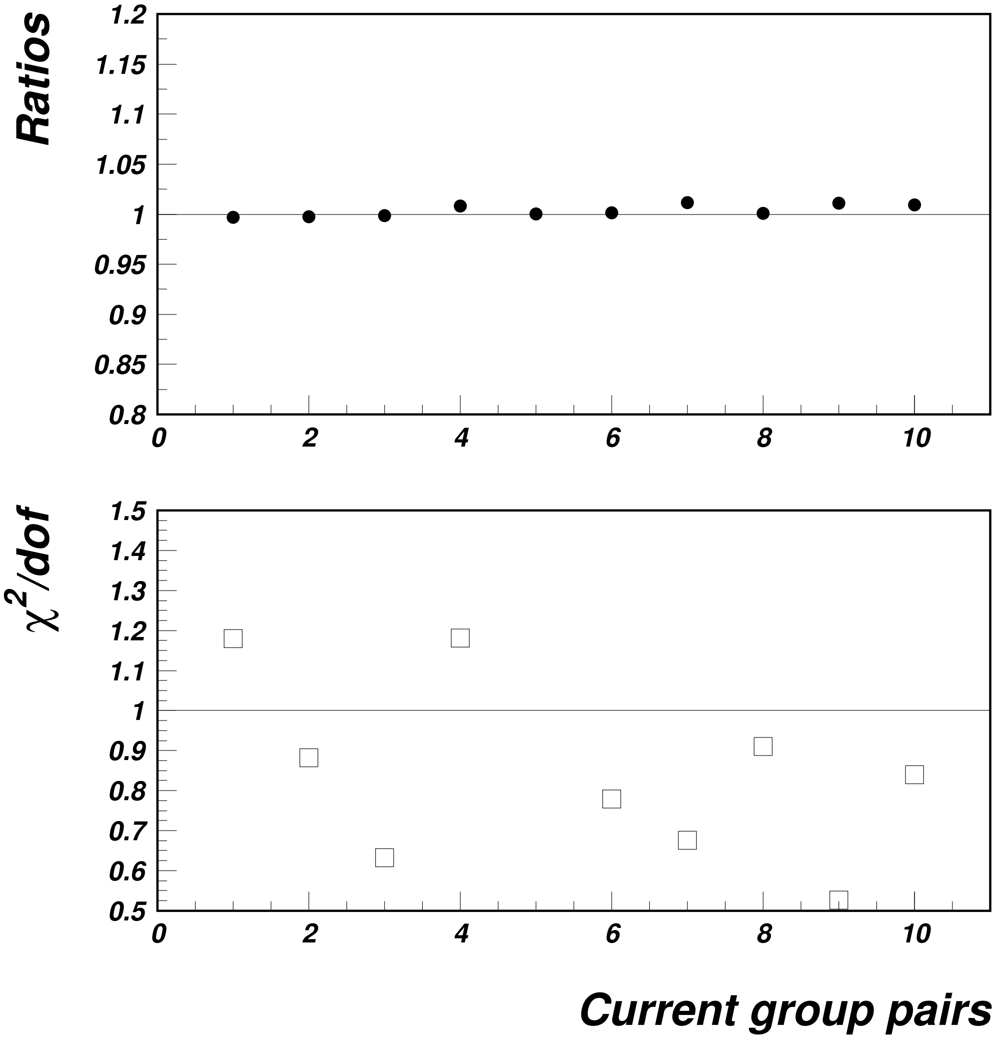

Figure 4-20: The top panel shows the results of $F_2^{^3He}/F_2^d$ ratio fits from the 10 pairs in the fill-by-fill extraction method and the χ^2/dof of the fits are shown in the bottom panel.

4.5.3 Smearing corrections

From the measured momentum and scattering angle in the experiment, we compute kinematic variables of the DIS interaction such as x and Q^2. However, the effect of the finite momentum and angular resolution of the HERMES spectrometer result in migrations or shifts of the kinematic variables. To make a correction to the F_2 ratio measurement due to possible differences or shifts of a kinematic variable, a Monte Carlo simulation using HMC is used by comparing the *generated* and *reconstructed* F_2 ratio. For this study the inclusive HMC mcDST data with 14×10^6 DIS events for ^{1}H , 28×10^6 for ^{2}H , and 12 $\times10^6$ for ^{3}He of DIS inclusive events was used.

Table 4.13 shows the average x and Q^2 values for *generated* and *reconstructed* HMC DIS events. As expected, the results at low values of x are not very different. The biggest variation occurs in the mid x ranges. The maximum deviation is 0.3%. The results of smearing corrections for F_2^n/F_2^p and $F_2^{^3He}/F_2^d$ of *generated* and *reconstructed* using HMC events are shown in table 4.14. As expected, the smearing correction of F_2^n/F_2^p is in the range of a few % throughout the entire x range. This correction is not significant since the values of F_2^n/F_2^p lie in the range of 0 to 1. Also, the change in $F_2^{^3He}/F_2^d$ is negligible. Therefore, the smearing correction results are not applied to the measured results. Instead of doing so, these corrections are quoted as a systematic uncertainty for the F_2^n/F_2^p and $F_2^{^3He}/F_2^d$ measurements.

$< x >$		Q^2	
Generated	Reconstructed	Generated	Reconstructed
0.0124	0.0124	0.5015	0.5013
0.0171	0.0171	0.6675	0.6675
0.0225	0.0225	0.8509	0.8524
0.0288	0.0287	1.0557	1.0596
0.0361	0.0361	1.2911	1.3001
0.0451	0.0451	1.5731	1.5902
0.0601	0.0601	2.0234	2.0528
0.0851	0.0850	2.7107	2.7566
0.1246	0.1244	3.6467	3.7156
0.1745	0.1744	4.6423	4.7340
0.2340	0.2338	5.6427	5.7483
0.3087	0.3085	6.7075	6.8178
0.3980	0.3977	7.8031	7.9077
0.5205	0.5198	9.1702	9.2542
0.6829	0.6816	11.4996	11.5310

Table 4.13: The average x and Q^2 values for 15 x bins using ^{1}H and ^{2}H HMC events. Here Gen is HMC generated and Rec for HMC reconstructed values.

$< x >$	$\Delta\ F_2^n/F_2^p$ (%)	$\Delta\ F_2^{^3He}/F_2^d$ (%)
0.0124	0.25	0.23
0.0171	0.95	0.27
0.0225	0.69	0.04
0.0288	0.66	0.13
0.0361	0.56	0.43
0.0451	0.83	0.50
0.0602	1.81	0.43
0.0851	0.91	0.16
0.1246	2.50	0.93
0.1745	1.41	0.07
0.2340	1.00	0.02
0.3087	0.74	0.20
0.3981	1.47	0.30
0.5205	0.35	0.41
0.6829	1.65	0.22

Table 4.14: The smearing corrections for $F_2^{^3He}/F_2^d$ and F_2^n/F_2^p using HMC inclusive DIS events. The results are quoted as a systematic uncertainty instead of a correction to the data points.

4.6 Structure function ratios

The structure function ratios F_2^n/F_2^p, $F_2^{^3He}/F_2^d$ and F_2^N/F_2^d are extracted and shown in figures 4-21, 4-22 and 4-23. F_2^n/F_2^p from the HERMES in figure 4-21 shows a quite good agreement with NMC/SLAC within given systematic uncertainties for all x bin. In figure 4-22, the HERMES $F_2^{^3He}/F_2^d$ is compared to the $F_2^{^4He}/F_2^d$ from the NMC and SLAC experiments. In figure 4-23, the HERMES F_2^N/F_2^d is also compared to the $F_2^{^{12}C}/F_2^d$ from the NMC, SLAC, and E665 experiments. The systematic errors, which are about 1 % for NMC and range from 1% at the highest x-bin to 5% (^{3}He) and 7% (^{14}N) at the lowest x-bin for HERMES, are represented by the error band at the bottom of the figures.

Considering the A-dependence of the nuclear shadowing at low x, from figure 4-22 and 4-23 it is clearly concluded that while the NMC and E665 data are in good agreement with each other, the HERMES data are significantly below the other data sets at low x. The large difference between the HERMES results and the results from NMC, SLAC and E665 is unexpected. In an effort to understand these discrepancies, the Q^2 dependence of the cross section ratio for each x bin will be discussed in the next chapter. It is seen that there is no smooth transition from the HERMES data at low Q^2 to the NMC and E665 data at higher Q^2. The discrepancy is most notable for $0.01 < x < 0.05$, as was already noted in relation to figure 4-22 and 4-23.

The only quantity which is different for HERMES and NMC at the same x and Q^2 is y (and thus ϵ), since the beam energy at the NMC (197 GeV) experiment is higher than at HERMES (27.5 GeV). One possible way that this difference in ϵ might explain the HERMES and NMC difference is if $R_A \neq R_D$. In the next chapter, a possible resolution of these different cross section ratios between the HERMES and NMC experiments will be discussed.

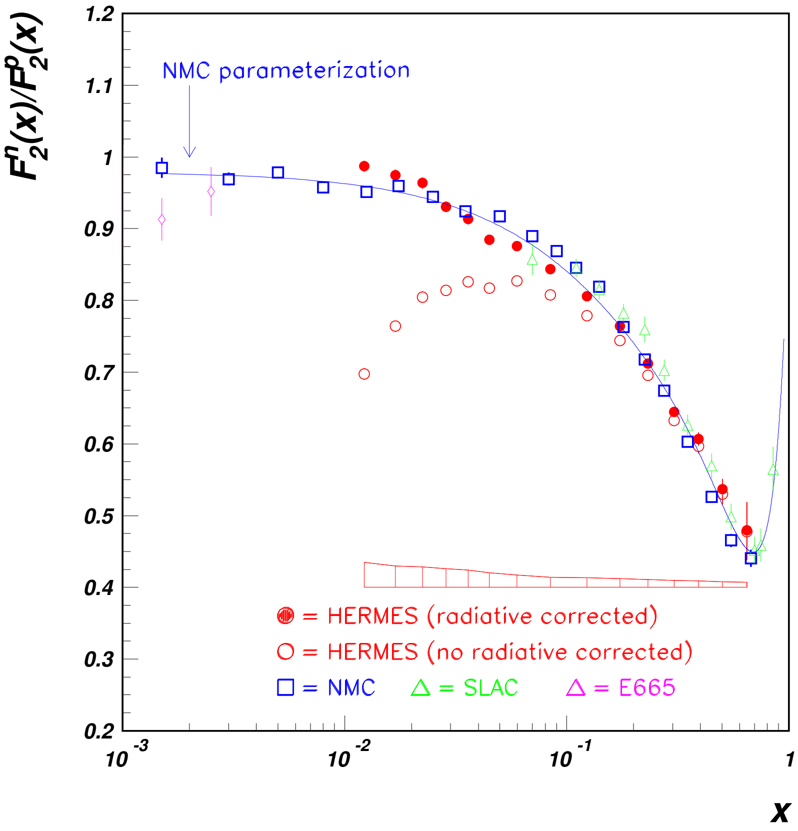

Figure 4-21: F_2^n/F_2^p from the HERMES is compared to NMC/SLAC experiments. The systematic uncertainty for F_2^n/F_2^p from the HERMES are expressed in the box graph. 1.4 % of normalization uncertainty is not included in this plot.

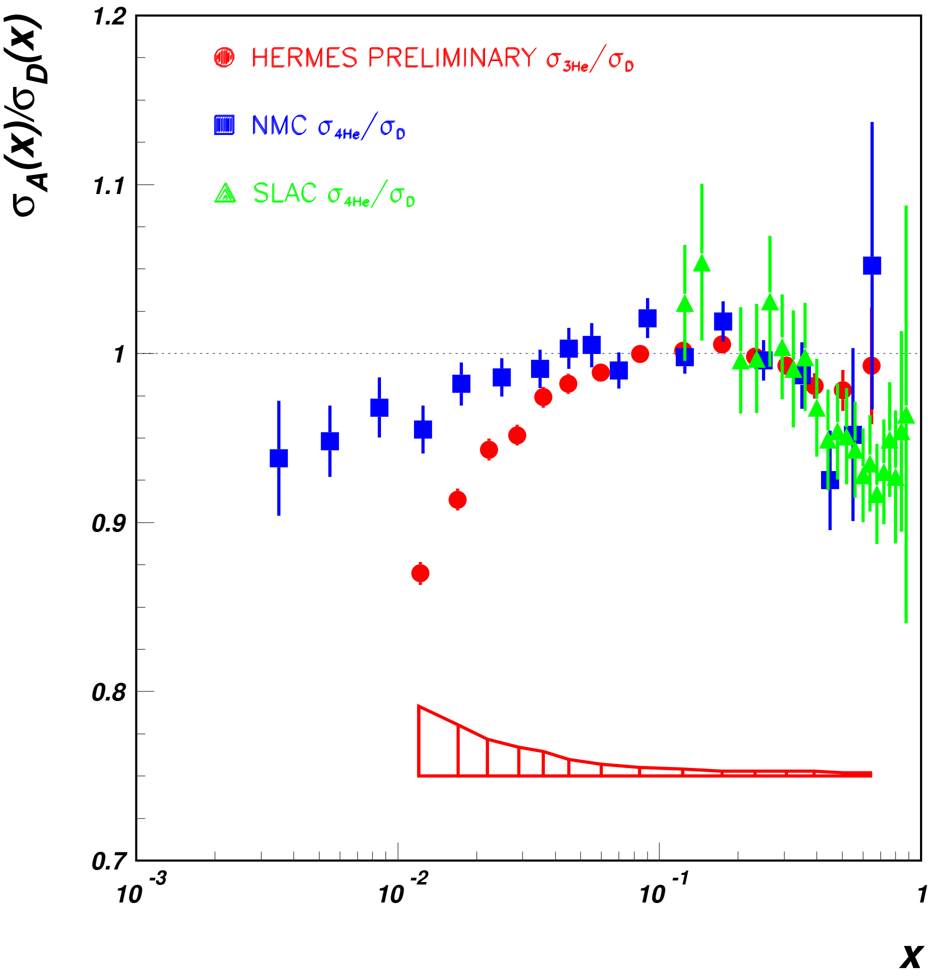

Figure 4-22: A large difference between HERMES (^{3}He) and NMC (^{4}He) for $0.01 < x < 0.1$ is observed.

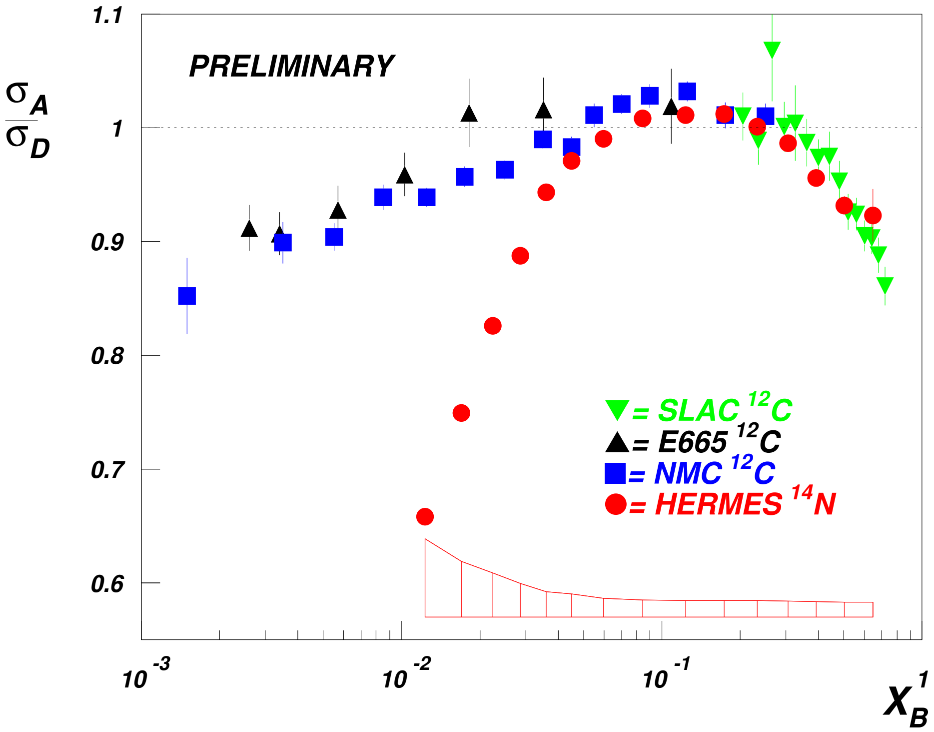

Figure 4-23: A large difference between HERMES (^{14}N) and NMC/E665 (^{12}C) data for $0.01 < x < 0.1$ is observed.

Chapter 5

The nuclear dependence of $R = \sigma_L/\sigma_T$

The cross section ratios of ^{3}He to ^{2}H and ^{14}N to ^{2}H from the HERMES data in the previous chapter show an unexpected and large shadowing effect compared to previous data from NMC , SLAC, and E665 experiments. It is worth while noticing that one major difference between the HERMES and the NMC/SLAC/E665 data is that the same x bin has a significantly different Q^2 value. For instance the average Q^2 value of the lowest x bin for the HERMES data is 0.45 GeV^2 and is 5.0 GeV^2 at the same x for the NMC experiment. The Q^2 difference results in a significantly different ϵ value at the same x bin between the HERMES and NMC/SLAC/E665 data. This difference has one important implication: If the incident beam energy is high enough, then the virtual photon polarization parameter ϵ is close to unity. Therefore, it is quite safe to consider the cross section ratios as the same as the structure function ratios. However, in case of a low energy incident beam energy, this is not always true. In this chapter, the extraction of the structure function ratios from cross section ratios is discribed using the ϵ-dependence of the cross section and the implications of this are discussed.

5.1 The cross section ratio formula

Introducing the virtual photon polarizability ϵ explicitly, the DIS cross section can be rewritten as

$$\frac{d\sigma(x,Q^2,\epsilon)}{dE'd\Omega} = \sigma_{Mott}\frac{2MxF_2(x,Q^2)}{\epsilon Q^2}[\frac{1+\epsilon R(x,Q^2)}{1+R(x,Q^2)}] \tag{5.1}$$

with R the ratio of the longitudinal and transverse virtual photon absorption cross section ($=\sigma_L/\sigma_T$), σ_{Mott} is the cross section for a point like particle, and F_2 is the structure function. The virtual photon polarization parameter ϵ can be written as

$$\epsilon = \frac{4(1-y) - \frac{Q^2}{E^2}}{4(1-y) + 2y^2 + \frac{Q^2}{E^2}}. \tag{5.2}$$

The virtual photon polarization parameter ϵ ranges from 0 to 1 and quantifies the degree of transverse polarization of the virtual photon.

Now taking the cross section ratio of deep inelastic scattering on a nuclear target with atomic mass A to deuterium D ($={}^2$H), the cross section ratio becomes

$$\frac{\sigma_A}{\sigma_D} = \frac{F_2^A}{F_2^D}\frac{(1+\epsilon R_A)(1+R_D)}{(1+R_A)(1+\epsilon R_D)}. \tag{5.3}$$

where R_A and R_D represent the ratio σ_L/σ_T for nucleus A and D. From the above equation (5.3), the cross section ratio equals the ratio of structure function ratio F_2^A/F_2^D with the two limiting conditions: $\epsilon \to 1$ and $R_A = R_D$. A difference between R_A and R_D will thus show up as an ϵ dependence of σ_A/σ_D.

5.2 Q^2-dependence of cross section ratio

The Q^2-dependence of the cross section ratios, $F_2^{^3He}/F_2^d$ and F_2^N/F_2^d , are plotted in fugures 5-1 and 5-2.

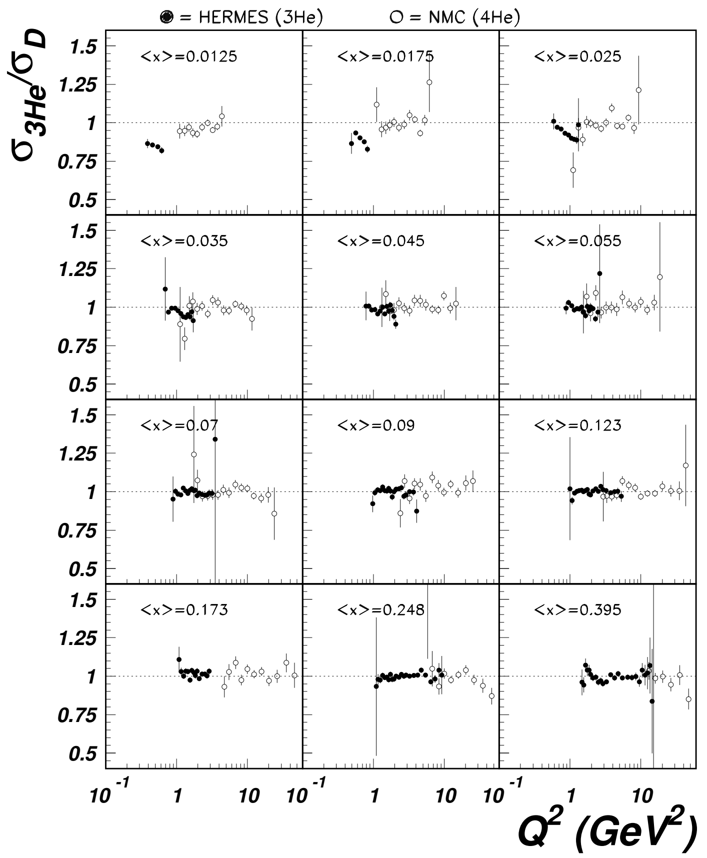

Figure 5-1: Q^2-dependence of cross section ratio is plotted for 15 x bins. The same average x has quite different Q^2 values between the HERMES and NMC data. The difference at low x increases with Q^2.

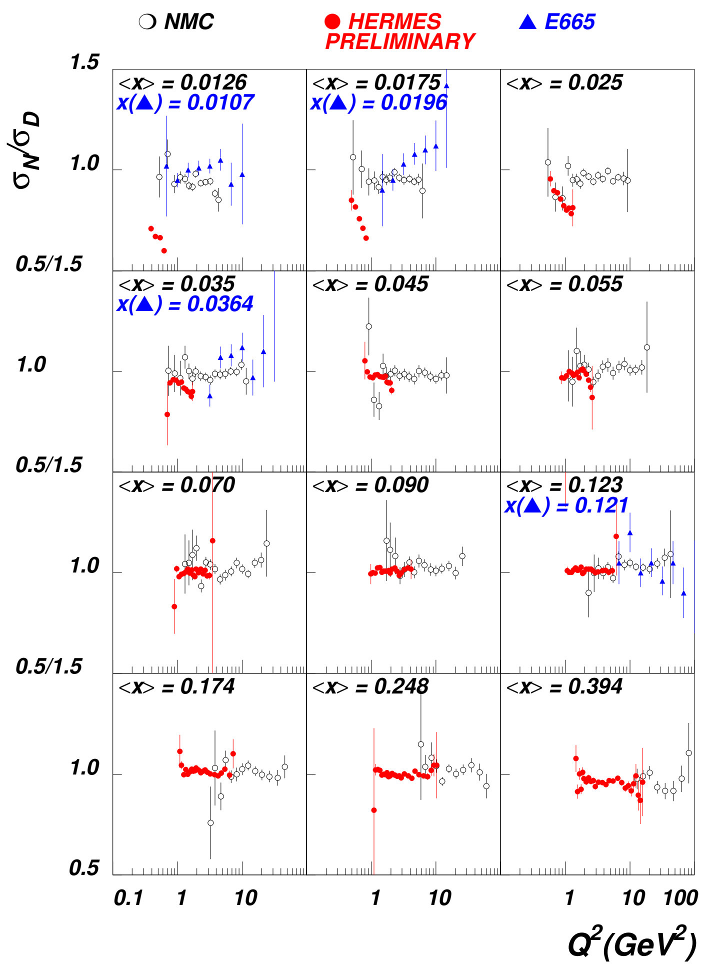

Figure 5-2: Q^2-dependence of cross section ratio is plotted for 15 x bins. The same average x has quite different Q^2 values between the HERMES and NMC/SLAC data. The difference at low x increases with Q^2.

It is seen that there is no smooth transition from the HERMES data at low Q^2 to the NMC and E665 data at higher Q^2. The discrepancy is most notable for $0.01 < x < 0.05$, as was already noted in relation to figures 4-22 and 4-23.

The only quantity which is different for HERMES and NMC at the same x and Q^2 is y (and thus ϵ), since the beam energy at the NMC (197 GeV) experiment is higher than at HERMES (27.5 GeV). One possible way that this discrepancy in ϵ might explain the HERMES and NMC difference is to assume that $R_A \neq R_D$.

5.3 Cross section ratios vs ϵ

In order to find the possible ϵ-dependence of the cross section ratios, the ϵ parameter is calculated for each event using equation (5.2) and then the cross section ratio for each x bin is plotted as a function of ϵ in figure 5-3 for ^{3}He and 5-4 for ^{14}N targets. The ϵ-dependence of the cross section ratios for ^{3}He from the HERMES experiment in figure 5-3 shows that the deviation with respect to unity decreases with increasing ϵ values. The cross section ratio of ^{14}N vs ϵ in figure 5-4 shows an increased deviation from unity and distinctive slopes at low x. This observation is in accordance with the anticipated behavior of σ_A/σ_D if $R_A \neq R_D$ as described in the former section. However, the NMC results for ^{3}He and ^{14}N show no or very little ϵ-dependence throughout the entire x region. Again, the two data sets shown in figures 5-3 and 5-4 at the same ϵ and x values correspond to different Q^2 values as seen in the Q^2-dependence plots.

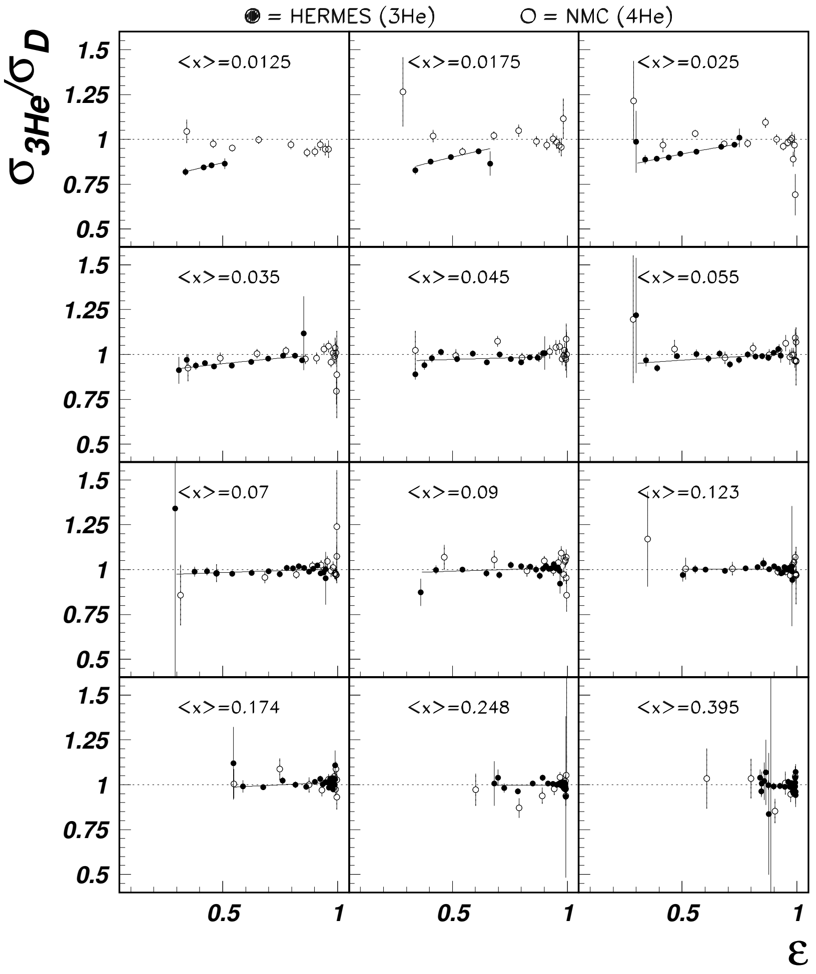

Figure 5-3: The ϵ-dependence of the cross section ratio $\sigma_{^3He}/\sigma_D$ is shown. The fit inside the plot is done by considering F_2^A/F_2^D and R_A/R_D as free parameters from equation (5.3).

5.4 Extraction of F_2^A/F_2^D and R_A/R_D

The data in the individual x bins of figure 5-3 and 5-4 have been fitted using equation (5.1). In these fits a parametrization of R_D [112] has been used while the ratio F_2^A/F_2^D and R_A/R_D have been treated as free parameters. The solid curves on the HERMES data in

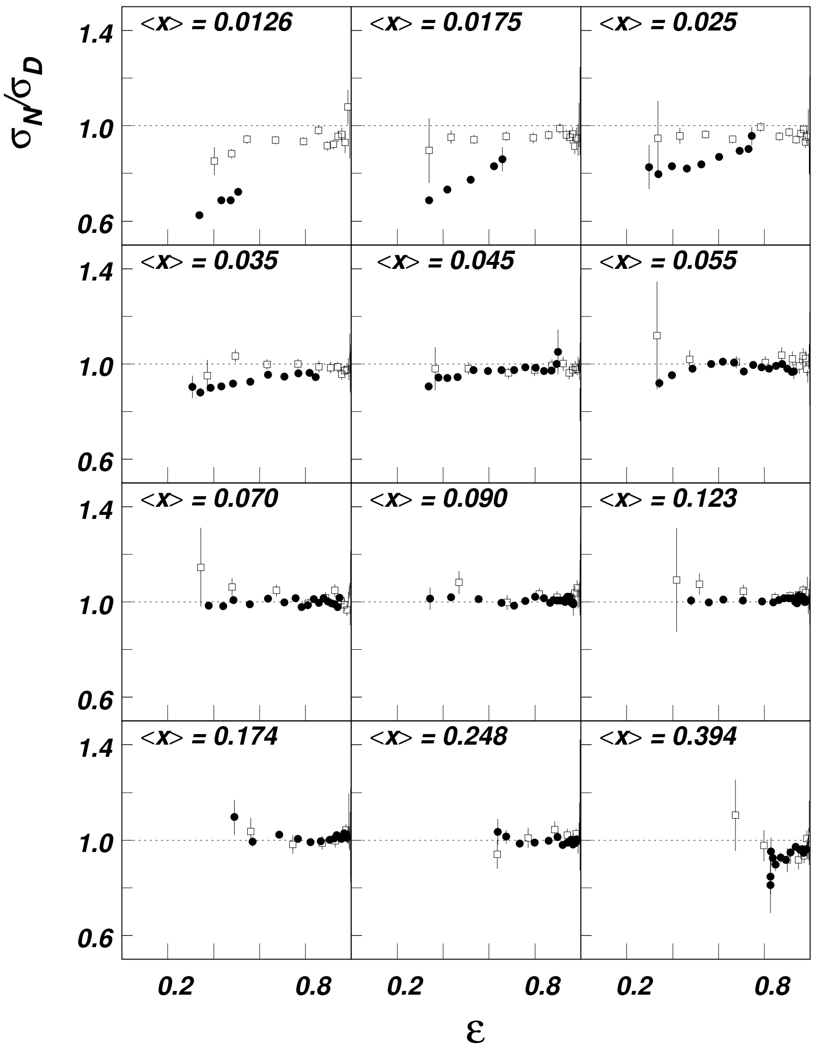

Figure 5-4: The ϵ dependence of the cross section ratio σ_N/σ_D is shown. The fit inside the plot is done by considering F_2^A/F_2^D and R_A/R_D as free parameters from equation (5.3).

figure 5-3 represent the fits. A single value of F_2^A/F_2^D and R_A/R_D has been extracted from each x bin for both the HERMES and NMC data at the average x and Q^2 values of each panel. In the fitting procedure both F_2^A/F_2^D and R_A/R_D are constant over the limited Q^2 range covered by the data in each x bin. While the Q^2 dependence of F_2^A/F_2^D is known to be very small [113, 114], the effect of a possible Q^2 dependence on extracted values of R_A/R_D has been studied separately. Assuming a linear Q^2 dependence of R_A/R_D, it has been verified that the Q^2 range covered by each x bin does not affect the average values of R_A/R_D derived from the fit.

The values of F_2^A/F_2^D extracted from the fit of the HERMES data are displayed in figure 5-5 for ^{3}He and ^{14}N target. The statistical uncertainty and the effect of the correlated error in R_A/R_D (inner error bars) are indicated separately from the total uncertainty that includes the systematic uncertainties as well (outer error bars). The solid curves in the plot represent parametrizations of F_2^A/F_2^D for A=4 and 12, determined using the NMC and SLAC data [41, 42]. The HERMES result for F_2^A/F_2^D is in good agreement with the parametrization. The uncertainties on F_2^A/F_2^D are too large to observe any systematic deviation between F_2^A/F_2^D for neighboring nuclei.

The resulting values of R_A/R_D are shown in figure 5-6. The error bars include the statistical uncertainty, the correlated error in F_2^A/F_2^D and the systematic uncertainty. Both the present results, which were obtained from the fits of the HERMES and NMC data shown in figures 5-1 and 5-2, and results derived from other sources are also displayed. The data are plotted at the average value of Q^2 for a given x bin. The values of R_A/R_D derived from the HERMES data are considerably larger than unity for $x < 0.06$ and $Q^2 < 1.5$ GeV^2. The deviation from unity is smaller for ^{3}He than for ^{14}N , as one would expect from the A dependence of F_2^A/F_2^D. The results of the fits of the NMC data for ^{4}He and ^{12}C , which were collected at higher average Q^2 values, are all consistent with unity. The present data for R_A/R_D are also compared to the results of previous studies of the A dependence of R. Existing data are usually represented in terms of $\Delta R = R_A - R_D$. The published values of ΔR [115, 113, 112] have been converted to R_A/R_D using a parametrization for R_D [112] and added in the plot. All data above $Q^2 = 1.5$ GeV^2 are seen to be consistent with unity, while for $x < 0.06$ and $Q^2 < 1.5$ GeV^2 a strong Q^2 dependence is observed. It is noted that the R_A/R_D data below $x = 0.15$ can be described by an inverse power of Q^2, independent of x. The errors associated with the two parameter fit are summarized in tables 5.1 and 5.2.

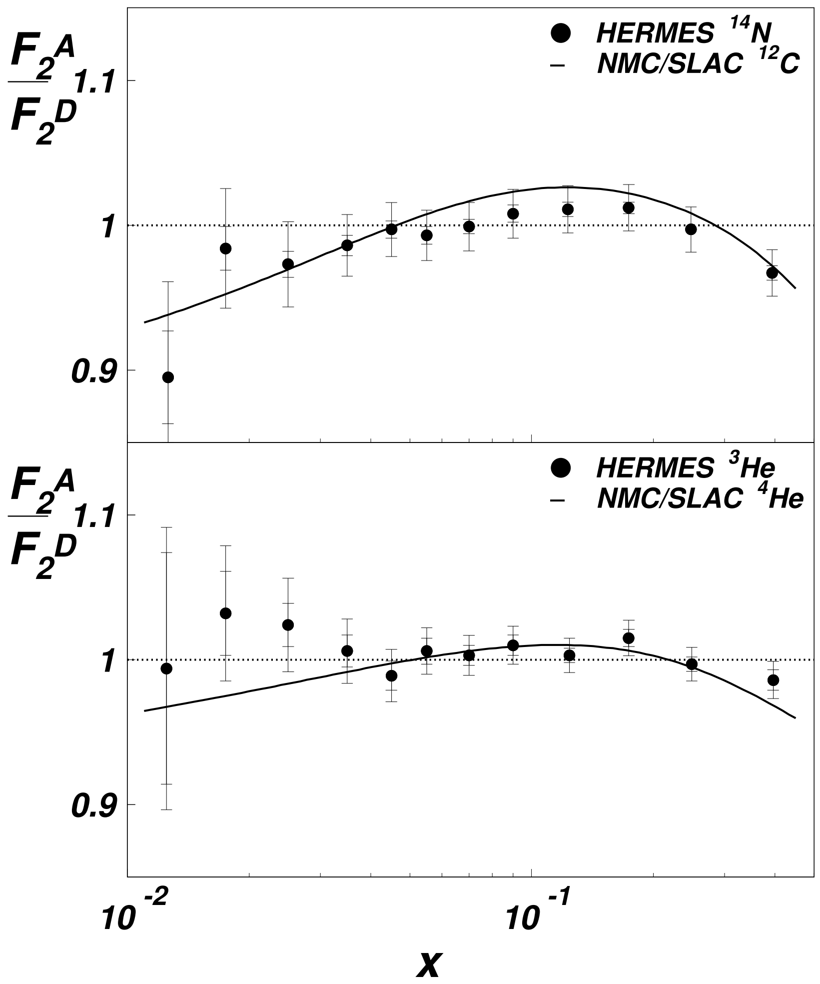

Figure 5-5: The F_2^A/F_2^D ratio as a function of x from the best fit is shown for ^{3}He and ^{14}N targets. The data are compared to parametrizations of F_2^A/F_2^D for A=4 and 12, determined using the NMC and SLAC data [41, 42]. The inner error bars include the statistical uncertainty and the correlated error in R_A/R_D. The outer error bars represent the total uncertainty including the systematic uncertainty.

i	x	Q^2	$\frac{R_{^3He}}{R_D}$	$\Delta\frac{R_{^3He}}{R_D}$		$\frac{F_2^{^3He}}{F_2^D}$	$\Delta\frac{F_2^{^3He}}{F_2^D}$	
				fit	sys		fit	sys
1	0.0125	0.498	2.60	1.09	0.23	0.994	0.080	0.056
2	0.0175	0.660	2.57	0.41	0.05	1.032	0.029	0.037
3	0.025	0.872	2.17	0.22	0.05	1.024	0.015	0.029
4	0.035	1.117	1.58	0.15	0.01	1.006	0.011	0.019
5	0.045	1.322	1.15	0.13	0.00	0.989	0.010	0.015
6	0.055	1.493	1.37	0.15	0.00	1.006	0.009	0.013
7	0.070	1.699	1.19	0.13	0.00	1.003	0.007	0.012
8	0.090	1.903	1.19	0.16	0.00	1.010	0.007	0.011
9	0.124	2.167	1.01	0.16	0.00	1.003	0.005	0.011
10	0.174	2.496	1.39	0.31	0.00	1.015	0.006	0.011
11	0.249	2.862	0.98	0.39	0.00	0.997	0.005	0.011
12	0.396	4.241	0.43	1.22	0.01	0.986	0.007	0.011

Table 5.1: For each fit parameter two errors are listed. The 'fit' error includes the effect of the statistical uncertainty in the cross section ratios and the error due to correlations between the fit parameters. The 'systematic' error includes uncertainties due to the radiative corrections and normalization error, which are summed quadratically. The later error is evaluated by determining the maximum and minimum values of the cross section ratio, which are used to extract the maximum and minimum values of the fit parameters, F_2^A/F_2^D and R_A/R_D. The deviation of the fit parameters, relative to the central value, is represented in the tables in the column "sys". The uncertainty in R_A/R_D due to the error of the R1998 [116] parametrization is smaller than 1%, and can thus be neglected compared to the other errors.

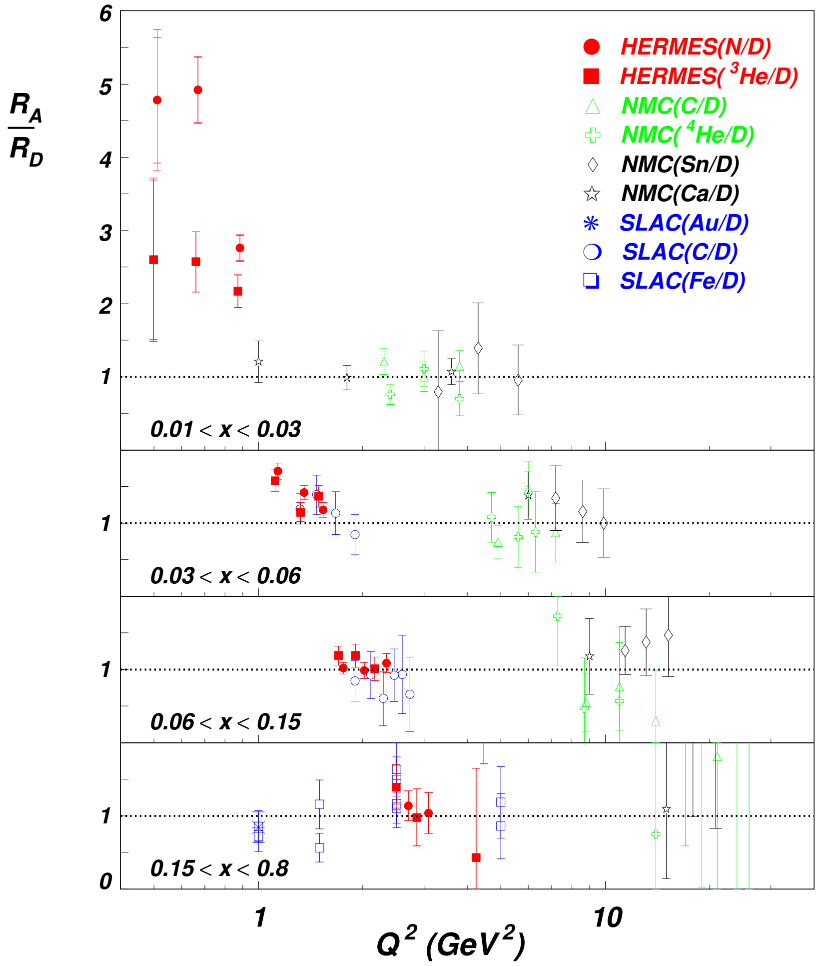

Figure 5-6: The ratio of R_A/R_D for nucleus A and ^{2}H as a function of Q^2 for four different x bins is shown. The HERMES data on ^3He and ^{14}N are represented by the solid square and circles, respectively. The open triangle and crosses have been drived from the NMC data using the same method. The other SLAC [115] and NMC data [113, 114] displayed have been derived from a measurement of $\Delta R = R_A - R_D$ taking parametrization [112] for R_D. The inner error bars included both the statistical uncertainty and correlated error in F_2^A/F_2^D. The outer error bars also include the systematic uncertainty.

i	x	Q^2	$\frac{R_{^{14}N}}{R_D}$	$\Delta\frac{R_{^{14}N}}{R_D}$		$\frac{F_2^{^{14}N}}{F_2^D}$	$\Delta\frac{F_2^{^{14}N}}{F_2^D}$	
				fit	sys		fit	sys
1	0.0125	0.500	4.78	0.86	0.44	0.895	0.032	0.058
2	0.0175	0.669	4.92	0.44	0.13	0.984	0.015	0.038
3	0.025	0.885	2.76	0.17	0.07	0.973	0.009	0.028
4	0.035	1.138	1.71	0.11	0.01	0.986	0.007	0.020
5	0.045	1.353	1.42	0.10	0.00	0.997	0.006	0.018
6	0.055	1.534	1.18	0.10	0.00	0.993	0.006	0.016
7	0.070	1.758	1.02	0.08	0.00	0.999	0.005	0.016
8	0.090	2.018	0.99	0.11	0.00	1.008	0.006	0.016
9	0.123	2.341	1.09	0.13	0.00	1.011	0.005	0.016
10	0.174	2.702	1.14	0.20	0.00	1.012	0.004	0.016
11	0.248	3.096	1.04	0.28	0.00	0.997	0.003	0.015
12	0.394	4.469	3.14	1.43	0.02	0.967	0.005	0.015

Table 5.2: For each fit parameter two errors are listed. The 'fit' error includes the effect of the statistical uncertainty in the cross section ratios and the error due to correlations between the fit parameters. The 'systematic' error includes uncertainties due to the radiative corrections and normalization error, which are summed quadratically. The later error is evaluated by determining the maximum and minimum values of the cross section ratio, which are used to extract the maximum and minimum values of the fit parameters, F_2^A/F_2^D and R_A/R_D. The deviation of the fit parameters, relative to the central value, is represented in the tables in the column "sys". The uncertainty in R_A/R_D due to the error of the R1998 [116] parametrization is smaller than 1%, and can thus be neglected compared to the other errors.

Chapter 6

Summary

Deep-inelastic scattering from unpolarized ^{2}H, ^{3}He and ^{14}N gas targets has been measured by the HERMES experiment at DESY. The ratios of the inclusive nuclear cross sections with respect to the deuterium cross section have been determined in the x range of $0.013 < x < 0.7$ with the average Q^2 varying between 0.5 and 7 GeV^2. The data are compared to existing measurements by NMC and E665 and are found to be substantially different for x values below $x = 0.1$. As the experiments were performed at largely different incident lepton energies, the cross section ratios are measured for different values of the virtual photon polarization parameter ϵ. The observed difference in the cross section ratios is thus attributed to a large A-dependence of the longitudinal structure function at low x and low Q^2 [117].

Possible mechanisms that give rise to an enhancement of R_A with respect to R_D at low Q^2 and x are constrained by the present data to not significantly change the ratio of the structure functions F_2^A/F_2^D. Since F_2^A and R_A depend differently on the longitudinal and transverse DIS cross sections, the different effects of the nuclear medium on σ_L and σ_T can be distinguished. In fact, both an enhancement of the longitudinal response and a corresponding reduction of the transverse response are needed to explain the present data. These results appearing at low Q^2 and low x seem to indicate a novel and significant shadowing effect not included in current theoretical models. Possible shadowing differences between σ_L and σ_T have been discussed in references [118, 119]. The quoted enhancement of R_A with repect to R_D does not exceed 50% [119]. However, these studies did not cover the kinematics of the present experiment. It is noted that a satisfactory description of the HERMES results should be also consistent with the real photon data, which show less shadowing ($\sigma_T^A/\sigma_T^D = 0.77(5)$) than the virtual photon data at low Q^2 [120, 121, 122, 123, 124].

The steep Q^2 dependence of the R_A/R_D at low Q^2 also suggests a possible higher twist effect [125], i.e. strong quark-gluon correlations that are enhanced in the nuclear environment [126]. This conclusion is supported by the fact that leading twist effects are estimated to be much smaller than the observed enhancement of R_A/R_D [127, 128]. The size of twist-4 effects in nuclei has been estimated by Luo, Qui, and Sterman [129] for dijet photoproduction. They find sizable enhancement factors of order 100 % that scale as $A^{1/3}$.

Appendix A

Unpolarized target density

The primary purpose of the HERMES unpolarized gas feed system (UGFS) is to flow pure gases at a constant rate into the target cell with the desired target density. To meet the demand, the gas flow should be controlled, which could be done in many ways. The HERMES unpolarized gas feed system has used a diaphragm as a flow limiter for this purpose. This has been operated reliably during the course of data taking from 1995 to 2000. In this appendix, the calibration of the conductance of the diaphragm and target density calculations are described.

A.1 Unpolarized gas feed system

Figure A-1 shows the schematic layout of the unpolarized gas feed system. The pressures in each gas bottle were kept under 50 bar for ^{1}H and ^{2}H and 10 bar for ^{3}He and located in the fire-proof cabinet under the target platform. The gas bottles of ^{1}H, ^{2}H, and ^{3}He (or ^{14}N) were connected to the gas manifold, which is not shown in figure A-1, through gas regulators to the remote controlled and air actuated solenoid valves. The gas manifold has sufficient volume to act as a buffer so that the input pressure to the thermo-valve(UDV 135 Valve from Balzers) could be constant. The purpose of the thermo-valve is to provide constant input pressure before the diaphragm. The gas flow control is achieved by a diaphragm after

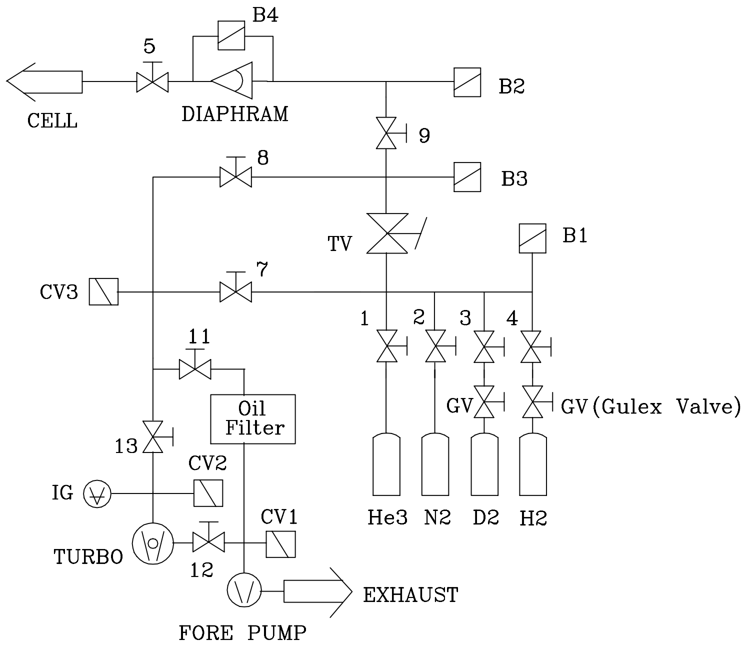

Figure A-1: Schematic diagram of unpolarized gas feed system as configured for 96 running.

the thermo-valve. The diaphragm is made from a solid copper block sandwiched between two CF45 frange: 9.5 mm in thickness and has a hole of 0.51mm in diameter. The pressure drop across the diaphragm is measured by the differential baratron (B4). The gas flow or *throughput* is then given by $Q = C_d \Delta P$. Here C_d is the conductance of the diaphragm and ΔP is the pressure drop as read from B4. The constant flow rate with a nominal target density at the target cell is controlled and limited by the smallest conductance of this diaphragm.

A.2 Calibration of the diaphragm

The gas in a vacuum system can be in a viscous state, in a molecular state or in a state which is intermediate between these two. The mean free path of the gas molecule is very small at atmospheric pressure so that the flow of the gas is limited by viscosity. At low temperature where the mean free path of molecules is similar to the dimensions of the vacuum enclosure, the flow of the gas is governed by viscosity as well as by molecular phenomena. This is the case of intermediate flow. At low pressures where the mean free path is much larger than the dimensions of the vacuum enclosure, the flow is molecular. This boundary is described by the Knudsen number [130] which is the ratio D/λ, between the diameter of the pipe, D, and the mean free path, λ. In terms of this number, the ranges can be defined as [130]

$$\begin{aligned} D/\lambda > 110 &\quad \text{Viscous flow} \\ 1 < D/\lambda < 110 &\quad \text{Intermediate flow} \\ D/\lambda < 1 &\quad \text{Molecular flow} \end{aligned} \tag{A.1}$$

where λ is $2.33 \times 10^{-20} T/(\xi P)$ in units of cm by using ξ for molecular diameter in cm, T in ^oK and P in Torr. In the case of ^{1}H, ^{2}H, and ^{3}He gas, the flow regime inside the diaphragm is in the intermediate regime. Therefore, the exponential pressure decay from a given volume can provide a way of measuring the conductance of the diaphragm.

Firure A-2 shows the schematic layout of the diaphragm conductance calibration set up. Air has been used to measure the pressure decay with respect to time from the calibration set-up. Starting with closed valves 1, 2, 3, and 4, the initial pressure was to set to be around 10 torr with baratron B1 and B2. Then, with valve number 4 open, the pressure decay was observed using baratron B2. The pressure decay as a function of time for three different measurements was fit to the relation:

$$\begin{aligned} P(t) &= P_0 e^{-\frac{C_d}{V} t} \\ &= P_0 e^{-\frac{C_m + C_v P(t)}{V} t} \end{aligned} \tag{A.2}$$

where C_m is the molecular conductance, C_v the viscosity conductance of the diaphragm, P_0 the initial pressure, and V the effective volume. The measurements are shown in figure A-3.

Using the best fit to each measurement, the molecular conductance C_m in units of liters/sec and the viscosity conductance C_v in liters/sec/Torr were determined as 0.0418 ± 0.0076(stat)

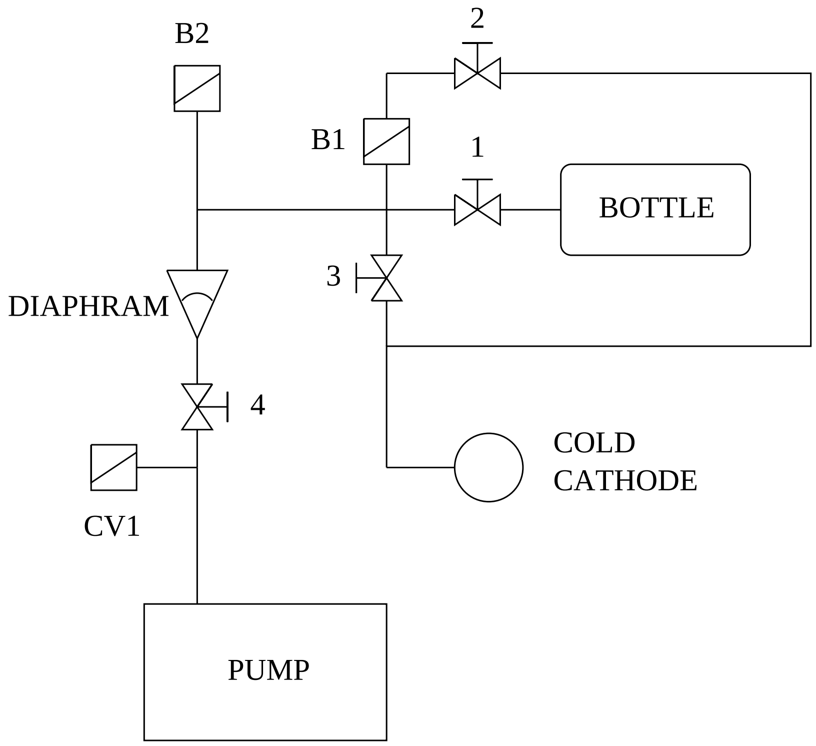

Figure A-2: The schematic diagram of the calibration measurement set up of the diaphragm conductance.

and 0.0147(stat) $\pm$ 0.0043, respectively. Here the statistical uncertainty is determined from the fitting errors. The effective volume, V, between the diaphragm and the other three valves is 141.0 cm^3. Since the conductance C_m and C_v are measured using air, conversion factors [130] were applied in order to compare with the measured conductances C_m=0.0161 and C_v=0.003) using ^{3}He in 95. The comparison berween the conductance from using ^{3}He in 95 and the current measurement is shown as a function of the input pressure in table A.1.

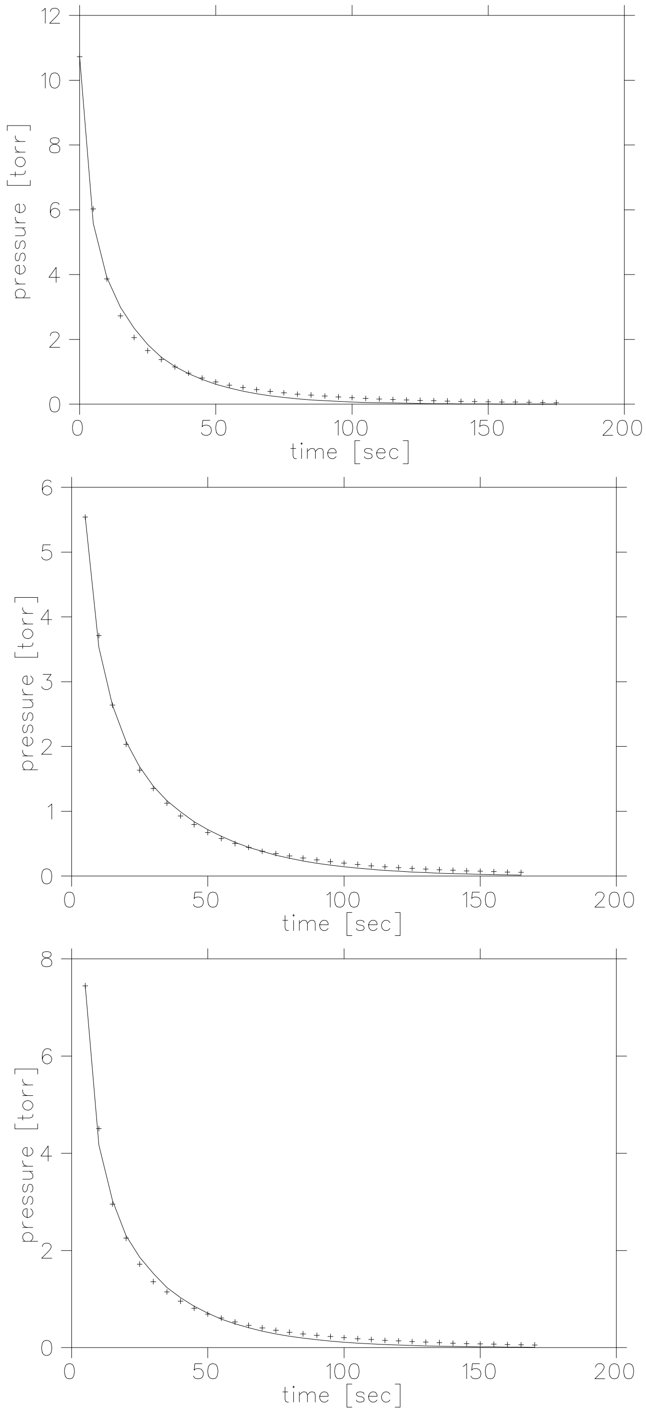

Figure A-3: The pressure decay measurements with repect to time.

p(torr)	$C_d(95)$	$C_d(96)$	$\Delta C_d(96)$
0.5	0.0176	0.0192	0.0038
1.0	0.0191	0.0203	0.0038
1.5	0.0206	0.0214	0.0039
2.0	0.0221	0.0225	0.0040
2.5	0.0236	0.0236	0.0041
3.0	0.0251	0.0247	0.0043
3.5	0.0266	0.0258	0.0045
4.0	0.0281	0.0269	0.0047
4.5	0.0296	0.0280	0.0049
5.0	0.0311	0.0291	0.0051

Table A.1: The comparison of conductances between $C_d(95)$ and $C_d(96)$. The $C_d(96)$ is converted to ^{3}He from air. Here the total uncertainties in $\Delta C_d(96)$ are calculated as a quadratic sum of statistical and 10% uncertainty from the effective volume measurement.

A.3 Calculation of target density

During the course of data taking in 95 through 99 using the UGFS, the nominal values of the conductances of the diaphragm have been 0.0161 liters/sec for C_m and 0.0030 liters/sec/Torr for C_v. Here the target density calculation is described using these values of C_m and C_v.

To convert the measured conductance C_m and C_v from ^{3}He, the Sutherland's constant and mean free path were introduced to take account of the viscosities for different gases[130]. Table A.2 summarizes the conversion factors used to determine conductances of different gases from measurement of C_m and C_v using ^{3}He gas. Using those numbers, the conductance of the diaphragm for a gas of mass number M is given as [130]:

$$C = C_m\sqrt{\frac{M_0}{M}} + C_v\frac{1+S/T_{room}}{1+S_0/T_{room}}\sqrt{\frac{M_0}{M}}\frac{\lambda_0}{\lambda}\Delta P \tag{A.3}$$

where M_0 is 3 for the mass number, S_0 the Suthrland's constant [130], and λ_0 for the mean free path of ^3He. The flow rate f, which is the product of the conductance (C_d) and pressure drop (ΔP) across the diaphragm is

$$\begin{aligned} f &= C\sqrt{\frac{T_d}{M}}\Delta P \\ &= C\sqrt{\frac{T_d}{M}}\Delta P\frac{N_A}{V_0 Y} \end{aligned} \tag{A.4}$$

where T_d is the temperature of the diaphragm; N_A is 6.02×10^{23} molecules/mole; V_0 is 22.4 liter/mole from standard volume; Y is 1.31×10^{-3} Torr/atm as the conversion factor from atm to Torr. As a result, the first expression in equation (A.4) is written in units of Torr-liter/sec and the second in equation (A.4) is given as molecules/sec. Finally, using the target cell conductance [71] C_{cell}, the target density (n) formula in units of nucleons/cm^2 is

$$\begin{aligned} C_{cell} &= 12760\sqrt{\frac{T_{cell}}{T_{room}}}\sqrt{\frac{M_0}{M}} \\ n &= 0.5LfM/C_{cell}. \end{aligned} \tag{A.5}$$

Here the length of the cell (L) is 40 cm. Tables A.3, A.4, A.5, and A.6 summarize calculations of the conductance, flow rate and target density by assuming a 100 ^{o}K target cell. The total uncertainties in conductance (C_d) and flow rate (f) calculation are quoted as 10%. The uncertainty in the target density(n) is then 22.4% by assigning 20% uncertainty to the target cell conductance.

conversion factor	^{1}H	^{2}H	^{14}N	^{3}He
Sutherland's constant (S)	76.0	76.0	112.0	79.0
mean free path λ (cm)	0.01056	0.01056	0.0061	0.016

Table A.2: The conversion factors for different gases [130].

ΔP (Torr)	C_d(liter/sec)	f (molecule/sec)	n (nucleons/cm^2)
0.10	2.020E-02	7.150E+16	3.208E+14
0.20	2.075E-02	1.469E+17	6.592E+14
0.30	2.131E-02	2.263E+17	1.015E+15
0.40	2.186E-02	3.096E+17	1.389E+15
0.50	2.242E-02	3.968E+17	1.780E+15
0.60	2.298E-02	4.880E+17	2.190E+15
0.70	2.353E-02	5.831E+17	2.616E+15
0.80	2.409E-02	6.822E+17	3.061E+15
0.90	2.465E-02	7.852E+17	3.523E+15
1.00	2.520E-02	8.921E+17	4.003E+15

Table A.3: The flow rate (molecules/sec) and target density (nucleons/cm^2) calculations as a function of ΔP for ^{1}H are summarized assuming a 100 ^{o}K target cell.

ΔP (Torr)	C_d(liter/sec)	f (molecules/sec)	n (nucleons/cm^2)
0.10	1.434E-02	5.076E+16	6.365E+14
0.20	1.473E-02	1.043E+17	1.308E+15
0.30	1.513E-02	1.607E+17	2.014E+15
0.40	1.552E-02	2.198E+17	2.756E+15
0.50	1.592E-02	2.817E+17	3.533E+15
0.60	1.631E-02	3.465E+17	4.344E+15
0.70	1.671E-02	4.140E+17	5.191E+15
0.80	1.710E-02	4.843E+17	6.073E+15
0.90	1.750E-02	5.574E+17	6.990E+15
1.00	1.789E-02	6.333E+17	7.942E+15

Table A.4: The flow rate (molecules/sec) and target density (nucleons/cm^2) calculations as a function of ΔP for ^{2}H are summarized assuming a 100 ^{o}K target cell.

ΔP (Torr)	C_d(liter/sec)	f (molecules/sec)	n (nucleons/cm^2)
0.10	1.640E-02	5.806E+16	4.729E+14
0.20	1.670E-02	1.183E+17	9.631E+14
0.30	1.700E-02	1.806E+17	1.471E+15
0.40	1.730E-02	2.450E+17	1.996E+15
0.50	1.760E-02	3.116E+17	2.538E+15
0.60	1.791E-02	3.803E+17	3.097E+15
0.70	1.821E-02	4.512E+17	3.674E+15
0.80	1.851E-02	5.241E+17	4.269E+15
0.90	1.881E-02	5.992E+17	4.880E+15
1.00	1.911E-02	6.765E+17	5.509E+15

Table A.5: The flow rate (molecules/sec) and target density (nucleons/cm^2) calculations as a function of ΔP for ^{3}He are summarized assuming a 100 ^{o}K target cell.

ΔP (Torr)	C_d(liter/sec)	f (molecules/sec)	n (nucleons/cm^2)
0.10	5.325E-03	1.885E+16	4.382E+15
0.20	5.382E-03	3.810E+16	8.858E+15
0.30	5.439E-03	5.776E+16	1.343E+16
0.40	5.496E-03	7.782E+16	1.809E+16
0.50	5.553E-03	9.828E+16	2.285E+16
0.60	5.609E-03	1.191E+17	2.770E+16
0.70	5.666E-03	1.404E+17	3.264E+16
0.80	5.723E-03	1.621E+17	3.768E+16
0.90	5.780E-03	1.842E+17	4.281E+16
1.00	5.837E-03	2.066E+17	4.804E+16

Table A.6: The flow rate (molecules/sec) and target density (nucleons/cm^2) calculations as a function of ΔP for ^{14}N are summarized assuming a 100 ^{o}K target cell.

Appendix B

y-scaling method in TERAD

A description of radiative corrections in the one photon exchange cross section, $\sigma_{1\gamma}$, in deep inelastic scattering(DIS) is well known and described in references [93, 94, 95]. The corrections apart from nuclear effects are very reliable. However, the contribution from the quasielastic scattering process has been studied and the resulting uncertainty is not negligible.

The radiative tail from quasielastic scattering inside TERAD and POLRAD is calculated using a suppression factor for ^3He and ^{14}N. The differential scross section, $d\sigma/d\Omega$, is evaluated at approximately the quasielastic peak position ($\nu_0 = Q^2/2M$) and then the nucleon momentum distribution inside the nucleus is applied in terms of suppression factors calculated in the Fermi gas model. The detailed description of TERAD was well given in reference [131]. The structure functions can now be written for ^3He using electric(magnetic) suppression factors $S_E(S_M)$ as

$$\begin{aligned} W_1 &= \tau(G_{M,n}^2 + 2G_{M,p}^2)S_M \\ W_2 &= \frac{\tau(G_{M,n}^2 + G_{M,p}^2)S_M + (G_{E,n}^2 + G_{E,p}^2)S_E}{1+\tau} \end{aligned} \tag{B.1}$$

where $\tau = Q^2/4M^2$. The differential cross section for quasielastic scattering is then

$$\frac{d\sigma}{d\Omega} = \sigma_{mott}[W_2(Q^2) + 2\tan^2(\frac{\theta}{2})W_1(Q^2)]. \tag{B.2}$$

Another possibility is to use the experimental scaling function $F(y)$. High quality quasielastic data for various nuclei exist with $F(y)$ extracted for each nucleus [132, 133]. Thefore, the concept of y-scaling is briefly introduced in this appendix and extended to TERAD and POLRAD to calculate radiative tails from quasielastic scattering. The radiative tail from the quasielastic peak as a contribution to a total correction to unpolarized inclusive DIS events in the HERMES experiment is reconsidered using the y-scaling model.

B.1 Quasielastic Scattering

In inclusive scattering (e,e$^{'}$), the final state of the nucleus is unobserved: only the scattered electron is detected and the meaured cross section is an integral over all possible final states. It is well known that if Lorentz covariance, parity violation and current conservation is assumed, the (e,e$^{'}$) cross section depends only on two independent structure structure function: the longitudinal, R_L, arising from the interaction with the charge of the target, and the transverse, R_T, resulting from the interaction with magnetism and convection currents in the target. When using unpolarized targets and electrons, the response functions depend on two independent variables, $|\vec{q}|$ and ν. The inclusive cross section may be written in the form [132]

$$\frac{d^2\sigma}{d\Omega d\nu} = \sigma_{mott}[v_L R_L + v_T R_T] \tag{B.3}$$

with $v_L = Q^4/|\vec{q}|^4$, $v_T = \frac{1}{2}(|Q^2|/|\vec{q}|^2) - \tan^2(\frac{\theta}{2})$ and $\sigma_{mott} = \alpha^2\cos^2(\frac{\theta}{2})/4E^2\tan^4(\frac{\theta}{2})$. Here the relation between longitudinal (R_L) and transverse response (R_T) functions and the structure function W_1 and W_2 is

$$\begin{aligned} W_1(Q^2,\nu) &= \frac{1}{2}R_T \\ W_2(Q^2,\nu) &= \frac{Q^4}{|\vec{q}|^4}R_L + \frac{1}{2}\frac{|Q^2|}{|\vec{q}|^2}R_T. \end{aligned} \tag{B.4}$$

B.1.1 Scaling function F(y)

The experimental scaling function $F^{exp}(\mathrm{y},|\vec{q}|)$ is defined as follows [133, 111]:

$$F^{exp}(y,|\vec{q}|) = \frac{\sigma_2(y,|\vec{q}|)}{[Z\sigma_{ep} + N\sigma_{en}]}K(y,|\vec{q}|) \tag{B.5}$$

where $\sigma_2 = d^2\sigma/d\Omega dE_2$, σ_{eN}=$d^2\sigma/d\Omega$ is the off-shell electron-nucleon cross section with $N = p,\ n$ and the kinematic factor $K(y,q) = |\vec{q}|/[M_N^2 + (|\vec{q}| + y)^2]$. The scaling variable y is given by the solution of the following equation:

$$\nu + M_A = [M_N^2 + (|\vec{q}| + y)^2]^{1/2} + [M_A^2 + y^2] \tag{B.6}$$

which represents the principle of energy conservation corresponding to the scattering of the virtual photon by a nucleon having the minimum values of the momentum and removal energy, $|y| = k_{min}(|\vec{q}|,\nu,E_{min})$. At high momentum transfer the inclusive cross section σ_2 $= d^2\sigma/d\Omega dE_2$ factorizes to a good approximation and one can define the theoretical scaling function as [132]

$$F^{th}(y,|\vec{q}|) = 2\pi\int_{E_{min}}^{E_{max}} dE \int_{E_{min}}^{E_{max}} kP(k,E)dk, \tag{B.7}$$

where, for ease of presentation, we have defined for the present section $|p| = k$. In the asymptotic limit of $|\vec{q}| \longrightarrow \infty$ at fixed y, F^{th} scales in y and becomes the asymptotic scaling function:

$$F^{th}(y) = 2\pi\int_{E_{min}}^{\infty} dE \int_{|y-(E-E_{min})|}^{\infty} kP(k,E)dk. \tag{B.8}$$

Therefore, the knowledge of the experiment asymptotic scaling function $F_{exp}(y)$ which is the q independent quantity with $\sigma_2 = \sigma_2^{exp}$ in the region of negative values of y would allow one to obtain the nucleon momentum distribution.

B.1.2 Off-shell extrapolation and current conservation prescription

There are various prescriptions to take account of the off-shell nature of the nucleon inside the nucleus. Here, we take the prescription of reference [134]. In this prescription the bound nucleon interacting with the virtual photon is considered to be on-shell and current conservation is enforced. Thus, kinematic variables are defined as follows:

$$\begin{aligned} p \equiv \bar{p} &= ((M_N^2 + \vec{p}^2)^{1/2}, \vec{p}) \\ \widetilde{Q}^2 = \bar{Q}^2 &= -\bar{q}^2 = \vec{q}^2 - \bar{\nu}^2 \\ \bar{\nu} &= \nu - (M_N^2 + \vec{p}^2)^{1/2} + M_A - ((M_{A-1}^{*2} + \vec{p}^2)^{1/2} \\ \widetilde{W}^2 &= (\bar{p} + \bar{q})^2 = (p+q)^2 \\ \bar{W}_{1(2)}^{N,off}(\widetilde{Q}^2, \widetilde{W}, p^2) &= W_{1(2)}^{N,on}(\bar{Q}^2, \widetilde{W}). \end{aligned} \tag{B.9}$$

It is worth while to notice that three prescriptions [133] have in common following features: (i) The off-shell nucleon structure functions do not include dynamical modifications and, therefore, they are assumed to have the same form as the free ones. (ii) Both the invariant mass, $\widetilde{W}$, and the component $p_{\|}^2 = (\vec{p} \cdot \vec{q})^2 / |\vec{q}|^2$ of the off-shell nucleon are the same so that the mapping of the off-shell to the on-shell structures is carried out unambiguously in all prescriptioins.

Using the equation (B.4) upto (B.7), the electron-nucleon cross section for scattering by an off-shell nucleon with momentum p now becomes [134]

$$\sigma_{eN} = \frac{\sigma_{mott}}{E_p E_{p'}} [v_L \widetilde{R}_L^N + v_T \widetilde{R}_T^N] \tag{B.10}$$

where

$$\begin{aligned}\widetilde{R}_L^N &= \frac{(E_p + E_{p'})^2}{4}(F_1^2 + \bar{\tau}\kappa_2 F_2^2) - \frac{|\vec{q}|^2}{4}(F_1 + \kappa F_2)^2 \\ \widetilde{R}_T^N &= p_\perp^2 (F_1^2 + \bar{\tau}\kappa_2 F_2^2) + \frac{\bar{Q}^2}{2}(F_1 + \kappa F_2)^2 \\ p_\perp^2 &= \vec{p}^2 - p_\|^2,\ E_p = p_0,\ E_{p'} = (M_N^2 + (\vec{p} + \vec{q})^2)^{1/2}\end{aligned} \tag{B.11}$$

and where the form factors F_1 and F_2 are evaluted at $\widetilde{Q}^2 = Q^2$ and $\widetilde{\tau} = \bar{Q}^2/4M_N^2$.

Now using $F(y)$ and K with σ_{eN}, the double differential cross section, we have the following:

$$\frac{d^2\sigma}{d\Omega dE_2} = \sigma_{mott}\frac{F(y)K}{E_p E_{p'}}[v_L(Z\widetilde{R}_L^p + N\widetilde{R}_L^n) + v_T(Z\widetilde{R}_T^p + N\widetilde{R}_T^n)]. \tag{B.12}$$

For a given Q^2 and ν, using the Rosenbluth separation by dividing the equation above by $\sigma_{mott}v_L$, one can extract W_1 from the slope and W_2 from the intercept. The response functions now become

$$\begin{aligned}R_L &= \frac{F(y)K}{E_p E_{p'}}(Z\widetilde{R}_L^p + N\widetilde{R}_L^n) \\ R_T &= \frac{F(y)K}{E_p E_{p'}}(Z\widetilde{R}_T^p + N\widetilde{R}_T^n).\end{aligned} \tag{B.13}$$

Therefore, the double differential scross section becomes

$$\frac{d^2\sigma}{d\Omega d\nu} = \sigma_{mott}[W_2(Q^2,\nu) + 2\tan^2(\frac{\theta}{2})W_1(Q^2,\nu)]. \tag{B.14}$$

B.2 Experimental scaling function $F(y)$

The inclusive cross section for the process $A(e,e')$ at various kinematics from SLAC and Bates has been reported. Using current world experimental data, the parametrization of the experimental scaling functoin $F(y)$ was extracted by means of a best fit [133]. Figure B-1 shows the experimental scaling scaling $F(y)$ for ^3He and ^{12}C. Since there is no data on ^{14}N,

^{12}C has been used for our study. One can make correction for ^{12}C using Fermi momenta of ^{12}C and ^{14}N.

Figure B-2 clearly shows the usefulness of $F(y)$ to extract the quasielastic contribution from ^{3}He(e,e$'$) reaction data from SLAC [133]. The double differential cross section at an incident electron energy 10.594 GeV and a scattering angle of $8^o$is plotted as function of energy transfer ν with $< Q^2 >$=2.0 GeV^2. The quasielastic peak is located around 1.1 GeV of ν and the double differential cross section is lower than the data because of the DIS contribution at high momentum transfer.

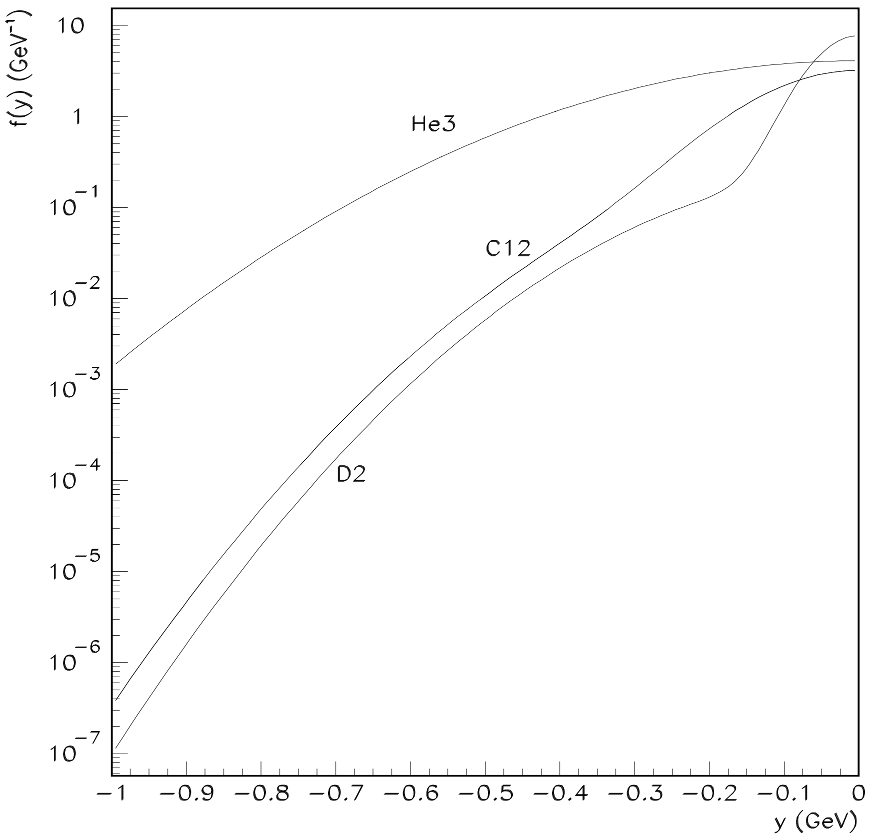

Figure B-1: Experimental scaling function $F(y)$ for ^{2}D, ^{3}He and C^{12} targets [111].

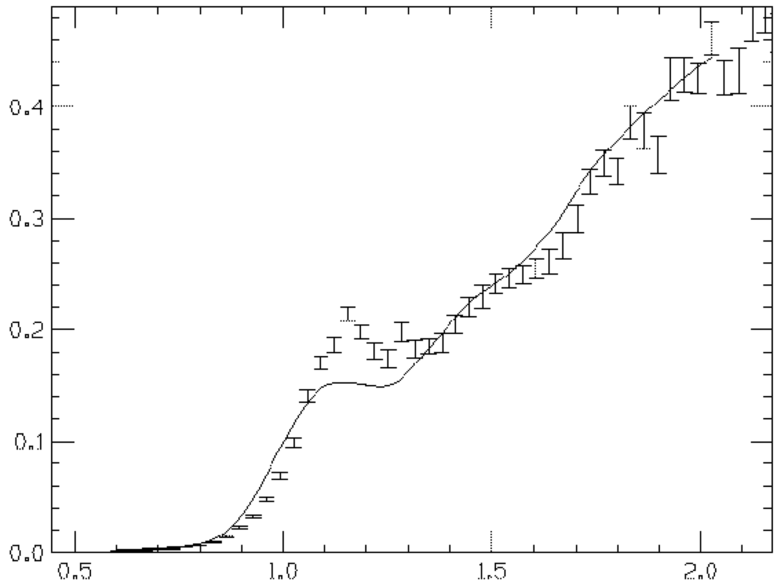

Figure B-2: The SLAC ^{3}He data in reference [133] is reproduced using $F(y)$ from reference [111]. The cross section (nb/MeV sr) is plotted as a function of energy transfer ν(GeV). Here the points are the data and the line is the calculation using y-scaling for the quasielastic peak($\nu = 1.2$ GeV).

Using equation (B.14), we calculate the double differential cross section from only the quasielastic contribution for the same data with E_i=3.258 GeV of different incident beam energy and $< Q^2 >$=0.3 GeV. The two top panels in figure B-3 show the double differential cross section as function of Q^2 and ν. As we described before, $W_1(Q^2, \nu)$ and $W_2(Q^2, \nu)$ were calculated from R_L and R_T by Rosenbluth separation. It is worth while to mention that there is a minimum invariant mass W^2 from the relation in equation B.6. It results in a cut-off value of ν at the lower axis. By integration over ν, the differential cross section is 0.202E+02 $\mu b\ sr/\mathrm{GeV}$ from the y-scaling method and 0.219E+02 $\mu\ sr/\mathrm{GeV}$ from the suppression factor method in TERAD.

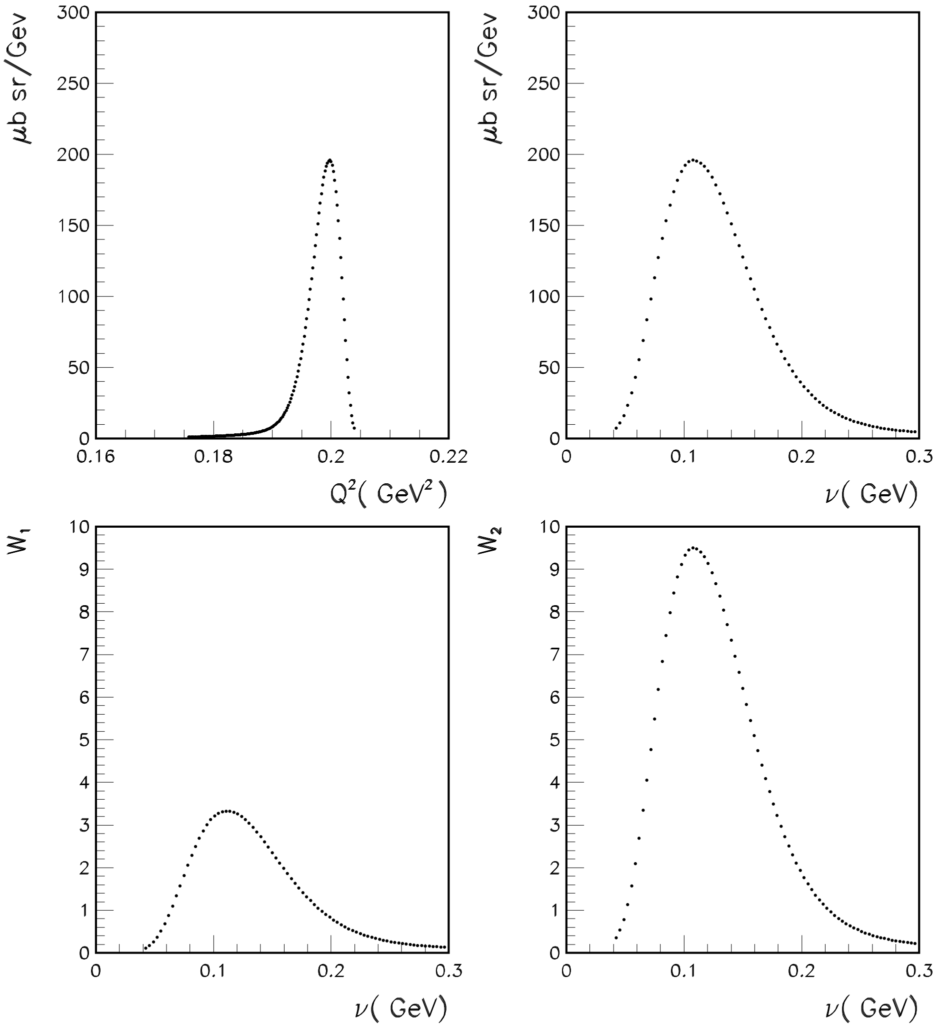

Figure B-3: Double differential cross section of SLAC ^{3}He data at E_i=3.258 GeV using y-scaling. The first two panels show the cross section as function of Q^2 and ν. The functions W_1 and W_2 are obtained by means of a Rosenbluth separation as a function of ν.

B.3 Quasielastic radiative tail

The cross section for inclusive quasielastic scattering can be presented in terms of the contraction of leptonic and hadronic tensors [131]

$$\frac{d\sigma}{d\nu dQ^2} = C_0 L_{\mu\nu} W_{\mu\nu}(p,q) \tag{B.15}$$

where p and q are four-vectors of proton and virtual photon. The hadronic tensor can be written as

$$\begin{aligned} W_{\mu\nu}(p,q) =& \left(\frac{q_\mu q_\nu}{q^2} - g_{\mu\nu}\right) W_1(Q^2,\nu) \\ &+ \frac{1}{M^2}\left(p_\mu - \frac{pq}{q^2}q_\mu\right)\left(p_\nu - \frac{pq}{q^2}q_\nu\right) W_2(Q^2,\nu). \end{aligned} \tag{B.16}$$

In this terminology, the quasielastic radiative tail is defined as

$$\sigma_q = \frac{d^2\sigma_q}{dxdy} = C\int \frac{d^3k}{2k_0}\left[L^{rad}_{\mu\nu} W_{\mu\nu}(p,q-k)\right]. \tag{B.17}$$

The arguments of the structure functions $W_{1,2}$ are, so called *true* variables $\tilde{\nu}$ and $\tilde{Q}^2$, which are defined as

$$\tilde{\nu} = \frac{1}{M}p(q-k) \text{ and } \tilde{Q}^2 = -(q-k)^2. \tag{B.18}$$

The integration region is a triangle and is defined by the following lines

$$\begin{aligned} Q^2_\pm &= Q^2 + 2(\nu - \tilde{\nu})(\nu \pm \sqrt{\nu^2 + Q^2}) \\ Q^2_\epsilon &= 2\tilde{\nu}(M_A - \epsilon) - \epsilon(2M_A - \epsilon). \end{aligned} \tag{B.19}$$

The first two equations are defined by restriction of the kinematics in the bremsstrahlung process. The third defines the region where the solution of the y-scaling equation exists. For practical calculation we made corresponding modifications of the known FORTRAN codes TERAD and POLRAD, which were developed for RC calculations in DIS.

B.3.1 TERAD

The most convenient way to implement the y-scaling formalism in TERAD is by generalization of the inelastic radiative tail. Several steps are necessary, namely, to calculate the limits of of integration over the true $\tilde{Q}^2$ and $\tilde{W}^2$, to generalize the DIS structure functions into the quasielastic region and to remove the infrared substraction, which is used in TERAD for the inelastic tail.

As a result, the formula for the quasielastic radiative tail within TERAD notation becomes the following

$$\sigma_1^q = \frac{2\alpha^3 S^2 y}{S^2 - 4m^2 M^2} \int\limits_{W_{min}^2}^{W_{max}^2} d\tilde{W}^2 \int\limits_{Q_{min}^2}^{Q_{max}^2} \frac{d\tilde{Q}^2}{\tilde{Q}^4} 2MW_1(\tilde{W}^2, \tilde{Q}^2)\mathcal{S}_1 + \tilde{\nu}W_2(\tilde{W}^2, \tilde{Q}^2)\frac{1}{T}\mathcal{S}_2 \tag{B.20}$$

where $MW_1 = F_1$ and $\tilde{\nu}W_2 = F_2$ are quasielastic structure functions discussed in the last sections. The quantities $\mathcal{S}_{1,2}$ are kinematical factors known exactly, $T = 2p(q-k) = \tilde{W}^2 + \tilde{Q}^2 - M^2$. The integration limits follow from equation (B.18) and have the following explicit form

$$\begin{aligned}
Q_{min}^2 &= max(Q_-^2, \epsilon_a(\tilde{W}^2 - M^2) + \epsilon_\mu) \\
Q_{max}^2 &= Q_+^2 \\
W_{min}^2 &= (M + m_\pi)^2 \\
W_{max}^2 &= W^2 \frac{2M(\nu + \sqrt{\nu^2 + Q^2}) + 2M^2\epsilon_a - 2\epsilon_\mu}{2M(\nu + \sqrt{\nu^2 + Q^2}) - 2Q^2 + 2W^2\epsilon_a}
\end{aligned} \tag{B.21}$$

where

$$\begin{aligned}
Q_\pm^2 &= \frac{1}{2W^2}\left[2M(W^2 - \tilde{W}^2)(\nu \pm \sqrt{\nu^2 + Q^2}) + 2\tilde{W}^2 Q^2\right] \\
\epsilon_a &= -\frac{A - \epsilon/M}{A - 1 - \epsilon/M} \\
\epsilon_\mu &= \frac{\epsilon(2A - \epsilon/M)}{A - 1 - \epsilon/M}.
\end{aligned} \tag{B.22}$$

We note that there are no limitation on the lower limit over $\tilde{W}^2$ coming from (B.18), so it is choosen arbitraily where the peak does not contribute.

B.3.2 POLRAD

The other method to implement the y-scaling formalism is the FORTRAN code POLRAD. Here, we added additional integration into subroutines to calculate the quasielastic radiative tail itself. Another set of photon variables $R = 2M(\nu - \tilde{\nu})$ and $\tau = (\tilde{Q}^2 - Q^2)/R$ is used instead of $\tilde{\nu}$ and $\tilde{Q}^2$ [131]. In this case the cross section for the quasielastic radiative tail is obtained in the form [131]:

$$\sigma_1^q = -\frac{\alpha^3 y}{A} \int\limits_{\tau_{min}}^{\tau_{max}} d\tau \sum_{i=1}^{2} \sum_{j=1}^{k_i} \theta_{ij}(\tau) \int\limits_{R_{min}}^{R_{max}} dR \frac{R^{j-2}}{(Q^2 + R\tau)^2} \Im_i. \tag{B.23}$$

where $\theta_{ij}(\tau)$ are kinematic factors known exactly. $\Im_i$ are combinations of quasielastic response functions. The explicit form of the limits of integration follows from (B.18)

$$\begin{aligned} \tau_{max,min} &= \frac{1}{M}(\nu \pm \sqrt{\nu + Q^2}) \\ R_{max} &= \frac{2\nu(M_A - \epsilon) - \epsilon(2M_A - \epsilon) - Q^2}{\tau + (M_a - \epsilon)/M}. \end{aligned} \tag{B.24}$$

For the lower limit of R we take pion threshold where the quasielastic peak vanishes:

$$R_{min} = \frac{2M\nu - Q^2 + M^2 - (M + m_\pi)^2}{1 + \tau}. \tag{B.25}$$

B.4 Results

The quasielastic radiative tails from unpolarized ^{2}H , ^{3}He , and ^{14}N targets are calculated using the y-scaling method. The results are summarized in tables A.1, A.2, and A.3. The comparisons between the y-scaling method and suppression factors using the Fermi gas model show good agreement for ^{3}He and ^{14}N targets. Therefore, the uncertainties for

Table B.1: The calculation of the quasielastic radiative tail for ^{2}H. The σ_{Born} is the Born cross section and σ_{qe}^{TERAD} is the quasielastic radiative tail using equation (B.17) in TERAD. $\sigma_{qe}^{yscaling}$ is the quasielastic radiative tail using the scaling function F(y). The unit of cross section is nbarn.

x	y	Q^2	σ_{Born}	σ_{qe}^{TERAD}	$\sigma_{qe}^{yscaling}$
0.0122	0.788	0.496	0.54946E+04	0.13830E+04	0.20115E+04
0.0169	0.752	0.656	0.36079E+04	0.65313E+03	0.90895E+03
0.0224	0.714	0.825	0.25638E+04	0.32185E+03	0.43993E+03
0.0286	0.679	1.002	0.19127E+04	0.16855E+03	0.22831E+03
0.0359	0.603	1.118	0.17176E+04	0.90460E+02	0.12297E+03
0.0449	0.602	1.394	0.11645E+04	0.47374E+02	0.65047E+02
0.0595	0.545	1.674	0.88465E+03	0.20873E+02	0.28502E+02
0.0842	0.470	2.042	0.65445E+03	0.76975E+01	0.10572E+02

quasielastic scattering radiative tail from those targets were determined by the relative differences. However, in the case of ^{2}H target, the y-scaling method produces different results from the TERAD. TERAD used the prescription from reference [100] as a standard input and was checked with references [135] and [124]. These methods are consistent within 2% throughout the whole kinematic range. The difference between the y-scaling approach and others was not resolved and y-scaling result for ^{2}H target was not used to obtain the results in this thesis.

Table B.2: The calculations of the quasielastic radiative tail for ^3He. the σ_{Born} is the Born cross section and σ_{qe}^{TERAD} is the quasielastic radiative tail using equation (B.17) in TERAD. $\sigma_{qe}^{yscaling}$ is the quasielastic radiative tail using the scaling function F(y). The unit of cross section is nbarn.

x	y	Q^2	σ_{Born}	σ_{qe}^{TERAD}	$\sigma_{qe}^{yscaling}$
0.0122	0.788	0.496	0.49291E+04	0.20816E+04	0.21006E+04
0.0169	0.752	0.656	0.33410E+04	0.92102E+03	0.89239E+03
0.0224	0.714	0.825	0.24375E+04	0.43630E+03	0.42904E+03
0.0286	0.679	1.002	0.18559E+04	0.22309E+03	0.21746E+03
0.0359	0.603	1.118	0.16933E+04	0.11670E+03	0.11247E+03
0.0449	0.602	1.394	0.11624E+04	0.60925E+02	0.58394E+02
0.0595	0.545	1.674	0.89348E+03	0.26610E+02	0.25050E+02
0.0842	0.470	2.042	0.66798E+03	0.97122E+01	0.89200E+01

Table B.3: The calculations of the quasielastic radiative tail for ^{14}N. the σ_{Born} is the Born cross section and σ_{qe}^{TERAD} is the quasielastic radiative tail using equation (B.17) in TERAD. $\sigma_{qe}^{yscaling}$ is the quasielastic radiative tail using the scaling function F(y). The unit of cross section is nbarn.

x	y	Q^2	σ_{Born}	σ_{qe}^{TERAD}	$\sigma_{qe}^{yscaling}$
0.0122	0.788	0.496	0.48957E+04	0.14380E+04	0.17399E+04
0.0169	0.752	0.656	0.33148E+04	0.68903E+03	0.76847E+03
0.0224	0.714	0.825	0.24154E+04	0.33445E+03	0.36489E+03
0.0286	0.679	1.002	0.18365E+04	0.17289E+03	0.18987E+03
0.0359	0.603	1.118	0.16729E+04	0.91580E+02	0.99384E+02
0.0449	0.602	1.394	0.11462E+04	0.47859E+02	0.51623E+02
0.0595	0.545	1.674	0.87816E+03	0.21011E+02	0.22272E+02
0.0842	0.470	2.042	0.65301E+03	0.77139E+01	0.79821E+01

Bibliography

[1] R.E. Taylor, Rev. Mod. Phys. 63 (1991) 573.

[2] J.I. Friedman, H.W. Kendall and R.E. Taylor, Rev. Mod. Phys. 63 (1991) 629.

[3] M. Gell-Mann, Phys. Lett. 8 (1964) 214.

[4] G. Zweig, CERN-TH-412.

[5] R.P. Feynman, Phys. Rev. Lett. 23 (1969) 1415.

[6] J.D. Bjorken and E.A. Paschos, Phys. Rev. 185 (1969) 1975.

[7] The European Muon Collaboration, J.J. Aubert et al., Phys. Lett. B123 (1983) 275.

[8] J. Ellis and R. Jaffe, Phys. Rev. D9 (1974) 1444.

[9] J. Ellis and R. Jaffe, Phys. Rev. D10 (1974) 1669.

[10] The European Muon Collaboration, J. Ashman et al., Phys. Lett B206 (1988) 364.

[11] The European Muon Collaboration, J. Ashman et al., Phys. Lett B328 (1989) 1.

[12] K. Gottfried, Phys. Rev. Lett 18 (1967) 1174.

[13] The New Muon Collaboration, M. Arneodo et al., Phys. Rev. D50 (1994) 1.

[14] E866 Collaboration, E.A. Hawker et al., Phys. Rev. Lett. 80 (1998) 3715.

[15] The HERMES Collaboration, K. Ackerstaff et al., Phys. Rev. Lett. 58 (1998) 5519.

[16] F.E. Close, An Introduction to Quarks and Partons (Academic press, 1979).

[17] F. Halzen and A.D. Martin, Quarks and leptons: an introductory course in modern particle physics (John Wiley and sons, New York, 1984).

[18] E.D. Bloom et al., Phys. Rev. Lett 23 (1969) 935.

[19] M. breidenbach et al., Phys. Rev. Lett 23 (1969) 935.

[20] R.P. Feyman, Phys. Rev. Lett 23 (1969) 1415.

[21] R.L. Jaffe, MIT-CTP-1261 (1985).

[22] R.L. Jaffe, Lectures presented at the Los Alamos School on Quark Nuclear Physics, Los Alamos Published in Los Alamos Wkshp. 0537 (1985).

[23] R.P. Feynman, Phys. Rev. Lett. 23 (1969) 1415.

[24] S.D. Drell and T. Yan, Ann. Phys. 66 (1971) 578.

[25] E.L. van Neerven, hep-ph/9905503 (1999).

[26] C.G. Callan and D.J. Gross, Phys. Rev. Lett. 22 (1969) 156.

[27] D.F. Geesaman, K. Saito and A.W. Thomas, Ann. Rev. Nucl. Part. Sci. 45 (1995) 337.

[28] K. Janson, Experimental investigations of the proton and deuterion structure functions, PhD thesis, Uppsala University, 1991.

[29] D.J. Gross and S.B. Treiman, Phys. Rev. D4 (1971) 1059.

[30] A.H. Mueller, Phys. Rev. D18 (1978) 3705.

[31] A.H. Mueller, Phys. Rept. 73 (1981) 237.

[32] T. Muta, Foundations of Quantum Chromodynamics: An Introduction to Perturbative Methods in Gauage Theories (World Scientific, Singapore, 1987).

[33] N. Christ, B. Hasslacher and A.H. Mueller, Phys. Rev. D6 (1972) 3543.

[34] E. Leader and E. Predazzi, An Introduction to Gauge Theories and The 'New Physics'. (Cambridge university press, 1982).

[35] J.D. Bjorken, Phys. Rev. 148 (1966) 1467.

[36] D.J. Gross and C.H.L. Smith, Nucl. Phys. B14 (1969) 337.

[37] A.J. Buras, Rev. Mod. Phys. 52 (1980) 199.

[38] G. Altarelli and G. Parisi, Nucl. Phys. B126 (1972) 298.

[39] G. Altarelli and G. MArtinelli, Phys. Lett. B76 (1982) 89.

[40] G. Piller and W. Weise, (1999), hep-ph/9908230.

[41] New Muon Collaboration, P. Amaudruz et al., Nucl. Phys. B441 (1995) 3.

[42] SLAC, J. Gomez et al., Phys. Rev. D49 (1994) 4348.

[43] BCDMS Collaboration, A.C. Benvenuti et al., Phys. Lett. B189 (1987) 483.

[44] E665 Collaboration, M.R. Adams et al., Phys. Rev. Lett. 68 (1992) 3266.

[45] E665 Collaboration, M.R. Adams et al., Z. Phys. C67 (1995) 403, hep-ex/9505006.

[46] E665 collaboration, M.R. Adams et al., Phys. Lett. B287 (1992) 375.

[47] New Muon Collaboration, P. Amaudruz et al., Z. Phys. C51 (1991) 387.

[48] New Muon Collaboration, P. Amaudruz et al., Z. Phys. C53 (1992) 73.

[49] New Muon Collaboration, M. Arneodo et al., Nucl. Phys. B481 (1996) 3.

[50] New Muon Collaboration, M. Arneodo et al., Nucl. Phys. B481 (1996) 23.

[51] K. Ackerstaff, First Results from the HERMES Experiment using Unpolarized Targets, PhD thesis, University Hamburg, 1996.

[52] V.A. Abramovsky, V.N. Gribov and O.V. Kancheli, Yad. Fiz. 18 (1973) 595.

[53] L.V. Gribov, E.M. Levin and M.G. Ryskin, Phys. Rept. 100 (1983) 1.

[54] A.H. Mueller and H. Navelet, Nucl. Phys. B282 (1987) 727.

[55] T.H. Bauer et al., Rev. Mod. Phys. 50 (1978) 261.

[56] L.L. Frankfurt and M.I. Strikman, Phys. Rept. 160 (1988) 235.

[57] S.J. Brodsky and H.J. Lu, Phys. Rev. Lett. 64 (1990) 1342.

[58] N.N. Nikolaev and V.R. Zoller, Z. Phys. C56 (1992) 623.

[59] V. Barone et al., Z. Phys. C58 (1993) 541.

[60] W. Melnitchouk and A.W. Thomas, Phys. Lett. B317 (1993) 437, nucl-th/9310005.

[61] G. Piller, W. Ratzka and W. Weise, Z. Phys. A352 (1995) 427, hep-ph/9504407.

[62] J. Hufner, B. Kopeliovich and J. Nemchik, Phys. Lett. B383 (1996) 362, nucl-th/9605007.

[63] J. Raufeisen, A.V. Tarasov and O.O. Voskresenskaya, Eur. Phys. J. A5 (1999) 173, hep-ph/9812398.

[64] G.K. Mallot, (1997), hep-ex/9703014.

[65] L.W. Whitlow et al., Phys. Lett. B250 (1990) 193.

[66] New Muon, M. Arneodo et al., Nucl. Phys. B483 (1997) 3, hep-ph/9610231.

[67] CCFR/NuTeV Collaboration, U. Yang et al., J. Phys. G22 (1996) 775, hep-ex/9605005.

[68] A.A. Sokolov and I.M. Ternov, Sov. Phys. Doklady 8 (1964) 1203.

[69] W. Lorenzon, Proc. of the Workshop "Polarized gas targets and polarized beams,", edited by R.J. Holt and M.A. Miller, p. 181, Urbana-Champagne, USA, 1997, AIP Conf. Proc. 421.

[70] B.E. Tipton, Measurement of Polarized Parton Distributions with Spin-dependent Deep-Inelastic Scattering, PhD thesis, Massachusetts Institute of Technology, 1999.

[71] D. DeSchepper et al., Nucl. Instrum. Meth. A419 (1998) 16.

[72] J. Stewart, Proc. of the Workshop "Polarized gas targets and polarized beams,", edited by R.J. Holt and M.A. Miller, p. 69, Urbana-Champagne, USA, 1997, AIP Conf. Proc. 421.

[73] HERMES Collaboration, K. Ackerstaff et al., Phys. Rev. Lett. 82 (1999) 3025.

[74] M. Kolstein, Exclusive ρ^0-Meson Electroproduction at HERMES, PhD thesis, Vrije Universiteit Amsterdam, 1998.

[75] M.F. Sutter, A Study of Spin Transfer in Fragmentation in the Leptoproduction of the Λ, PhD thesis, Massachusetts Institute of Technology, 1998.

[76] H. Kolster, The HERMES Gaseous Internal Polarized Proton Target and its use in the HERA Positron Storage Ring, PhD thesis, Ludwig Maximilians Universität München, 1998.

[77] C. Baumgarten, Proc. of "13th International Symposium on High-Energy Spin Physics (SPIN98)", Protvino, Russia, 1998.

[78] B. Braun, Proc. of the Workshop "Polarized gas targets and polarized beams,", edited by R.J. Holt and M.A. Miller, p. 156, Urbana-Champagne, USA, 1997, AIP Conf. Proc. 421.

[79] J.W. Martin, "Results of Recent Low-α Running", HERMES Collaboration Meeting, August 1997.

[80] B. Dolgoshein, Nucl. Instr. and Meth. A 326 (1993) 434.

[81] X. Artru et al., Phys. Rep. D 12 (1975) 1289.

[82] M.A. Funk, A Measurement of the Polarized Parton Densities of the Nucleon in Deep-Inelastic Scattering at HERMES, PhD thesis, Universitaet Hamburg, 1998.

[83] W. Wander, Reconstruction of High Energy Scattering Events in the HERMES experiment, PhD thesis, Universität Erlangen Nürnberg, 1995.

[84] B. Braun et al., CERN-CN Application Software Group (1993).

[85] P. Geiger et al., http://www-hermes.desy.de/hmc/.

[86] Experimental Physics Input Output Package,CERN Program Library Long Writeup I101, http://consult.cern.ch/writeup/epio/.

[87] G. D'Agostini, Nucl. Instrum. Meth. A362 (1995) 487.

[88] Particle Data Group, Particle and Fields, Review of Particle Properties, Phys. Rev. D, APS.

[89] New Muon Collaboration, M. Arneodo et al., Nucl. Phys. B487 (1997) 3.

[90] T.S. Tsai, Phys. Rev 120 (1960) 269.

[91] T.S. Tsai, Phys. Rev 120 (1960) 269.

[92] L.W. Mo and Y.S. Tsai, Rev. Mod. Phys. 41 (1969) 205.

[93] A.A. Akhundov, D.Y. Bardin and N.M. Sumeiko, Sov. J. Nucl. Phys 26 (1977) 660.

[94] D.Y. Bardin and N.M. Sumeiko, Sov. J. Nucl. Phys 29 (1979) 499.

[95] A.A. Akhundov et al., Sov. J. Nucl. Phys 44 (1986) 988.

[96] B. Badelek et al., Z. Phys. C66 (1995) 591, hep-ph/940238.

[97] B. Badelek and J. Kweiencinski, Phys. Lett. B295 (1992) 263.

[98] M. Gari and W. Krümpelmann, Z. Phys. A322 (1985) 689.

[99] A. Svarc and M.P. Locher, Fizika 22 (1990) 549.

[100] J. Bernabeu, Nucl. Phys. B49 (1972) 186.

[101] L.I. Shiff, Phys. Rev 3B (1964) 133.

[102] E.J. Moniz et al., Phys. Rev. 184 (1969) 1154.

[103] C.W.D. Jager et al., Atomic Data and Nuclear Data Tables 14 (1974) 479.

[104] G. Hoehler et al., Nucl. Phys. B114 (1976) 505.

[105] S. Platchkov, Nucl. Phys. A510 (1990) 740.

[106] P.C. Dunn et al., Phys. Rev. C 27 No 1 (1983) 71.

[107] H.D. Vries et al., Atomic Data and Nuclear Data Tables 36 (1987) 501.

[108] R.L. Huffman et al., Phys. Lett 139B (1984) 249.

[109] T.W. Donnelly and I. Sick, Rev. Mod. Phys. 56 (1984) 514.

[110] T.W. Donnelly, Massachusetts Institute of Technology , By priviate communication.

[111] D. Day, University of Virginia , By priviate communication.

[112] SLAC, K. Abe et al., Phys. Lett. B452 (1999) 194.

[113] New Muon Collaboration, P. Amaudruz et al., Phys. Lett. B294 (1992) 120.

[114] New Muon Collaboration, M. Arneodo et al., Nucl. Phys. B481 (1996) 23.

[115] SLAC, S. dasu et al., Phys. Rev. D49 (1994) 5641.

[116] E143, K. Abe et al., Phys. Lett. B452 (1999) 194, hep-ex/9808028.

[117] HERMES, K. Ackerstaff et al., (1999), hep-ex/9910071.

[118] N.N. Nikolaev and B.G. Zakharov, Z. Phys. C49 (1991) 607.

[119] V. Barone and M. Genovese, Proc. of the Workshop 1995/1996 on "Future Physics at HERA", edited by G. Ingelman, A. de Roech and R. Klanner, p. 800, DESY, 1996.

[120] L. Criegee et al., Nucl. Phys. B121 (1977) 38.

[121] J. Franz et al., Z. Phys. C10 (1981) 105.

[122] J. Bailey et al., Nucl. Phys. B151 (1979) 367.

[123] J. Eickmeyer et al., Phys. Rev. Lett. 36 (1976) 289.

[124] S. Stein et al., Phys. Rev. D12 (1975) 1884.

[125] R.K. Ellis et al., Nucl. Phys. B207 (1982) 1.

[126] S. Barshay and D. Rein, Z. Phys. C46 (1990) 215.

[127] T. Gousset and T.H. Pirner, Phys. Lett. B375 (1996) 349.

[128] B. Kopeliovich and M. Strikman, private communication .

[129] M. Luo et al., Phys. Rev. D49 (1994) 4493.

[130] A. Roth, Vacuum Technology (North-holland, 1982).

[131] I. Akushevich et al., Comput. Phys. Commun. 104 (1997) 201, hep-ph/9706516.

[132] D.B. Day et al., Annu. Rev. Nucl. Part. Sci. 40 (1990) 357.

[133] C.C. delgi Atti, E. Pace and G. Salme, Phys. Rev. c43 (1991) 1155.

[134] T. de Forest, Nucl Phys A392 (1983) 232.

[135] H. Arenhovel, Nucl. Phys. A384 (1982) 287, ;Private communication.

List of Figures

List of Tables